


Novel planar photonic antennas to address the dynamic nanoarchitecture of biological membranes

DOCTORAL THESIS

by

Pamina M. Winkler

under the supervision of

Prof. María F. García-Parajo

ICFO – Institut de Ciències Fotòniques
UPC - Universitat Politècnica de Catalunya
BIST – Barcelona Institute of Science and Technology

Castelldefels, in October 2020

for my grandfather,
who sparked my curiosity for finding scientific solutions

for my parents,
without their unconditional love and support I would not be here

for my three sisters,
my strongest supporters and harshest critics during the up and downs of my PhD journey and always giving me a reason to laugh.

Dans la vie, il n'y a pas de solutions. Il y a des forces en marche: il faut les créer et les solutions suivent.

Vol de nuit de Antoine de Saint-Excupéry

This PhD thesis was financially supported by a ICFOstepstone Fellowship, a COFUND Doctoral Programme of the Marie-Sklodowska-Curie-Action in the framework of the European Union's Horizon 2020 research and innovation programme under the Marie Skłodowska-Curie grant agreement No 665884.

Abstract

The cell membrane is the encompassing protective shield of every cell and it is composed of a multitude of proteins, lipids and other molecules. The organization of the cell membrane is inextricably intertwined with its function, and sensitive to perturbations from the underlying actin cytoskeleton and the extracellular environment at the nano- and the mesoscale. Elucidating the dynamic interplay between lipids and proteins diffusing on the cell membrane, forming transient domains and (re)organizing them according to signals from the juxtaposed inner and outer meshwork, is of paramount interest in fundamental cell biology. The overarching goal of this thesis is to gain deeper insight into how lipids and proteins dynamically organize in biological membranes at the nanoscale.

Photonic nano-antennas are metallic nanostructures that localize and enhance the incident optical radiation into highly confined nanometric regions (< 20 nm), leading to greatly enhanced light-matter interactions. In this thesis, we exploit an innovative design of planar gold nano-antenna arrays of different gap sizes (10-45 nm) and embedded in nanometric-size boxes. To elucidate nanoscale diffusion dynamics in biological membranes with high spatiotemporal resolution and single-molecule detection sensitivity, we further combine our nanogap antenna arrays with fluorescence correlation spectroscopy (FCS) in a serial and multiplexed manner.

In this dissertation, we first describe the fabrication process of these planar gold nanogap antennas and characterize their performance by means of electron microscopy and FCS of individual molecules in solution. We demonstrate giant fluorescence enhancement factors of up to 10^4-10^5 times provided by our planar nanogap antennas in ultra-confined detection volumes and with single molecule detection sensitivity in the micromolar range.

Second, we apply these planar plasmonic nano-antennas in combination with FCS for assessing the dynamic organization of mimetic lipid membranes at the nanoscale. For a ternary composition of the model membranes that include unsaturated and saturated lipids together with cholesterol, we resolve transient nanoscopic heterogeneities as small as 10 nm in size, coexisting in both macroscopically phase-separated lipid phases.

Third, we add a Hyaluronic Acid (HA) layer on top of the model lipid membranes to emulate the effect of the extracellular environment surrounding native biological membranes. We extend our nano-antenna-FCS approach with atomic force microscopy and spectroscopy. We reveal a distinct influence of HA on the nanoscale lipid organization of mimetic membranes composed of lipids constituting the more ordered lipid phase. Our results indicate a synergistic effect of cholesterol and HA re-organizing biological membranes at the nanoscale.

Fourth, we apply our planar nano-antenna platform combined with FCS to elucidate the nanoscale dynamics of different lipids in living cells. With our nanogap antennas we were able to breach into the sub-30 nm spatial scale on living cell membranes for the first time. We provide compelling evidence of short-lived cholesterol-induced ~10 nm nanodomain partitioning in living plasma membranes.

Fifth, we demonstrate the multiplexing capabilities of our planar gold nanogap antenna platform combined with FCS in a widefield illumination scheme combined with sCMOS camera detection. Our approach allows recording of fluorescence signal from more than 200 antennas simultaneously. Moreover, we demonstrate multiplexed FCS recording on 50 nano-antennas simultaneously, both in solution as well as in living cells, with a temporal resolution in the millisecond range. The dissertation finishes with a brief discussion of the main results achieved in this research and proposes new avenues for future research in the field.

Resumen

La membrana plasmática separa el entorno intracelular del extracelular y está compuesta por una multitud de diferentes proteínas y lípidos. Su organización está fuertemente interconectada a su función, y es sensible a perturbaciones tanto de la actina cortical posicionada internamente en proximidad con la membrana, así como de una red extracelular en contacto próximo con la membrana exterior. Estas perturbaciones ocurren a distintas escalas temporales y espaciales, llegando a unos pocos nanómetros. Dada la estrecha relación entre la organización de la membrana y su función biológica, es tremendamente importante entender como lípidos y proteínas se organizan dinámicamente a la escala nanométrica y como se ven afectados por su entorno. El objetivo principal de esta tesis doctoral se centra en alcanzar este entendimiento.

Las antenas fotónicas son nano-estructuras metálicas que incrementan la radiación electromagnética en regiones nanométricas (< 20 nm) del espacio. En esta tesis doctoral, hemos fabricado y utilizado plataformas con matrices de antenas en oro, y con regiones de confinamiento entre 10-45 nm. Además, hemos combinado estas antenas con la técnica de "fluorescence correlation spectroscopy (FCS)" a fin de obtener información espaciotemporal a la nano-escala en membranas biológicas, junto a la sensibilidad de detectar moléculas individuales a altas concentraciones.

En esta disertación, describimos primero la fabricación de antenas fotónicas y caracterizamos su rendimiento utilizando técnicas de microscopía electrónica y FCS de moléculas individuales en solución. Nuestros resultados demuestran factores de incremento de la fluorescencia entre 10^4-10^5, en regiones ultra-confinadas, y una capacidad para detectar moléculas individuales en rango de concentraciones de micro-molares.

Una vez validadas nuestras herramientas, nos enfocamos en su uso para el estudio dinámico de la organización de membranas lipídicas miméticas a escala nanométrica. En el caso de composiciones ternarias de lípidos insaturados, saturados y colesterol, hemos descubierto la existencia de heterogeneidades nanoscópicas y transitorias que coexisten tanto en las regiones ordenadas como desordenadas de las membranas lipídicas.

El siguiente capítulo contiene resultados enfocados a estudiar el efecto del entorno extracelular en la organización dinámica de este tipo de capas lipídicas. Para ello, y como modelo, preparamos membranas lipídicas cubiertas de ácido hialurónico (HA), un componente abundantemente expresado en la matriz extracelular. Combinando FCS con microscopia y espectroscopia de fuerzas atómicas, logramos resolver la influencia de HA a escala nanométrica en la organización de la fase ordenada de las membranas lipídicas. Nuestros resultados indican la existencia de un efecto sinérgico entre HA y colesterol en el reordenamiento de la membrana a la nano-escala.

El siguiente tema de investigación en esta tesis doctoral se enfoca a la aplicación de antenas fotónicas y FCS para el estudio de dominios lipídicos enriquecidos de colesterol en la membrana plasmática de células vivas. La utilización de estas antenas nos ha permitido, por primera vez, remontar la barrera de 30 nm, y demostrar de manera inequívoca la existencia de dominios enriquecidos en colesterol en células vivas con una resolución espacial de 10 nm.

Finalmente, hemos demostrado la capacidad de multiplexado de nuestras antenas fotónicas, combinando una iluminación y detección en campo amplio utilizando una camera sCMOS. Describimos la implementación de nuestro esquema, así como también medidas que demuestran la detección simultánea de fluorescencia en más de 200 antenas. De manera importante, demostramos la obtención de curvas de FCS en 50 antenas simultáneamente, tanto en solución como en células vivas. Esta disertación culmina con una breve discusión de los resultados más importantes de esta investigación doctoral y propone nuevas avenidas de investigación en el futuro.

TABLE OF CONTENTS

1 Introduction[1]

The cell membrane is the encompassing protective shield of every cell and is composed of a multitude of proteins, lipids and other molecules. The organization of the cell membrane is inextricably intertwined with its function, and sensitive to perturbations from the underlying actin cytoskeleton and the extracellular environment at the nano- and the mesoscale. Elucidating the dynamic interplay between lipids and proteins diffusing on the cell membrane, forming transient domains and (re)organizing them according to signals from the juxtaposed inner and outer meshwork is of paramount interest in fundamental cell biology. How lipids and proteins organize dynamically in biological membranes at the nanoscale frames the overall aim of this dissertation.

Throughout this PhD research an innovative design of photonic nano-antennas combined with fluorescence correlation spectroscopy (FCS) is exploited to elucidate nanoscale diffusion dynamics in biological membranes with high spatiotemporal resolution and single-molecule detection sensitivity.

In this introductory chapter a general motivation for the importance of cell membrane spatiotemporal compartmentalization is first presented together with a review on the relevant research findings. Second, the optical techniques employed for super-resolved single-molecule detection in living

[1] The content of this chapter has been partially published in:
Winkler, P.M., Regmi, R., Flauraud, V., Brugger, J., Rigneault, H., Wenger, J. and García-Parajo, M.F., *Optical Antenna-Based Fluorescence Correlation Spectroscopy to Probe the Nanoscale Dynamics of Biological Membranes*. J. Phys. Chem. Lett., 2018, 9, 1, 110-119.

cells are outlined. Third, the nanophotonic approaches to address the complexity of the cell membrane at the nanoscale are discussed. Last, the outline of the chapters composing this dissertation is given.

1.1 General Motivation

The plasma membrane of living cells is a complex, versatile and essential signaling interface that separates the cell cytoplasm from the extracellular space.[1,2] Research in the last twenty years has provided compelling evidence that the plasma membrane is highly compartmentalized at multiple spatial scales, ranging from the nano- to the meso-scale. Importantly, this non-random spatiotemporal organization appears to be crucial for cell function.[3,4] The basis for understanding cell membrane structure was proposed nearly 50 years ago by Singer and Nicolson.[2,5] This fluid mosaic model captures the general characteristics of the cell membrane as a lipid bilayer dressed with embedded proteins. However, intensive research in the last twenty years has revealed that biological membranes are highly heterogeneous and of a much higher complex architecture that goes well beyond what it was initially proposed by the fluid mosaic model.

Within the plane of the membrane certain types of proteins, sphingolipids and cholesterol arrange in transient nanoscopic domains, also denoted as lipid rafts.[1,2,6–8] These highly dynamic and fluctuating nanoscale assemblies can be stabilized in the presence of lipid- or protein-mediated activation events to compartmentalize cellular processes.[2,9] By means of physically segregating specific molecular components within the membrane, lipid rafts are believed to modulate the activity of raft-associated proteins, and to influence signaling and function of a broad range of membrane receptors.[4,10–12] Moreover, recent research indicates that the biophysical properties of lipid rafts (size, composition and dynamics) can be modulated by the proximal actin cytoskeleton[13–15] and components of the extracellular matrix[16–20], adding an extra-layer of complexity to the sub-compartmentalization of the plasma membrane. While the overwhelming diversity of membrane nanodomains makes their study particularly challenging, understanding the fundamental mechanisms that lead to raft formation as the first organizing principle of the cell membrane is of paramount importance.

Mimetic lipid membranes have been extensively used as model systems since they recapitulate some of the most important features of biological membranes.[21–24] On the microscopic scale, ternary lipid membranes composed of unsaturated phospholipids, saturated sphingolipids and cholesterol separate into two distinct liquid phases which can be resolved by diffraction-limited optics: a liquid-disordered (Ld) phase comprised mainly of unsaturated phospholipids and a liquid-ordered (Lo) phase mostly composed of saturated lipids and cholesterol.[2,4,25]

This Lo phase has been considered to represent the potential physical model for lipid rafts in living cell membranes.[2,4,21–24] Microscopic and stable liquid-liquid phase separation has been observed on both supported lipid bilayers (SLB) and giant unilamellar vesicles prepared from cell membrane lipid extracts.[26,27] However, such phase coexistence has remained so far largely unresolved on biological membranes.

Interestingly, several studies have shown that the cell membrane in all its complexity is fully capable of phase segregating into a micrometer-sized two-phase fluid-fluid system. Such a two-phase system has been reported to occur upon a temperature decrease[28] or induced through ganglioside GM1 (a raft lipid) tightening by its ligand cholera toxin-β (CTxB) at physiological temperatures[29], provided that the membrane is separated from the influence of the cortical cytoskeleton. Based on these results, it has been proposed that an underlying selective connectivity mediated by cholesterol must exist among membrane rafts even at the resting state.[2,29] This connectivity will thus be responsible for the large-scale phase segregation induced far beyond the valency of initial GM1 tightening through CTxB.[29,30] Yet, most of the experimental proof for such raft connectivity has been based on the visualization of the end stage of an activated condition and in the absence of the cytoskeleton and/or membrane traffic, where the transient rafts are amplified to coalesce into larger, stable micrometer-sized raft domains. It is only at this scale that standard fluorescence microscopy is able to observe this segregation.

1.2 Optical techniques towards super-resolved single-molecule detection in living cells

In the context of fully intact living cells, early investigations on membrane organization yielded conflicting results regarding the sizes, distribution and dynamics of lipid rafts, including experimental results that refuted their existence.[2,4,9,31,32] Most of the earliest work was performed using fluorescence recovery after photobleaching (FRAP)[33,34] and more recently, using single particle tracking (SPT)[3,32,34,35] and **fluorescence correlation spectroscopy (FCS)**[32,34,36].

FCS has been widely adopted for studying structural dynamics and biomolecular interactions on cell membranes as it features several key advantages.[36–38] The working principle of FCS is to monitor over time intensity fluctuations of fluorescently labeled molecules diffusing through a fixed illumination volume using diffraction-limited confocal excitation. By performing an autocorrelation of the

fluorescence intensity trace in time, the number of molecules and the diffusion coefficient, among other parameters can be extracted. This allows determination of the mean transit time over thousands of single-molecule diffusion events. The advent of single photon counting avalanche diodes has made it possible to resolve the local molecular mobility of single molecules at picosecond temporal resolution over a broad dynamic range. To guarantee single-molecule detection sensitivity in a confocal illumination spot the required fluorescent labeling concentration should be within the pM range, well below physiologically relevant concentrations (µM - mM). This precludes single-molecule analysis by means of standard FCS within the crowded environment of the cell membrane. Moreover, FCS is an averaging technique based on thousands of individual molecule events, hence the influence of local variations in the composition and/or organization of the cell membrane on the diffusion of the molecule of interest remains hidden. In spite of these limitations, FCS has been broadly employed to investigate biological systems due to its straightforward implementation and non-invasiveness. Every obtained FCS correlation function contains rich information on molecular mobility. Yet, it is hard to retrieve a complete description of the underlying diffusion behavior (free, anomalous, constrained, directed …) out of a single FCS measurement. Alternatively, a more powerful method consists in performing diffusion measurements over a range of observation areas, as first introduced by Yechiel and Edidin in the context of FRAP.[39]

This concept has been further generalized by Lenne and coworkers to establish the so-called "FCS diffusion law"[40,41], which is a graph (Figure 1-1) representing the average FCS diffusion time $\tau(\omega^2)$ as a function of increasing observation area ω^2 and can be linearly fitted according to:

$$\boldsymbol{\tau(\omega^2) = t_0 + \omega^2/(4 \times D)} \quad \textbf{Eq. 1-1}$$

where D corresponds to the effective diffusion coefficient, and t_0 corresponds to the y-intercept. Figure 1-1 illustrates the measurement principle to obtain a FCS diffusion law plot by a variation of illumination areas on an exemplary biological membrane as well as four possibly occurring diffusion modes.

Note that the corresponding approach of performing a series of FCS measurements for different observation areas has been coined "spot-variation FCS" (svFCS).[40] Once the FCS diffusion law graph from a svFCS measurement series is obtained, its shape allows one to determine the nature of the diffusion process and to infer the

underlying membrane organization at scales smaller than the accessible experimental observation area.[40,42]

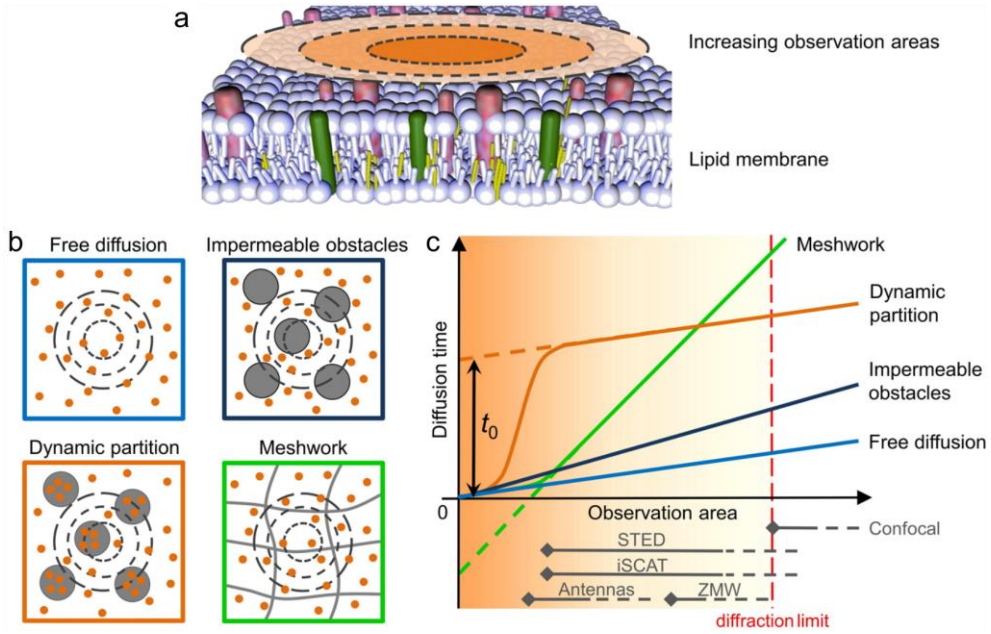

Figure 1-1. ***Principle of FCS diffusion laws to reveal biological membrane organization at the nanoscale.*** *(a) FCS diffusion laws are constructed by measuring the diffusion times of molecules traversing illumination areas of increasing sizes. (b) Different diffusion models depending on the membrane organization can be distinguished by varying the illumination areas. Molecules can freely diffuse on the membrane or show hindered diffusion due to their dynamic partitioning into nanodomains or due to the cortical actin meshwork. (c) FCS diffusion laws showing diffusion times vs. observation area. The type of diffusion is retrieved by extrapolation of the curves through the y-axis intercept t_0. Free diffusion and impermeable obstacles are characterized by $t_0 = 0$, while a positive t_0 intercept indicates the presence of nanodomains transiently trapping the molecular probe. A negative t_0 intercept relates to a meshwork of barriers separating adjacent domains. The observation areas accessible with various techniques that overcome the diffraction limit are indicated as grey lines. Adapted from Ref. 43.*

Free diffusion is characterized by a strict linear relationship between the diffusion time and the illumination area, hence the curve crosses the origin. The presence of impermeable obstacles constrains the diffusion and increases the apparent time to traverse a given observation area, thus the slope of the FCS diffusion law is larger, but the origin (0,0) is still crossed. Notably, the presence of confinement affecting the lateral diffusion is revealed by a deviation of the intercept on the time axis t_0

from the origin (Figure 1-1 c). For instance, in the case of hindered diffusion due to nanodomains, the extrapolation of the experimental curve to the intercept with the time axis results in a positive intercept on the time axis i.e. $t_0 > 0$. In contrast, hindered diffusion due to an underlying meshwork results in a negative intercept i.e., $t_0 < 0$.

FCS diffusion laws were first validated on diffraction-limited confocal microscopes, where for the transferrin receptor TfR-GFP (known to interact with the cytoskeleton meshwork) the results yielded a negative t_0 value, and for the fluorescent ganglioside GM1 a positive t_0 value was found.[40,44] By extrapolating to the origin, the FCS diffusion laws can thus predict the occurrence of membrane heterogeneities affecting the lateral diffusion at spatial scales well beyond the optical resolution. However, the size of lipid rafts is expected to be around 10-100 nm[9,36,45], so their areas are 5× to 500× smaller than the smallest diffraction-limited observation area on confocal microscopes. Reducing the gap between optical resolution and the size of lipid rafts to gain better insights on membrane organization at the nanoscale is currently a field of active research.

With the advent of super-resolution optical microscopy approaches such as single-molecule localization methods[46–48], **stimulated emission depletion (STED) microscopy**[49–51] and **near-field scanning optical microscopy (NSOM)**[10,52–55], it is now becoming clearer that lipids and proteins can indeed organize in nanometric compartments on the cell membrane, albeit a consensus in terms of their sizes and dynamics has not yet been reached.

The approach of **NSOM** relies on the scanning of a sub-wavelength aperture probe across the sample surface to map out its super-resolved architecture (Figure 1-2 a). The NSOM resolution in the axial and lateral dimensions is dictated by the physical size of the nano-aperture which is nanofabricated at the apex of a metallic tip, and the scanning tip-sample distance.[56] Spatial resolutions in the order of 70 nm are commonly obtained using this approach. In this design the combination of NSOM with FCS was successfully applied for dynamic measurements in living cells. For instance, it was shown that the fluorescent lipid analog SM exhibited anomalous diffusion on living cell membranes at the nanoscale, which could not be resolved by confocal microscopy.[57] A more sophisticated illumination scheme that increases the optical resolutions consists in the addition of a monopole antenna on a bowtie nano-aperture at the apex of a NSOM probe.[58] This approach allows for dual-color

single-molecule detection with 20 nm lateral resolution at high photon counts per molecule, but its combination with FCS has not been demonstrated yet.

Since the beginnings of **STED** microscopy, this powerful far-field optical technique has continued to push the limits far beyond the diffraction limit. Currently, a lateral resolution of ~40 nm is routinely achieved, and it can be pushed down to a few nanometers with the use of tailor-made fluorescent probes.[59] In STED microscopy the diffraction limit is overcome by exciting the fluorophore from the ground (OFF) state into an excited (ON) state first. Then the fluorophore has two options to relax back into the ground state. It is either "forced" to be de-excited into the ground state via stimulated emission, without the emission of a fluorescent photon, or it relaxes back spontaneously into the ground state while emitting a fluorescent photon. This ON/OFF switching is reiterated until enough emitted photons have been collected. The result is a super-resolved STED image composed of all collected photons which are localized well beyond the diffraction limit. The most common STED implementation is via a coalignment of a Gaussian excitation beam with a second beam, the so-called STED or depletion beam. This STED beam is shifted to longer wavelengths to de-excite the fluorophores via stimulated emission and engineered in polarization and/or phase to provide a doughnut-shaped intensity distribution in the focus with a "zero-intensity" area in its center. Both beams are diffraction-limited but by applying a high STED laser intensity the stimulated emission transition is efficiently saturated and only the fluorophore(s) around the "zero intensity" region remain in the excited state and their fluorescent emission is detected. An image is created by scanning the overlapped excitation and STED beams over the sample, and by collecting the emitted photons. The effective sub-diffraction area is then given by the "zero intensity" region. Since photons outside this region need to be fully depleted by stimulated emission, high laser powers are required and thus the obtainable spatial resolution scales inversely with increasing STED beam intensity. In practice, the resolution also depends on the brightness and the photostability of the fluorophore to withstand the high intensity laser powers required by STED.

With regard to biological applications of STED nanoscopy, a major advance has been achieved by combining STED with FCS, allowing the exploration of the nanoscale dynamics occurring in lipid membranes.[60–65] More precisely, it led to the beginning of spot-variation STED-FCS due to the straightforward possibility of probing different effective observation volumes as a function of the laser intensity

of the STED depletion beam. Depending on which nanoscale diffusion behavior is studied, the appropriate STED-FCS modality has to be chosen.[66]

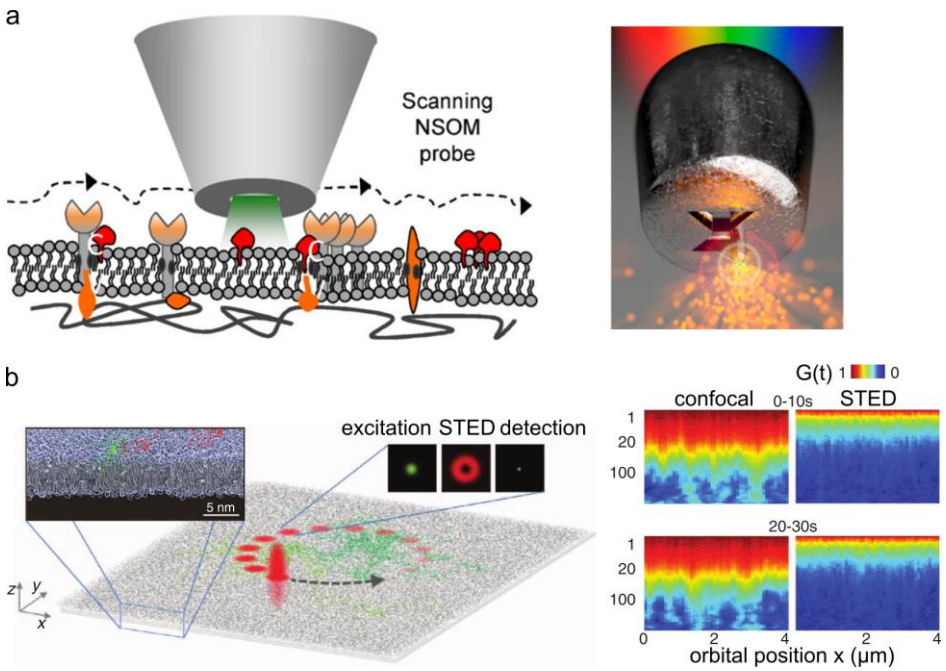

Figure 1-2. ***Principles of two scanning super-resolution approaches to resolve the nanoscale organization of biological membranes.*** *(a) On the left side, the principle of NSOM based nanoscopy on cell membranes is sketched. In the imaging mode, the NSOM probe scans the sample in close proximity to the surface (dashed line). The optical resolution (typically 70 nm) depends on the probe diameter and probe-sample axial distance separation. The optical resolution can be further increased by using hybrid bowtie nano-aperture (BNA) probes (right panel). This type of antennas consists of a monopole antenna positioned at one of the edges of the BNA gap and they are fabricated using focused ion beam (FIB) technology. Adapted from Ref.56,58. In (b) the principle of scanning STED-FCS (sSTED-FCS) is outlined. In this configuration the STED illumination is circularly scanned over the membrane sample, resulting in a fluorescence time trace generated for each pixel along the circle. In the panels on the right correlation curves are presented in a color code, yielding so-called correlation carpets. Different correlation carpets for confocal and STED are shown at different 10 seconds subsets of the measurements, highlighting changes of spatial heterogeneity over time. Adapted from Ref. 63.*

The most common approach is so-called point STED-FCS (pSTED-FCS) in which the measurement consists of a series of single stationary observation spots. pSTED-FCS provides high spatial (~30 nm) and temporal (microseconds) resolution but is limited by low throughput and sparse sampling.

The advent of fast laser-beam scanners led to the recording of multiple FCS measurements by scanning along a line or a circle at the micron-scale with high frequency (1-10 kHz), so called scanning STED-FCS (sSTED–FCS)[63], and shown in Figure 1-2 b. This modality allows one to explore with high statistical precision the spatial heterogeneity of lipids in the plasma membrane in short timeframes. The combination with line-interleaved laser scanning enables direct detection of diffusion behavior at multiple positions by alternating between STED and confocal laser illumination. The gain in statistics in the spatial domain is at the expense of temporal resolution, i.e. in the millisecond regime due to the kHz scanning frequency of the STED beam. Ergo, only accurate measurements of diffusion coefficients smaller than 10 $\mu m^2/s$ are feasible. To accurately extract diffusion dynamics via FCS analysis the scanning frequency has to be at least four times higher than the characteristic diffusion time of the probed molecule. This requirement determines the size of the detection spot, and thus the spatial resolution. In the case of live cell experiments with fluorescent lipid analogs of a diffusion coefficient $D \sim 0.5\ \mu m^2/s$, the smallest observation spot has a diameter d $\sim$ 60 nm at a minimal scanning frequency of 3 kHz.[63] Also note that the detected photon counts are divided between multiple curves in sSTED-FCS, hence the signal-to-noise ratio is reduced in comparison to pSTED-FCS. This can be compensated by collecting for longer time windows (< 30 s). More recently, it has been shown that hybrid detectors and real-time gigahertz sampling fully alleviated this issue, rendering possible photon count rates with an average intensity over 1 MHz.[67] Another approach to generate a FCS diffusion law from a single recording is based on a continuous-wave depletion laser with pulsed excitation and software processing by signal gating or lifetime filtering (STED-FLCS).[62,68]

In terms of biological insights obtained by STED-FCS experiments on living cell membranes, it has been shown that unlike phosphoglycerolipids, sphingolipids and GPI-APs are transiently trapped in cholesterol-mediated molecular complexes of sub-20 nm dimensions.[64] STED-FCS was also applied to study ternary lipid-cholesterol model membranes featuring microscopic liquid-liquid phase separation into Ld and Lo phases, without observing any direct evidence of the presence of nanoscopic domains at spatial scales down to 40 nm.[65]

Recently, Basu and coworkers detected dynamic heterogeneities at length scales of $\sim$ 100-150 nm in binary phospholipid-cholesterol bilayers of high cholesterol content (50 %) by applying STED-FCS with a resolution of $\sim$ 80 nm.[69] The occurrence of these heterogeneities in binary model membranes showing no

macroscopic phase separation indicates that the domain formation is driven by cholesterol packing and influenced by the phospholipid type. However, the high cholesterol content (50 %) used in the binary mixtures complicates a direct comparison to cellular membranes with a cholesterol content of 30-40 %.

A recent study reported on the lateral diffusion of a fluorescent cholesterol analogue in both model and cellular membranes exploiting STED-FCS and comparing the experimental results to molecular simulations.[70] It was shown that cholesterol diffuses faster than phospholipids in living cell membranes but only slightly faster in model membranes. On living cell membranes, cholesterol exhibited a two-component diffusion behavior indicating a heterogeneous diffusion behavior due to nanoscale interactions and asymmetric localization between the two leaflets of the membrane. These findings open up new questions regarding the role of cholesterol triggering cellular signaling together with proteins associated with a cholesterol-binding motif.

Overall, these and many other fundamental cell membrane questions point out how essential it is to have techniques at hand which offer high spatial (nm) and temporal (sub-ms) resolution simultaneously together with live cell compatibility and high throughput.

Trajectories of individual molecules diffusing on the membrane can be tracked using advanced SPT[3,15,71] and **high-speed SPT interferometric scattering microscopy (iSCAT)**.[72] **iSCAT** microscopy has quickly evolved and now routinely achieves nanometer localization precision together with microsecond time resolution by means of using 20-40 nm gold nanoparticles as labeling probes and sampling rates of up to 500 kHz (Figure 1-3).[73,74] Recently, it was reported that iSCAT together with extensive image processing is capable of following single unlabeled proteins with nanometer precision and microsecond time resolution in all three dimensions and over tens of minutes of acquisition.[75]

Wu et al. exploited iSCAT to conduct experiments using 20 nm gold beads attached to individual lipids in multicomponent model membranes.[76] In this work the traced lipids showed anomalous diffusion in the Lo phase consistent with the occurrence of nanoscale heterogeneities, while homogeneous lipid diffusion was observed in the Ld phase. The estimated sizes of the nanodomains in the Lo phase varied between 20 to 40 nm with lipid trapping times inside the domains below 1 ms. iSCAT thus constitutes an attractive tool to investigate dynamic biophysical

processes in mimetic systems at the nanoscale. Yet the major concern of this technique is associated to the potential artifacts related to the large size of the gold nanoparticle label with respect to the lipids under study. In addition, there is the concern that the multivalent streptavidin serving as linker potentially cross-links the target molecule.

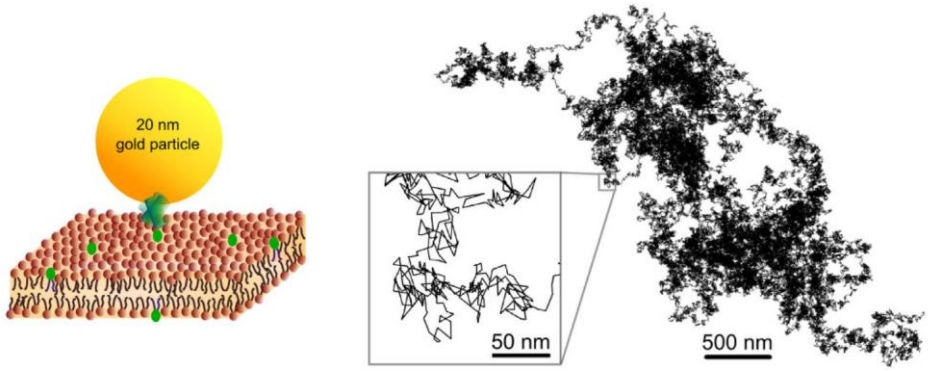

Figure 1-3. ***Principle of interferometric scattering microscopy (iSCAT).*** *Visualization of single lipid diffusion in a homogeneous lipid model membrane via high-speed iSCAT tracking with 3 nm spatial precision at 50 kHz. The schematics on the left shows a 20 nm gold nanoparticle attached to the headgroup of a single lipid molecule and tracked with high-speed iSCAT. On the right, exemplary diffusion trajectories are shown. Adapted from Ref. 76.*

A comparative study of probing lipid membrane dynamics with iSCAT and STED-FCS by attaching a fluorescent label to the gold particle showed that the observed diffusion behavior as well as relative differences in mobility yielded identical results for each approach separately.[77] However, the diffusion coefficients reported by STED-FCS were by a factor of 2-3 larger than the ones obtained by iSCAT. Overall, the authors claimed that despite a significant slow-down in diffusion on mimetic membranes as measured by iSCAT, no additional bias is introduced by the large and potentially cross-linking gold particles, at least at the spatial (> 40 nm) and temporal ($50 \leqslant t \leqslant 100$ ms) scales probed.

Thus, the iSCAT approach is perfectly suited and offers great value to quantitatively monitor the fast diffusion of lipids and proteins in mimetic membrane systems.[78] However, its extension to dynamic studies on the living cell membrane remains challenging. The main caveat is the high scattering (speckle-like) background of the living cell, which is impossible to correct and/or to compensate for. Only very recently the group of V. Sandoghdar was able to show first results of resolving the

nanoscale confinement of a transmembrane protein on a living cell based on a tremendous effort combining iSCAT with extensive data analysis.[75] This offers a promising glimpse into future directions to render live-cell experiments feasible with iSCAT.

1.3 Nanophotonic approaches to address the complexity of the cell membrane at the nanoscale

Beside these enormous progresses in super-resolution microscopy and single-molecule dynamics approaches, advances from the **nanophotonics** field have led to the concept of photonic nanostructures to confine light on a subwavelength scale and reach sub-diffraction observation areas in FCS.[79–81] A conceptually simple yet powerful approach uses single nanometric apertures milled in a metallic film also known as **zero-mode waveguides (ZMW)**, to confine the illumination spot directly in the sample plane (Figure 1-4).[82] Typically, the apertures have radii between 50 and 200 nm and are milled in an opaque aluminum film covering a glass coverslip.[83,84] Owing to their subwavelength radii, ZMWs sustain an exponentially decaying evanescent electromagnetic field acting as an efficient pinhole. This near-field profile translates into effective detection volumes three orders of magnitudes below the diffraction-limited confocal volume. Because of this large 3D confinement, ZMWs allow single-molecule detection at dye concentrations of ~ 1 µM[82], three to four orders of magnitude higher than confocal excitation.

ZMWs have been also combined with FCS to probe model lipid membranes[85,86] and living cell membranes[87–90], revealing, for instance, that fluorescent chimeric ganglioside proteins partition into 30 nm structures within the cell membrane.[90] While the ZMW approach is very efficient at confining light within circular hotspots of diameters between 100 to 200 nm, this technique faces difficulties regarding the signal-to-noise ratio and the attainable enhancement for spot sizes below 80 nm. Indeed, the FCS signal-to-noise ratio rapidly deteriorates for ZMW diameters below 100 nm as a consequence of fluorescence quenching induced by the metallic aperture edges and the low throughput of fluorescent photons due to the weak excitation fields.[91] The nanophotonic circular ZMW is the most simple and robust nanophotonic design to implement but provides modest fluorescent enhancement. As a consequence, an optimal diameter of about 120-150 nm depending on the employed metal was calculated in simulations and validated in experiments.[80,91] The enhancement factors obtained for ZMWs lie in the range of 5 to 25-fold in the best-case scenario of tuning the plasmonic properties of the nano-apertures.

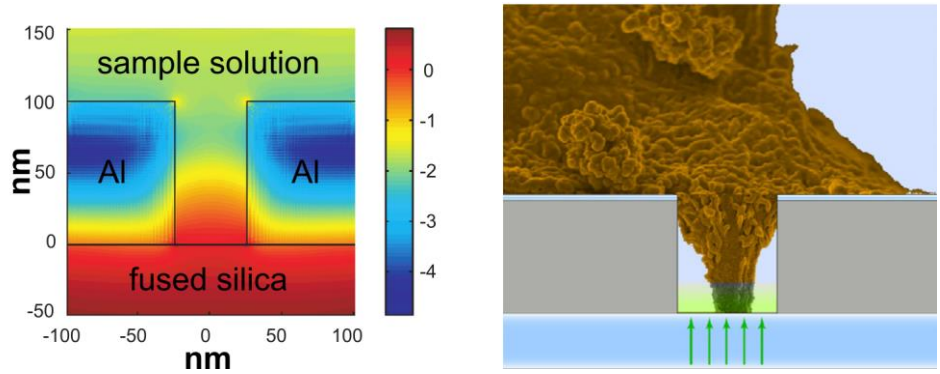

Figure 1-4. ***The pioneering nanophotonic approach to address the complexity of the cell membrane at the nanoscale.*** *On the left, the intensity distribution of a zero-mode waveguide (50 nm in diameter, 100 nm high) is plotted in log scale based on a 3D finite-element time-domain simulation. On the right, a cross-sectional cartoon of a cell invaginating into a ZMW (not drawn to scale) is displayed. In Ref. 88 the efficient excitation of the evanescent near-field was exploited to study the sources for membrane invaginations. The findings point towards cytoskeletal elements being responsible for the membrane invaginations, akin to filopodia extensions. Adapted from Refs. 82,88.*

In comparison, more sophisticated nano-antenna designs with sharp tips, edges and small gaps easily provide enhancement factors over 100-fold. An additional issue affecting the use of ZMWs for living cell membrane studies is the lack of control on the membrane invagination into the aperture. This problem has been addressed by introducing a planarization procedure in the nanofabrication process filling the aperture volume with fused silica.[92,93] Thanks to the absence of a height difference between the ZMW and the surrounding metal layer, the cells can rest on a nearly perfectly flat surface and are exposed to a homogeneous impinging electromagnetic illumination and thus enhancement. This homogeneous scenario is required to address the majority of membrane questions at the nanoscale. The best results achieved so far were reported in a nanospot diameter of 60 nm and microsecond resolution.[93] However, in the particular case of Ref. 88 the aim was to investigate the driving players for membrane invaginations and as sketched on the right in Figure 1-4. They explicitly triggered the membrane invaginations into the bottom of ZMWs and found that components of the cytoskeleton are the responsible elements similar to filopodia extrusions.

In the last decade, resonant **photonic nano-antennas** have been introduced to further enhance and confine the excitation light down to sub-20 nm scales.[94–96] Photonic nano-antennas are metallic (plasmonic) nanostructures that localize and

enhance the incident optical radiation into highly confined nanometric regions (plasmonic hotspots), leading to greatly enhanced light-matter interactions.[97,98] Depending on the material, shape and size of the nano-antenna, its resonance wavelength can be tuned within the visible electromagnetic spectrum.

With respect to biological applications, photonic nano-antennas are being exploited for the following two assets. First, photonic nano-antennas sustain a highly enhanced electromagnetic near-field leading to high fluorescent enhancement for fluorescent dyes with matching absorption spectra. Second, nano-antennas provide highly localized hotspots reducing the illumination volume by orders of magnitude into the regime of gap sizes below 50 nm compared to confocal spots of ≥ 250 nm. Over thousand-fold enhancement of the single-molecule fluorescence signal was reported with lithographically fabricated gold nano-antennas in the shape of bowties[99] (Figure 1-5 a), with dimers of gold nanoparticles assembled with DNA origami[100,101] and at the apex of single gold nanorods[102,103].

Recent advances in nanofabrication using colloid nanosphere lithography combined with plasma processing[103] and nanostencil lithography[104] currently enable large-scale production of reproducible nano-antennas with narrow gaps as required for the study of the plasma membrane of living cells. However, the applications of plasmonic antennas to living cells remain scarce. Plasmon-enhanced fluorescence was recently observed inside living bacterial cell membranes[105], highlighting the need to develop well-tuned substrates to maximize fluorescence enhancement and signal-to-noise ratio. In the highly active field of biosensing in the context of nanomedicine[106] plasmonic antennas have enabled the performance of Raman spectroscopy in a microfluidic device on the single cell level[107]and the detection of single amino acid mutations in breast cancer cells[108].

A major issue limiting the use of optical nano-antennas for living cell membrane studies is the efficient rejection of the background fluorescence light originating from the molecules that are significantly distanced (tens of nanometers) from the antenna hotspot but still within the diffraction limited confocal volume.[109] For antennas made of individual nanoparticles[110–114] or dimers of nanoparticles[115–117] deposited on a glass substrate, the fluorescence background can be significantly larger than the antenna-enhanced fluorescence signal from the plasmonic hotspot, challenging single-molecule detection and FCS using nano-antennas.

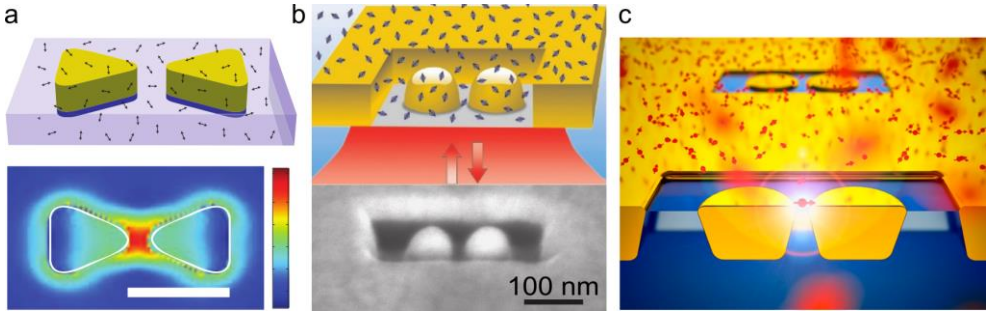

Figure 1-5. ***Evolution of nanogap antennas for enhanced FCS in biological samples.*** *(a)The pioneering gold bowtie antenna is sketched (upper panel) together with the simulated intensity distribution (bottom panel) showing the high field enhancement in the bowtie gap. (b) The initial «antenna-in-box» platform is shown (sketch and SEM scan) which allowed to perform single-molecule FCS at physiologically relevant dye concentrations in solution. (c) The planar gold nanogap antenna platform exploited in this dissertation is displayed. Adapted from Refs. 99,118,119, respectively.*

The initial approach to deal with this challenge employed low quantum yield emitters (quantum yield below 8 %) leading to maximizing the apparent fluorescence enhancement while minimizing the background.[113–115,117] Another solution relies on time gating and lifetime filtering, taking advantage of the reduced lifetime of the emitters in the vicinity of the plasmonic hotspot.[120]

A third approach, uses a dedicated antenna design termed "antenna-in-box".[118,121] The "antenna-in-box" platform features a metal dimer nanogap antenna centered inside a nano-aperture and is specifically designed for FCS and single-molecule analysis at physiologically relevant (µM) concentrations (Figure 1-5 b). The central nanogap antenna provides the nanoscale plasmonic hotspot, while the surrounding metal cladding screens the fluorescence background by preventing the excitation of the molecules diffusing away from the nanogap.[118]

A challenge associated with classical nanofabrication techniques such as focused ion beam milling or electron beam lithography is that the region of maximum field localization is buried into the nanostructure and not directly accessible for fluorescent emitters embedded in a membrane. We recently overcame this issue by combining electron beam lithography with planarization, etch back and template stripping.[119] The planarization strategy fills the aperture volume with a transparent polymer, yielding a flat top surface (of a planarity better than 3 nm), compatible with membrane studies on living cells (Figure 1-5 c). Possible curvature induced effects on the cell membrane are thus avoided.[92,93] The etch back approach

produces reproducible arrays of nano-antennas with controlled gap sizes and sharp edges.[119] With a gap size of 10 nm, the antenna gap area can be as small as 300 nm^2, realizing a reduction of 200× as compared to the diffraction-limited confocal area. Lastly, the template stripping flips the plasmonic hotspot to the top surface and places it in the immediate vicinity of the cell membrane. Owing to these nanofabrication advances, planar plasmonic nano-antennas drastically improve optical performance leading to fluorescence enhancement factors above 10 000× (for Crystal Violet dyes of 2 % quantum yield) and detection volumes in the zeptoliter range.

In this dissertation we exploit this innovative design of planar plasmonic nanogap antenna arrays embedded in nanometric-size boxes to address fundamental cell biological questions. Planar nanogap antenna platforms provide full surface accessibility of the hotspot-confined region. Hereby not only unwanted membrane curvature is prevented but more importantly it is possible to monitor single-molecule events on biological membranes at physiological relevant concentrations. By further combining this type of antennas with FCS, the diffusion of membrane components can be followed in time with ultrahigh spatiotemporal resolution. In the following section the challenges we decided to tackle during this PhD research are outlined.

1.4 Outline of the thesis

Throughout this PhD research the innovative planar "antenna-in-box" platform with different gap sizes, as introduced in the previous section, was employed for fundamental cell membrane studies. The overarching aim has been to exploit these planar plasmonic nanogap antenna arrays combined with FCS to probe nanoscale dynamics of biological membranes in their natural environment. Thus, the goal is to get one step closer to achieve a comprehensive insight into the underlying principles governing cell membrane organization, one of the most fundamental topics in cell biology.

Chapter 2 focuses on the fabrication of these planar gold nanogap antennas and the characterization of their performance in terms of electromagnetic field enhancement and confinement. The methodology of choice is FCS, which we take advantage of throughout this thesis. Hence, first we start with a detailed introduction to the principles of FCS and to our experimental implementation into a confocal setup. Second, we describe the different fabrication steps involved and

our characterization with electron microscopy and fluorescence spectroscopy. Finally, we demonstrate giant fluorescence enhancement factors of up to 10^4-10^5 times provided by our planar nanogap antennas and in ultra-confined detection volumes and single-molecule detection in the micromolar range.[119]

Subsequently in **Chapter 3** we apply these planar plasmonic nano-antennas in combination with FCS for assessing the dynamic organization of mimetic lipid membranes at the nanoscale.[121] First, we discuss the details of the preparation of mimetic membranes of different lipid compositions and the benchmarking experiments in confocal FCS. Next, we validate our preparation of mimetic membranes on our planar nanogap antenna platform to perform FCS experiments on three different gap sizes. For a ternary composition of the model membranes, we report on the emergence of transient nanoscopic heterogeneities coexisting in both macroscopically phase- separated lipid phases.[122]

In **Chapter 4** we increase in complexity regarding the biological system under study by adding a Hyaluronic Acid (HA) layer on top of the model lipid membranes to emulate the extracellular environment surrounding native biological membranes. Recently, there is emerging interest in studying the impact of constituents found on the extracellular side of the cell membrane such as the abundant glycosaminoglycan HA.[17,123]. For this study on multicomponent bilayers, we combined our nano-antenna-FCS approach with atomic force microscopy and spectroscopy. With our combined and extended approach, we reveal a distinct influence of HA on the nanoscale lipid organization of mimetic membranes composed of lipids constituting the more ordered lipid phase. We suggest a synergistic effect of HA and cholesterol on inducing and enhancing the formation of nanoscopic heterogeneities.

In **Chapter 5** we apply our planar nano-antenna platform combined with FCS to gain insight into the nanoscale dynamics of different lipids in living Chinese hamster ovary (CHO) cells.[124] We investigate the diffusion dynamics of fluorescent lipid analogs linked to either phosphoethanolamine (PE) or to sphingomyelin (SM) on living CHO cell membranes. With our nanogap antennas we were able to breach into the sub-30 nm spatial scale on living cell membranes for the first time. Together with cholesterol depletion experiments, we provide compelling evidence of short-lived cholesterol-induced ~ 10 nm nanodomain partitioning in plasma membranes and discuss the impact of these results in the context of lipid rafts.

In **Chapter 6** we explain in detail how we implemented a widefield illumination configuration together with sCMOS camera detection to demonstrate the multiplexing capabilities of our planar gold nanogap antenna platform combined with FCS. The recent advent of fast and sensitive imaging cameras is paving the way for Imaging FCS (ImFCS), a technique that takes advantage of the parallel acquisition of fluorescence from addressable areas on the camera.[126] By exploiting our nanogap antenna arrays to perform multiplexed FCS on 50 nano-antennas simultaneously, we show our results on benchmarking experiments with far-red fluorescent beads and resolve spatiotemporal heterogeneous diffusion proteins in living cells at the nanoscale.

Finally, in **Chapter 7** we summarize the main results of this thesis and provide an outlook for future research directions. In particular, we discuss potential novel antenna designs, new modes of excitation detection and ignite new questions to be addressed for pushing our knowledge of biology and beyond.

2 Planar gold nanogap antennas: Fabrication and Performance[2]

Optical nano-antennas have a great potential for enhancing light-matter interactions at the nanometer scale, yet fabrication accuracy and lack of scalability currently limit ultimate antenna performance and applications. In most antenna designs, the region of maximum field localization and enhancement (i.e. hotspot) is not readily accessible to the sample because it is buried into the nanostructure. Moreover, current large-scale fabrication techniques lack reproducible geometrical control below 20 nm.

In this chapter, we describe a new nanofabrication technique, which applies planarization, etch back, and template-stripping to expose the excitation hotspot at the surface, providing a major improvement over conventional electron-beam lithography approaches. We show the fabrication of large flat surface arrays of planar nano-antennas featuring gaps as small as 10 nm with sharp edges, excellent reproducibility and full surface accessibility of the hotspot confined regions. We further demonstrate that this novel fabrication approach drastically improves the optical performance of plasmonic nano-antennas to yield giant fluorescence enhancement factors up to 10^4 -10^5 times, outperforming previous plasmonic antenna realizations. This method is fully scalable and adaptable to a wide range of antenna designs.

---

[2]The content of this chapter has been partially published in:

Flauraud, V., Regmi, R., **Winkler, P.M.**, Alexander, D.T., Rigneault, H., van Hulst, N.F., García-Parajo, M.F., Wenger, J. and Brugger, J., *In-plane plasmonic antenna arrays with surface nanogaps for giant fluorescence enhancement.* Nano Letters, 17(3), pp.1703-1710.

In the following chapters, we will show applications of this type of planar nanogap antenna arrays to study the spatiotemporal organization of biological membranes with unprecedented ultra-high spatiotemporal resolution.

2.1 Introduction

The working principle of plasmonic nano-antennas is to take advantage of the plasmonic response of noble metals to strongly confine light energy into nanoscale dimensions and breach the classical diffraction limit.[95,96,125] This confinement leads to a drastic enhancement of the interactions between a single quantum emitter and the light field,[126–129] enabling large fluorescence gains above a thousand fold,[99–103,118] ultrafast picosecond emission[130–132] and photobleaching reduction.[133,134] With a view to biological applications, the two main advantages of plasmonic antennas are: first, the enhanced electromagnetic field leading to large fluorescent enhancement and second, the high field localization into confined nanometric hotspots allowing for impressive reductions of the illumination volume. Together, this ensures the detection of single molecules at physiologically relevant micromolar concentrations.[79,80,82]

Biological applications of nano-antennas require the large-scale availability of narrow accessible gaps. Not only should nanogaps with sub-20 nm dimensions be reproducibly fabricated, but also the gap region (plasmonic hotspot) must remain accessible to probe fluorescently labeled molecules diffusing within a membrane and preventing undesired membrane curvature. Despite impressive recent progress using electron beam[135], focused ion beam[136] or stencil lithographies[104,137,138], or alternatively with bottom-up self-assembly techniques[100,117,128–130,139–141], the challenges of reliable narrow gap fabrication and hotspot accessibility remain major hurdles limiting the impact and performance of plasmonic nano-antennas. For instance, when aiming for the fabrication of aperture antennas, electron beam lithography (EBL) using a positive-tone resist requires metal dry etching, which produces high line-edge roughness that is not suited for the definition of reliable and high aspect ratio nanogaps. Alternatively, patterning openings in metal films relying on EBL and negative-tone resist demands a lift-off approach. This is an efficient approach when lifting a full metal film for fabricating single particles but can be arduous when removing small isolated clusters of metal to clear apertures.

In this chapter we describe a novel nanofabrication technique based on EBL followed by planarization, etch back and template stripping. The process provides large arrays of planar nano-antennas featuring 10 nm gaps with sharp edges and full accessibility of the localized hotspot illumination provided by the antenna gap. We further characterize the performance of these antennas by means of

fluorescence correlation spectroscopy of individual molecules in solution. As such are these planar antenna arrays ideally suited for research on model and living cell membranes, as it will be shown in the subsequent chapters of this thesis.

2.2 Methods

In this section, the methods used for this PhD project to fabricate and benchmark the performance of the planar nano-antennas are outlined in detail. Note that some of the methods and theoretical principles have been used throughout the different PhD research topics. In this Methods section, the theoretical and experimental principles of fluorescence correlation spectroscopy are introduced at first. Next, we introduce the basics of single-molecule detection, highlighting those properties that are modified by the interaction between single molecules and nano-antennas. The final paragraphs of this section comprise the details of the experimental realizations.

2.2.1 Principles of Fluorescence Correlation Spectroscopy (FCS)

As introduced in Chapter 1, FCS has been broadly applied to probe the mobility and interaction behavior of fluorescently tagged (bio)molecules diffusing in and out of a confocal detection volume (Figure 2-1).[142,143] By diluting the concentration of the target molecules down to the pM range, fluorescence fluctuations recorded over time reveal the characteristic diffusion properties of individual molecules. This condition to achieve single-molecule detection for FCS in a diffraction-limited confocal spot is significantly more challenging to attain in the crowded environment of living cells. Therefore, the common approach has been to under-label the molecule of interest. A different approach to reach single-molecule sensitivity at physiologically relevant concentrations while simultaneously guaranteeing a reliable signal-to-background ratio, are plasmonic nano-antennas. The challenges as well as the insights into fundamental biological questions obtained by combining nano-antennas with FCS are extensively discussed in this dissertation.

Nonetheless, the theoretical and experimental principles of FCS in confocal as well as with nano-antennas are explained first. The integral parts of a confocal FCS setup are an excitation laser focused on the sample through a high NA objective. Once a fluorescently labeled molecule diffuses through the focused illumination spot, it becomes excited and its fluorescent emission is separated from the excitation laser via a dichroic mirror and additional filters. The confocal z-sectioning is achieved

through a correctly placed pinhole in the detection arm. The emission is collected by a detector, which is most commonly implemented by splitting the emission onto two avalanche photon diodes (APDs). The fluorescent emission or fluctuations of the molecules diffusing through the illumination volume are recorded in time (Figure 2-1 b).

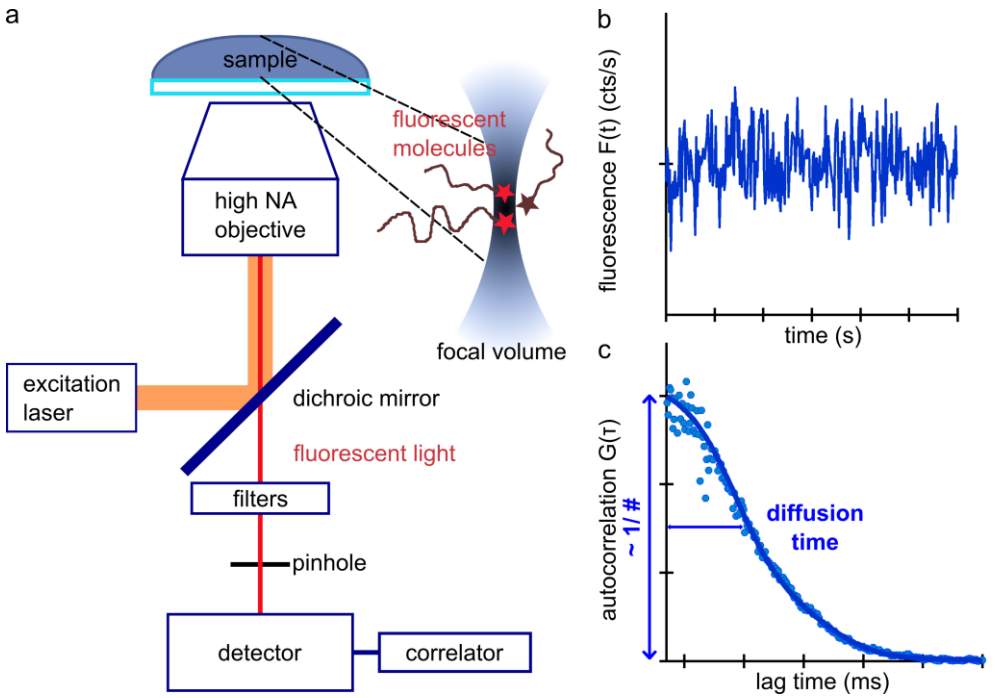

Figure 2-1. ***Fluorescence Correlation Spectroscopy (FCS) in a confocal configuration.*** *The scheme of a typical confocal FCS setup is shown in (a). Within the illumination volume in the sample plane, the fluorescent molecules are diffusing in and out, giving rise to fluorescent fluctuations which are collected back in reflection mode through the same high NA objective, separated from the excitation laser light by a dichroic mirror and filters, and detected through a pinhole. The fluorescent fluctuations are recorded over time (b) and then the corresponding autocorrelation curve is calculated (c). From this autocorrelation curve the number of molecules and characteristic diffusion time, i.e., the time the fluorescent molecules require to transit the illumination volume, can be extracted.*

Autocorrelation curves are then generated over multiple trajectories (Figure 2-1 c). The autocorrelation curves contain relevant information about the dynamics of the diffusing molecules. From these curves quantitative information such as the diffusion time and mode, chemical reaction rates, hydrodynamic radii as well as the average number of molecules can be extracted. In particular, the diffusion time, i.e.,

the time it takes for a molecule to traverse the illumination volume, can be directly estimated at half of the amplitude of the autocorrelation function (see Figure 2-1 c). In addition, the apparent number of molecules within the illumination volume can be extracted from the inverse of the autocorrelation curve at a lag time equaling zero (see Figure 2-1 c).

In the case of single-molecule experiments it is valid to assume that all occurrences affecting the diffusion of the molecule during the measurement time are encoded in the fluorescence intensity time traces. The challenge is to obtain a reliable signal-to-noise ratio (SNR). The statistics and hence the number of molecules diffusing randomly in and out of a detection volume are represented by a Poisson distribution, with the sample variance equaling the average number $\langle(\boldsymbol{\delta N})^{\boldsymbol{2}}\rangle = \langle \boldsymbol{N}\rangle$. The average or mean intensity of the detected fluorescence fluctuation intensity is directly proportional to the number of molecules $\langle \boldsymbol{F}\rangle = \boldsymbol{\alpha}\langle \boldsymbol{N}\rangle$, assuming a proportionality factor $\boldsymbol{\alpha}$. Consequently,

$$\langle(\boldsymbol{\delta F})^{\boldsymbol{2}}\rangle = \boldsymbol{\alpha}^{\boldsymbol{2}}\langle(\boldsymbol{\delta N})^{\boldsymbol{2}}\rangle = \boldsymbol{\alpha}^{\boldsymbol{2}}\langle \boldsymbol{N}\rangle \quad \textbf{Eq. 2-1}$$

and after normalization:

$$\frac{\langle(\boldsymbol{\delta F})^{\boldsymbol{2}}\rangle}{\langle \boldsymbol{F}\rangle^{\boldsymbol{2}}} = \frac{\boldsymbol{1}}{\langle \boldsymbol{N}\rangle}. \quad \textbf{Eq. 2-2}$$

An important remark is that the concentration is also directly proportional to the average number of particles and hence can be simultaneously deduced from the measured fluorescence intensity.

Switching to the case of a FCS experiment under constant excitation laser power conditions, the fluorescence fluctuations $\boldsymbol{\delta F(t)}$ are defined as deviations from the temporal average of the detected signal over the time $\boldsymbol{T}$,

$$\boldsymbol{\delta F(t) = F(t) - \langle F(t)\rangle \text{ with } \langle F(t)\rangle = \frac{1}{T}\int_0^T F(t)dt.} \quad \textbf{Eq. 2-3}$$

For a single molecule diffusing in equilibrium conditions, the fluorescence fluctuations may arise from changes in its absorption cross-section ($\boldsymbol{\delta\sigma}$), quantum yield ($\boldsymbol{\delta\phi}$) and or local concentration variations in the detection volume $\boldsymbol{\left(\delta C(\vec{r},t)\right)}$ and in summary $\boldsymbol{\delta\left(\sigma\phi C(\vec{r},t)\right)}$. Thus, the detected deviations in the fluorescence signal are described as:

$$\delta F(t) = \kappa \int_V I_{exc}(\vec{r})\, S(\vec{r}) \delta\big(\sigma \phi C(\vec{r}, t)\big)\, dV \quad \textbf{Eq. 2-4}$$

with κ being the detection efficiency, $S(\vec{r})$ the optical transfer function and the excitation intensity distribution $I_{exc}(\vec{r})$, with its maximum at I_0 and V being the detection volume.

To simplify, we introduce the convolution function $W(\vec{r}) = I_{exc}(\vec{r})/I_0 * S(\vec{r})$, which is typically approximated by a three-dimensional Gaussian function.

$$\delta W(\vec{r}) = e^{-2\frac{(x^2+y^2)}{r_0^2}} e^{-2\frac{z^2}{z_0^2}} \quad \textbf{Eq. 2-5}$$

This 3-D Gaussian decays to $1/e^2$ at r_0 and z_0 in the lateral and axial directions, respectively. Further, we use the brightness or photon count rate per molecule per second:

$$Q = \kappa \phi \sigma I_0 \quad \textbf{Eq. 2-6}$$

leading to:

$$\delta F(t) = \int_V W(\vec{r})\, \delta\big(QC(\vec{r}, t)\big)\, dV \quad \textbf{Eq. 2-7}$$

with the definition of the normalized autocorrelation function (ACF) $G(\tau)$ being:

$$G(\tau) = \frac{\langle \delta F(t) \delta F(t+\tau) \rangle}{\langle F(t) \rangle^2}. \quad \textbf{Eq. 2-8}$$

We compute $G(\tau)$ from the fluorescence signal with respect to its self-similarity after a given lag time τ. Thus, the normalized variance of the signal of the fluorescence fluctuation $\delta F(t)$ yields the ACF amplitude $G(0)$.

Inserting **Eq. 2-8** we obtain:

$$G(\tau) = \frac{\iint W(\vec{r}) W(\vec{r}') \langle \delta\big(QC(\vec{r}, t)\big) \delta\big(QC(\vec{r}', t+\tau)\big) \rangle dV dV'}{\left(\int W(\vec{r}) \langle \delta\big(QC(\vec{r}, t)\big) \rangle dV\right)^2}. \quad \textbf{Eq. 2-9}$$

We can separate the fluctuation term: $\boldsymbol{\delta(QC(\vec{r},t))} = \boldsymbol{C\delta Q + Q\delta C}$, and assuming that the properties of the fluorescent molecule are constant over the duration of the measurement, $\boldsymbol{\delta Q = 0}$, we further simplify to:

$$\boldsymbol{G(\tau) = \frac{\iint W(\vec{r})W(\vec{r}')\langle \delta C(\vec{r},0)\delta C(\vec{r}',\tau)\rangle dV dV'}{(\langle C\rangle \int W(\vec{r})\, dV)^2}}. \quad \textbf{Eq. 2-10}$$

Since we are looking at a molecule diffusing freely in 3D ($\boldsymbol{n = 3}$) with a diffusion coefficient **D** we can replace

$$\langle \boldsymbol{\delta C(\vec{r},0)\delta C(\vec{r}',\tau)}\rangle =$$

$$\langle \boldsymbol{C}\rangle \frac{\boldsymbol{1}}{\boldsymbol{(4\pi D\tau)^{-n/2}}} \boldsymbol{e^{-\frac{(\vec{r}-\vec{r}')^2}{4D\tau}}} \overset{\boldsymbol{n=3}}{\longrightarrow} \langle \boldsymbol{C}\rangle \frac{\boldsymbol{1}}{\boldsymbol{(4\pi D\tau)^{-3/2}}} \boldsymbol{e^{-\frac{(\vec{r}-\vec{r}')^2}{4D\tau}}} \quad \textbf{Eq. 2-11}$$

and we establish $\boldsymbol{\tau_D}$ as the characteristic diffusion or transit time of the molecule diffusing through the detection volume which is related to the diffusion coefficient as:

$$\boldsymbol{\tau_D = \frac{r_0^2}{4D}} \quad \textbf{Eq. 2-12}$$

and the effective confocal detection volume is specified as:

$$\boldsymbol{V_{eff} = \frac{(\int W(\vec{r})dV)^2}{\int W^2(\vec{r})dV} = \pi^{\frac{3}{2}} r_0^2 z_0}. \quad \textbf{Eq. 2-13}$$

Hence, we obtain the ACF for one species of molecule diffusing freely in 3D:

$$\boldsymbol{G(\tau) = \frac{1}{\langle C\rangle V_{eff}} \frac{1}{1 + \tau/\tau_D} \frac{1}{\sqrt{1 + (r_0/z_0)^2(\tau/\tau_D)}} =}$$

$$\boldsymbol{= \frac{1}{\langle N\rangle} \frac{1}{1 + (\tau/\tau_D)} \frac{1}{\sqrt{1 + (s)^2(\tau/\tau_D)}}} \quad \textbf{Eq. 2-14}$$

with $\boldsymbol{\langle N\rangle = \langle C\rangle V_{eff}}$ denoting the average number of molecules and $\boldsymbol{s = r_o/z_0}$ the ratio of the lateral to the axial dimension of the detection volume.

With a careful calibration of the detection volume at the beginning of the experiment the values of $\boldsymbol{r_o}$ and $\boldsymbol{z_o}$ can be determined. So, we finally recognize that

the amplitude of the ACF at zero lag time is inversely proportional to the average number of molecules in the detection volume $\mathbf{G(0) = 1/\langle N \rangle}$.

Over the course of this PhD research we often detect the fluorescence intensity of the red Alexa 647N dye, which has many advantageous properties, but it is also prone to transit to the dark triplet state with a probability of 0.3. Thus, the assumption that the count rate of the fluorophore (**Eq. 2-6**) is constant over the duration of the measurement ($\boldsymbol{\delta Q = 0}$) is not accurate anymore and is accounted for by a simple exponential decay for the triplet state, which improves the fitting satisfactorily already:

$$\boldsymbol{G(\tau) =}$$

$$\boldsymbol{= \frac{1}{\langle N \rangle}\left(1 - \frac{\langle B \rangle}{F}\right)^2 \left[1 + \eta_T e^{-\frac{\tau}{\tau_{bt}}}\right] \frac{1}{1 + (\tau/\tau_D)} \frac{1}{\sqrt{1 + (s)^2(\tau/\tau_D)}}} \qquad \textbf{Eq. 2-15}$$

adding the background noise $\langle \boldsymbol{B} \rangle$, the amplitude $\boldsymbol{\eta_T}$ and blinking time $\boldsymbol{\tau_{bt}}$ of the dark triplet state population. Note that this fitting is used to routinely calibrate the confocal detection volume.

The last addition to the toolbox of describing the diffusion behavior frequently observed during this research is the correlation curve of a 2D Brownian motion. When probing within a 2D surface we assume $\boldsymbol{z_0 \gg r_o}$ and in **Eq. 2-11** we replace $\boldsymbol{n}$ = **2**. Thus, in model and living cell membranes we encounter that the mobility of molecules is confined into two dimensions, so that:

$$\boldsymbol{G(\tau) = \frac{1}{\langle N \rangle}\left(1 - \frac{\langle B \rangle}{F}\right)^2 \left[1 + \eta_T e^{-\frac{\tau}{\tau_{bt}}}\right] \frac{1}{1 + (\tau/\tau_D)}} \qquad \textbf{Eq. 2-16}$$

The last three equations describing the ACFs, i.e., **Eq. 2-14, Eq. 2-15, Eq. 2-16**, are exploited as fitting models to quantify the diffusion properties of the molecules studied in the FCS experiments. In our work we focus on determining the characteristic diffusion time and the correlation amplitude at zero lag time (which is inversely proportional to the average number of molecules). Depending on the system under study we choose the appropriate ACF to fit the experimental data.

As described below in detail, the nano-antennas used during this PhD research are based on a "antenna-in-box" geometry with a dimer nanogap antenna centered inside a nano-aperture, i.e., box (see also Figure 1-5 b, c). The central nanogap antenna provides the nanoscale plasmonic hotspot, while the nano-aperture reduces the fluorescence background by preventing excitation of the molecules outside the nanogap.[118] When treating the fluorescence data obtained with nano-antennas, we acknowledge that the description of a Gaussian profile for the light confined at the antenna hotspot, does not hold. However, in contrast to earlier works on plasmonic antennas which required a special data fitting procedure[117,118] including two species of fluorophores with different numbers of molecules and brightness, we apply a two-component ACF fitting of the diffusion behavior (**Eq. 2-14, Eq. 2-15, Eq. 2-16**) best describing the diffusion dynamics under study.[119,122,124] The first component of the ACF fit results from the enhanced fluorescent counts of molecules diffusing through the nanogap and yields a faster diffusion time than the second component accounting for the background contribution. The second fit component yielding longer diffusion times is similar to the confocal excitation as well as to the two control cases of measuring on the nano-aperture without the antenna (approximately the size of a diffraction-limited spot) or when the excitation polarization is shifted by 90°, so that the antenna is no longer in resonance. We set the condition that the sum of both components equals the total fluorescence intensity. In our case, the signal from the hotspot of the planar nanogap antennas largely dominates over the background. Without any additional correction factor for the detection volume and keeping the Gaussian profile assumption, we obtain fitting results matching our expectations. Namely, the diffusion time across the gap linearly increases with increasing gap size. In contrast, we observe a decreasing correlation amplitude at zero lag time with increasing gap size corresponding to few molecules transiting the gap and thus a reduction of the detection volume.

2.2.2 Influence of nano-antennas on the fluorescent properties of single emitters

The fundamental diffraction limit of light sets the boundary for the minimal confinement of propagating electromagnetic fields (e.g. light) to roughly half of its wavelength when using conventional optics. In contrast, photonic nano-antennas efficiently squeeze the light to nanometric dimensions significantly defying the diffraction limit.[95,144] The choice of the metallic composition and geometrical design defines the properties of a nano-antenna such as the wavelength of its plasmonic

resonance lying in the visible spectrum. The near-field is directly proportional to the surface charge density. Sharp curvatures or tips of a metal surface exhibit an increased surface charge density. Thus, sharp tips and edges of a nano-antenna will exhibit a local increase of surface charge density affording hotspots of enhanced near-field.

A single emitter (e.g. fluorescent dye molecule) coupling to the near-field of impinging optical radiation (e.g. laser light excitation) strongly experiences the presence of a nano-antenna.[145] Namely, the nano-antenna influences both, the effective excitation of the molecule via near-field enhancement and the decay rates of the fluorescence emission. The details of the modulations on the properties of the emitters due to the presence of the nano-antenna are discussed below.

At the hotspot of the antenna, the locally enhanced near-field increases the absorption rate for the single emitter provided that the absorption spectrum of the emitter matches with the plasmonic resonance. The degree of the near-field enhancement further depends on the position and orientation of the emitter with respect to the nano-antenna.[146]

Once the incident radiation is absorbed by the emitter, its electrons are excited from the ground state to populate a higher energy state. From this excited transient state, the electrons relax back into the stable ground state via radiative or non-radiative emission.[143] Further non-radiative relaxation pathways are internal conversion ($\boldsymbol{\Gamma_{ic}}$), intersystem crossing ($\boldsymbol{\Gamma_{isc}}$) and triplet state de-excitation ($\boldsymbol{\Gamma_{ph}}$). The sum of the relaxation mechanisms from the excited down to the ground state via radiative ($\boldsymbol{\Gamma_{rad}}$) or non-radiative emission ($\boldsymbol{\Gamma_{nr}}$) is called the total de-excitation rate $\boldsymbol{\Gamma_{tot}}$ and is inversely proportional to the characteristic fluorescence lifetime of the emitter

$$\boldsymbol{\tau = \frac{1}{\Gamma_{rad} + \sum \Gamma_{nr}} = \frac{1}{\Gamma_{tot}}.} \quad \textbf{Eq. 2-17}$$

This characteristic fluorescent lifetime $\boldsymbol{\tau}$ is highly sensitive to the local environment. Thus, the presence of a nano-antenna in close proximity to the emitter will significantly modify its fluorescence lifetime. For instance, it can potentially alter the radiative rate of the molecule $\boldsymbol{\Gamma_{rad}}$ by modifying the local density of states (LDOS)[146], and/or opening up additional non-radiative decay channels $\boldsymbol{\Gamma_{nr}}$ due to metallic losses $\boldsymbol{\Gamma_{loss}}$ of the nano-antenna.[147]

Another parameter quantifying the excitation and relaxation process of an emitter is the fluorescent quantum yield $\boldsymbol{\phi}$. $\boldsymbol{\phi}$ refers to the number of photons emitted with respect to the number of absorbed photons, i.e., the efficiency of radiative events. Relating to the previously introduced rates in **Eq. 2-17**, the fluorescent quantum yield is defined as the rate of photon emission events over the summed rate constants of all de-excitation channels as:

$$\boldsymbol{\phi = \frac{\Gamma_{rad}}{\Gamma_{rad} + \sum \Gamma_{nr}}.} \quad \textbf{Eq. 2-18}$$

Denoting $\boldsymbol{\kappa}$ as the light collection efficiency and assuming steady-state excitation, the collected count rate per fluorescent molecule, also known as brightness per molecule, can be described as:

$$\boldsymbol{Q = \frac{\kappa \phi \sigma I_{exc}}{1 + I_{exc}/I_{sat}}} \quad \textbf{Eq. 2-19}$$

with $\boldsymbol{\sigma}$ being the excitation cross section of the emitter, $\boldsymbol{I_{exc}}$ the excitation intensity and the saturation intensity $\mathbf{I_{sat} = \Gamma_{tot}/\sigma\left(1 + \Gamma_{isc}/\Gamma_{ph}\right)}$. At low excitation conditions $[\boldsymbol{I_{exc} \ll I_{sat}}]$, the collected count rate simplifies to $\boldsymbol{Q = \kappa \phi \sigma I_{exc}}$ resulting in **Eq. 2-6** as introduced above.

Once the excitation intensity equals or exceeds the saturation intensity, the count rates no longer scale linearly with the excitation intensity. This regime should be avoided by all means for fluorescence experiments in biological systems due to phototoxic damage of biomolecules, living cells and tissue.

The last important parameter to be introduced is the fluorescent enhancement factor $\boldsymbol{\eta_F}$, which can be expressed as:[146,148]

$$\boldsymbol{\eta_F = \frac{Q^*}{Q_{conf}} \sim \frac{\phi^* \sigma^*}{\phi_{conf} \sigma_{conf}}} \quad \textbf{Eq. 2-20}$$

with $\boldsymbol{Q^*}$ being the brightness per molecule, quantum yield $\boldsymbol{\phi^*}$ and absorption cross section $\boldsymbol{\sigma^*}$ in presence of the nano-antenna and $\boldsymbol{Q_{conf}}$, $\boldsymbol{\phi_{conf}}$ and $\boldsymbol{\sigma_{conf}}$, the ones in the confocal detection volume, i.e., in the absence of the nano-antenna. As indicated in **Eq. 2-20** the enhancement factor $\boldsymbol{\eta_F}$ leading to a gain in the collected count rate or brightness per molecule in the presence of a nano-antenna obtained in experiments mainly arises due to

- enhanced local near-field excitation increasing the effective absorption of the emitter
- increased fluorescent quantum yield of the emitter (avoiding emitter – antenna coupling that could lead to quenching).

These contributions can be adjusted and tuned collectively or independently by a careful choice of the nano-antenna design and the fluorescent dye. Any increased contribution results in an enhanced fluorescent count rate per molecule. With regard to the nano-antenna design, the desirable choices include sharp tips or narrow gaps ensuring highly localized excitation enhancement and easy access to the excitation hotspot. But the tuning range for the fluorescent dye should not be neglected in the experiment design. Higher fluorescent enhancement factors are achieved with initially low quantum yield dyes (i.e., in the absence of the nano-antenna) since in this case the competition between the radiative and non-radiative decay channels of the molecule can be tuned to favor increased emission.

2.2.3 Time Correlated Single-Photon Counting (TCSPC)

TCSPC is a sensitive method to measure the fluorescent lifetime of emitters with extremely high temporal resolution, typically a few ps. This technique detects single photons with high precision in the time domain and is broadly applied for fluorescence lifetime imaging[149] and/or to determine the Förster resonance energy transfer (FRET) efficiency between close-by emitters.[150] TCSPC is based on pulsed laser excitation at high repetition rate.[151] Each pulse excites the emitter to a higher energy level and probes the rate of the bright and dark de-excitation pathways as explained in the Section 2.2.2.

Every TCSPC measurement extends over a multitude of pulsed excitation cycles to build up the characteristic histogram of the photon arrival time at the detector with enough statistics. This histogram is actually a probability distribution and can be fitted with a single exponential decay (assuming a Poisson distribution of the photon arrival times) to extract the molecular fluorescence decay rate/lifetime.

In relation to this PhD research we exploit the TCSPC approach to evaluate how nano-antennas influence the radiative and non-radiative rates of individual molecules via the measurement of their fluorescence lifetime.

2.2.4 Experimental setup for fluorescence spectroscopy

The experiments have been performed using an inverted confocal microscope with a Zeiss 40×, 1.2 NA water-immersion objective and a three-axis piezoelectric stage allowing to select individual nano-antennas at the Institut Fresnel in Marseille in the group of Prof. H. Rigneault and in collaboration with Dr. J. Wenger. The excitation for FCS and fluorescence burst experiments was provided by a linearly polarized He-Ne laser at 633 nm. For fluorescence lifetime measurements, the excitation source was a picosecond laser diode operating at 636 nm and 80 MHz repetition rate (*Pico-Quant LDH-P-635*). The fluorescence signal was collected in epi-detection mode through a dichroic mirror and a stack of two long-pass 650 nm filters to reject the backscattered laser light and maximize fluorescence collection. The detection was performed by two avalanche photodiodes (*PicoQuant MPD-5CTC*) after passing through a 30 µm pinhole conjugated to the focus plane. The fluorescence time traces for burst analysis and lifetime histograms were recorded on a fast time-correlated single photon counting module in time-tagged time-resolved mode (*PicoQuant PicoHarp 300*). The concentration of fluorescent molecules was measured with extinction spectroscopy and confirmed by confocal FCS experiments on a series of dilutions. In the photon count histograms, we determine the peak fluorescence intensity by the intercept of the fitted exponential decay with the x-axis at 100. Events of lower probabilities within the 30 s experiment duration and events lying above this level (corresponding to the presence of two molecules within the hotspot) are discarded. The temporal fluctuations of the fluorescence intensity F(t) were analyzed with a hardware correlator (*Flex02-12D/C correlator.com, Bridgewater NJ*) to compute the temporal correlation of the fluorescence signal.

2.2.5 Fabrication of planar nano-antenna arrays with different gap sizes

The fabrication of the nano-antenna arrays used during this research was performed at the EPFL in the group of Prof. J. Brugger within the framework of a European collaboration.

Silicon wafers (100 mm diameter, prime grade) were cleaned following the standard RCA-1/2 procedure prior to the low-pressure chemical vapor deposition of 100 nm-thick silicon nitride. Hydrogen silsesquioxane (HSQ) 4% (*Dow Corning*) was spun at 1500 rpm for 240 seconds yielding an approximately 100 nm-thick coating. The samples were then exposed by electron beam lithography (*VISTEC*

EBPG5000+, 100 kV) using a 1 nm grid and a 2 nA beam (5 nm FWHM). Short range dose corrections were used to increase feature accuracy and reliably pattern the sub-10nm features that define the narrowest gaps. After exposure, the samples were developed at room temperature in 25% tetramethylammonium hydroxide (TMAH) for two minutes, rinsed in deionized water and isopropanol prior to drying in order to avoid capillary force induced collapse of the narrowest features. A gold layer of 50 nm thickness was then evaporated by electron beam heating at a pressure of 8×10^{-7} mBar on static substrates ensuring normal incidence of the metal flux. The stage was cooled at -50 °C throughout the evaporation (*Huber Unistat 705w*) to ensure small grain size allowing for high feature accuracy.

In order to planarize the sample, flowable oxide (*Dow Corning FOX-16*) was then spun at 1000 rpm for 240 seconds yielding a 1 µm-thick film with a residual topography above the structures of interest below 10 nm. Broad argon ion beam milling (*Veeco Nexus IBE350*) performed at -45° sample tilt was then used to etch back the flowable oxide until the top gold caps were fully etched. End-point detection was performed by monitoring the gold signal on a secondary ion mass spectrometer. A 30 second etch with hydrofluoric acid diluted 1:10 in deionized water was used to clear out the residual HSQ in the antenna apertures. The wafer was then cleaved into individual dies.

For template stripping, microscope coverslips (30 mm diameter, 150 µm thickness) were cleaned in piranha solution and surface activated by oxygen plasma (*Tepla Gigabtach 1000W, 500 SCCM O2*). Then the coverslips were brought into contact with the gold substrates with a small drop of UV curable OrmoComp (*Microresist Technology GmBH*) and cross-linked under UV and light pressure *(ESCO EUN-4200 375nm, 2.5mW/cm²*) for 3 minutes followed by separation of the glass from the silicon with a razor blade. Additional samples were fabricated to perform high resolution metrology and EELS characterization following a similar process without template stripping. The TEM membranes were fabricated at wafer-scale by using 30 nm LPCVD silicon nitride that was released in 100 × 500 µm² windows from the backside by potassium hydroxide wet etching.

2.2.6 Metrology and statistics of gap sizes

Sample imaging was performed by scanning electron microscopy (*Zeiss Merlin*) to measure the features before (20 kV, 360 pA, 1mm working distance and in-lens detector) and after template stripping (2 kV, 80 pA, 3 mm working distance and in-

lens detector). Topography was measured by atomic force microscopy (*Bruker FastScan*) in both *ScanAsyst PeakForce* tapping and tapping mode. For high resolution metrology statistics, imaging was performed both in TEM and STEM mode (*FEI Talos*) and processed with a custom *Matlab* toolbox.

2.2.7 EELS measurements and data processing

STEM-EELS maps were acquired using a *FEI Titan Themis 60-300* equipped with a Wien-type monochromator and a *Gatan GIF Quantum ERS* spectrometer. A 300 keV incident electron beam was used for all experiments, monochromated to give an energy spread of ~110 meV FWHM in the zero-loss peak of elastically-scattered electrons, and with beam currents of ~240 pA. A 17 mrad convergence semi-angle of the probe and a 22 mrad collection semi-angle on the spectrometer were used, with the probe having a mean diameter of < 1 nm for full width at tenth maximum in incident intensity. Mapping was performed using the "ultrafast" spectrum imaging mode with typical dwell times of 0.20 to 0.26 ms per pixel, and with the probe rastered in (x, y) step sizes of 0.5–0.6 nm for a total of > 105 pixels per map. Each map was treated with the *HQ Dark Correction* plugin to reduce noise associated with dark current subtraction.

The EELS data cubes were processed using *Gatan Digital Micrograph* and custom *Matlab* scripts for the removal of the background from the tails of the zero-loss peak (ZLP), extraction of point spectra and spatial EELS maps. The ZLP was first centered pixel by pixel using a Gaussian-Lorentzian approximation. Following zero-loss alignment, each data cube was spectrally cropped to the region of interest including ZLP (-2 to 4 eV), and artifacts from cosmic rays were removed. To account for the absorption and scattering inside the Au film, the data cubes were normalized by dividing each pixel-spectrum by the integrated zero-loss fit. Spectra were integrated over a 30 × 30 pixel region of interest centered around the point overlaid on the STEM image, whereas EELS maps were typically integrated over a window of 0.06 eV in energy range. All of the experiments described in Section 2.3 for Figure 2-2, Figure 2-3 and Figure 2-4 were performed at the EPFL by our collaborators prior to the transfer of the antennas to us.

2.3 Results and Discussion

Our novel antenna design is based on the "antenna-in-box" platform featuring a nanogap dimer antenna inside a nanobox.[118,121] This design is especially tailored for enhanced single-molecule analysis in solutions at high concentrations. It combines

a central nanogap antenna between two 80 nm gold half-spheres to create the hotspot used for fluorescence enhancement, and a cladding 300 × 140 nm^2 box, to screen the background by preventing direct excitation of molecules diffusing away from the nano-antenna gap.

Figure 2-2 a summarizes the different steps of our fabrication process. First, we use EBL on a negative tone hydrogen-silsesquioxane (HSQ) resist (step I Figure 2-2 a). HSQ features a high patterning resolution below 10 nm, as well as a high post-processing stability due to its inert inorganic SiOx nature. After EBL patterning, a 50 nm-thick gold film is evaporated at low temperature (step II) to reduce the gold grain size by approximately a factor of two as compared to room temperature evaporation. Then flowable oxide (HSQ) is spun to planarize the overall structure (step III) and to allow for a subsequent etch back (step IV) that selectively removes the sacrificial top metal layer in order to clear out the aperture geometry. This process is uniformly carried out at a 100 mm wafer-scale and reliably results in the opening of all antennas at once after wet etching the HSQ (Step V). We point out that doing a conventional lift-off without this etch back step is ineffective to remove the top metal sacrificial layer due to hydrophobic interactions.

As becomes visible in the tilted SEM view of an opened "antenna-in-a-box" in Figure 2-2 b, the gold sidewalls yield a tapering angle due to metal diffusion during the evaporation. Therefore, the narrowest gap region, here ~12 nm, lies at the bottom of the antenna close to the substrate interface. Such a hotspot position is impractical for biological and fluorescence enhancement applications, where the narrowest gap position should be on the top surface of the antenna to maximize the contact with the sample (solution). We thus implemented a template stripping approach (step VI Figure 2-2 a),[152,153] whereby the gold structures are transferred, and flipped over, onto a microscope coverslip to facilitate access to the narrowest and brightest region of the nanogap. Figure 2-2 c, d show a comparison via SEM imaging before and after template stripping, the gap size apparent on the top surface seems slightly reduced after stripping, mostly due to charging during imaging. Additionally, only the narrowest gap region emerges on a flat top surface (Figure 2-2 e, f) enabling maximum fluorescence enhancement in a minimal near-field probe volume.

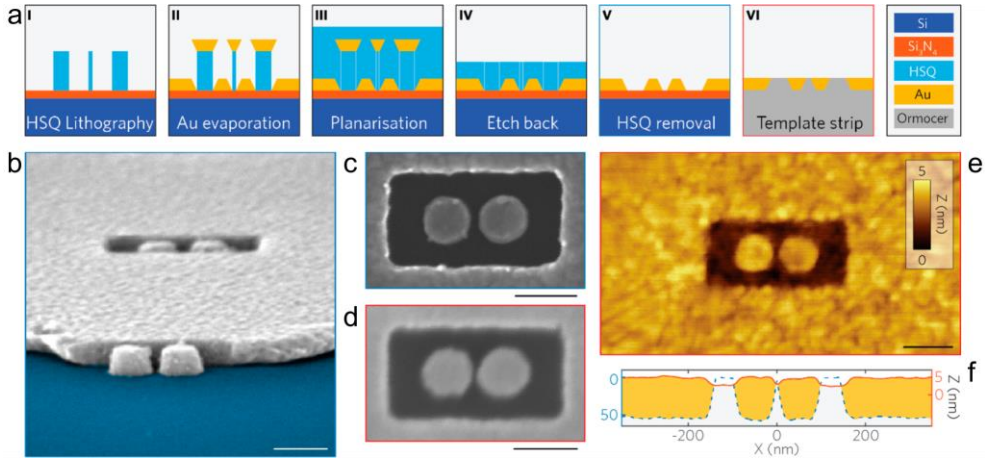

Figure 2-2. ***Fabrication and topography of planar nanogap antenna arrays.*** *(a) The antenna fabrication process flow is performed on a silicon nitride on silicon thin-film. The HSQ resist is patterned by electron-beam lithography (I) followed by gold evaporation (II), flowable oxide is spun for planarization (III) followed by etch back by Ar ion beam etching (IV), wet etching of the remaining HSQ (V) and final template stripping by UV curable adhesive (VI). (b) Tilted SEM view of an opened "antenna-in-box" before template stripping. The smallest part of the gap, here ~12 nm, lies at the surface level. A similar structure is imaged from the top before (c) and after (d) template striping. Dimensions are preserved and the space surrounding the antenna is filled by the UV curable polymer as seen in the AFM image (e) showing less than 5 nm residual topography. Panel (f) shows two AFM profiles averaged over 20 line-scans before (dashed blue) and after (red) template stripping of the 50 nm-thick gold structure. Scale bars are 100 nm.*

Our fabrication method is fully general, allowing for the design of arbitrary planar geometries. It is conveniently performed on conductive silicon substrates so that the final structures may be subsequently transferred to arbitrary substrates such as microscope coverslips, avoiding the need for a supplementary adhesion layer that can damp the plasmonic performance.[154] Additionally, the last template stripping step may be performed just before the final measurements, so the antenna hotspot is protected from surface contaminants during storage.

Transmission electron microscopy (TEM) was used to accurately quantify the dispersion in the antenna dimensions and to assess the reproducibility of the fabrication method. Figure 2-3 a shows TEM images of two representative "antenna-in-box" designs of 10 and 35 nm gap size, respectively.

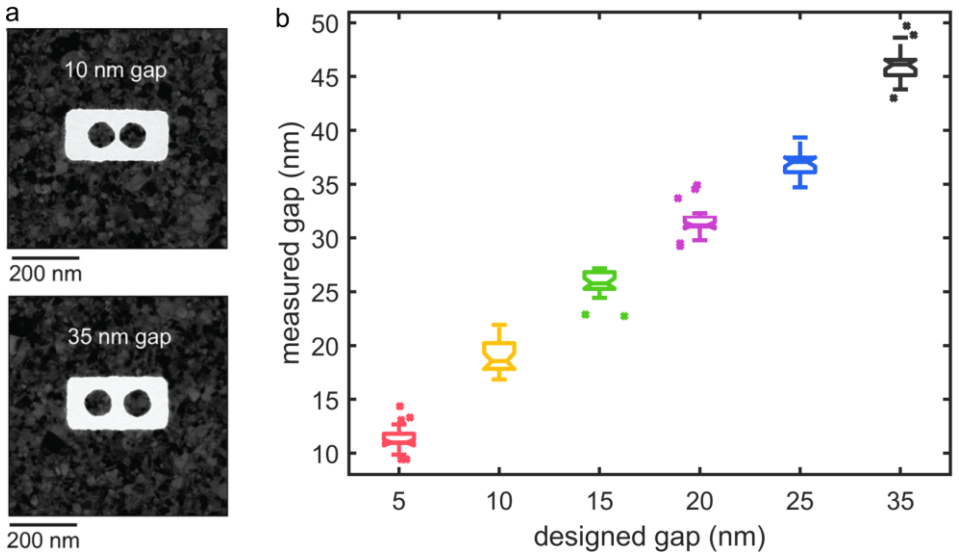

Figure 2-3. ***TEM metrology.*** *(a) TEM images of two examples of the gold "antenna-in-box" design of 10 and 35 nm gap size. (b) Measured gap width of the gold antenna dimer as a function of HSQ structure design width. Average gap width and associated standard deviation error bars are displayed for six sets of 25 antennas each.*

The same production process, excluding template stripping, was carried out on a 30 nm-thick freestanding silicon nitride membrane for accurate TEM metrology on prototypical arrays of nano-antennas. From the TEM measurements we obtain statistics on the actual gap size distribution versus the nominally designed one. The resulting gap size distribution confirms that we are able to fabricate gap sizes of 10-45 nm with narrow dispersions (Figure 2-3 b). Although HSQ is patterned at dimensions in the range of 5 nm for the nanogap region, the effective gap size of the gold dimer appears systematically larger. As already mentioned, this effect is due to a combination of metal diffusion and aperture clogging during evaporation, as well as metal wetting and diffusion onto the substrate. It should additionally be noted that the low feature density (antenna-to-antenna distance of 4 µm) results in negligible contribution from proximity effects in EBL, so that the lithographic resolution is equivalent on bulk and membrane substrates, as it is inherently limited by forward scattering in both cases.

To characterize the electromagnetic properties of the nano-antennas we applied scanning transmission electron energy-loss spectroscopy (STEM-EELS). The advantage of the STEM-EELS technique is that all eigenmodes of the nanostructure can be resolved, including the optically dark ones, which are not accessible for far-

field excitation, since there is no constraint by the selection rules for optical transitions. However, the EELS response of the "antenna-in-box" can be quite complex because of the influence of the rectangular aperture surrounding the dimer antenna. Therefore, we disentangle this complex response by first considering the simpler case of a single gold dimer without the surrounding metal layer, before inspecting the complete "antenna-in-box" configuration. We find the lowest energy mode at 1.78 eV to be the active bonding longitudinal mode which we exploit to optically drive the gap enhancement. The longitudinal bonding mode is visible at the same energy in both measured dark-field spectra (Figure 2-4 a, b).

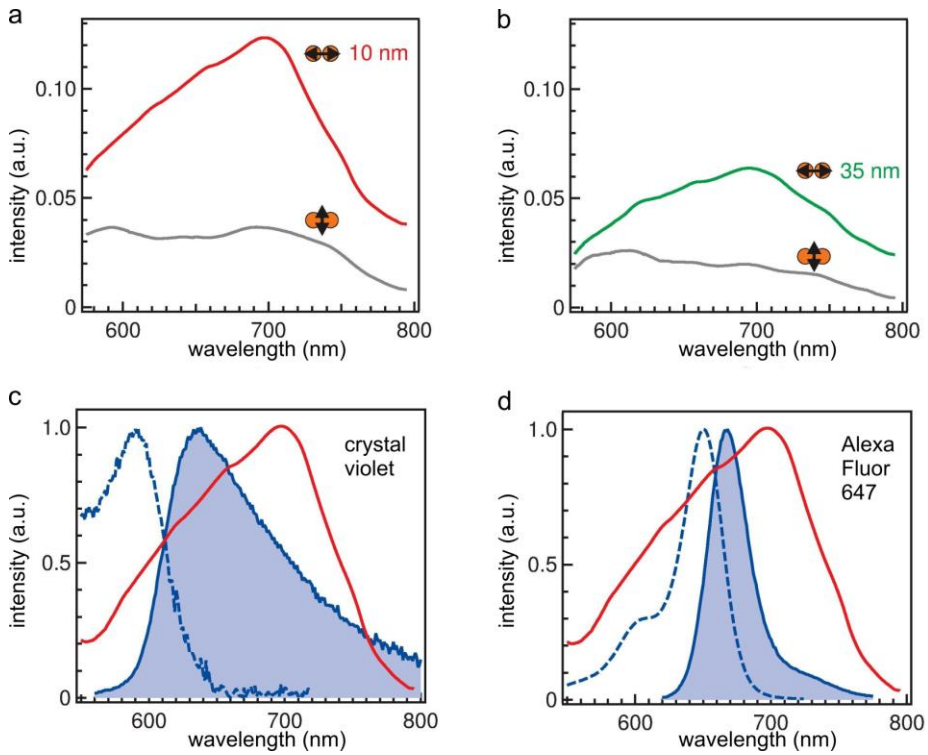

Figure 2-4. ***Overlap between the resonance of the nano-antenna and the fluorescence spectra.*** *(a, b) Dark-field scattering spectra for 10 nm (a) and 35 nm (b) gap sizes and two orientations of the illumination polarization. (c, d) Spectral overlap of the 10 nm antenna's response (red lines) with parallel orientation compared to the fluorescence spectra for Alexa Fluor 647 (c) and Crystal Violet (d). Excitation spectra are shown with dashed lines, emission spectra with solid shaded lines.*

We performed fluorescence experiments to assess the optical performance of the nano-antennas and to quantify the fluorescence enhancement together with the antenna's near-field volume. The experiments were performed by covering the

sample with a solution containing Alexa Fluor 647 or Crystal Violet fluorescent molecules at micromolar concentrations. The absorption and emission spectra of both dyes feature a strong overlap with the antenna's resonance (Figure 2-4 c, d). The fluorescence signal was analyzed with FCS and fluorescence burst analysis. FCS determines the average number of detected molecules from which we calculate the fluorescence brightness per emitter and the effective detection volume, as introduced in Section 2.2.1. In order to maximize the fluorescence enhancement brought by the nano-antenna, we use low quantum yield emitters: 200 mM of Methyl Viologen is added to the solution to quench the Alexa 647 quantum yield to 8%, and the quantum yield of Crystal Violet (CV) is around 2%.[109,114,115,118]

Figure 2-5 a, b display the raw fluorescence intensity time traces and corresponding correlation curves with excitation polarization parallel and perpendicular to the antenna dimer axis for two different gap sizes of 10 and 35 nm. Larger fluorescence fluctuations and higher correlation amplitudes are clearly observed when the incident electric field is parallel to the antenna axis and when the gap size is reduced. This directly evidences the presence of an electromagnetic hotspot in the antenna gap region. All experiments are performed at 26 µM concentration of Alexa Fluor 647, corresponding to 7630 molecules in the 0.5 fL confocal detection volume. The FCS correlation amplitude scales as the inverse of the number of fluorescent molecules, so in the confocal reference without the nano-antenna the FCS amplitude is very low at $1/7630 = 1.3\times10^{-4}$. In contrast, correlation amplitudes of 3.9 are detected with the nano-antenna of 10 nm gap size and correspond to an average number of 0.26 molecules diffusing through the hotspot at a time. The antenna detection volume can thus be quantified to 17 zL (1 zL = 10^{-21} L = 1000 nm^3) using the known 26 µM fluorophore concentration. This volume corresponds to a value 30 000× times smaller than the diffraction-limited confocal volume. The reduction of the detection volume is confirmed by the shortening of the diffusion time from 64 µs in the diffraction-limited confocal volume to 0.9 µs through the nanogap of the antenna.

For a molecule undergoing Brownian diffusion, the root mean square of the displacement scales as $(2\,D\,t\,)^{1/2}$, where D is the diffusion coefficient and t the elapsed time. Using this formula with D = 300 $\mu m^2/s$ for Alexa Fluor 647 at 21 °C[155] and t = 0.9 µs, we get a typical size of 23 nm, which corresponds to a 50 zL volume. While this number agrees well with the detection volume estimated from the FCS correlation amplitude, this approach cannot be used for an accurate measurement

of the effective detection volume due to the complex 3D form of the antenna hotspot volume and the presence of the interface influencing the Brownian diffusion.

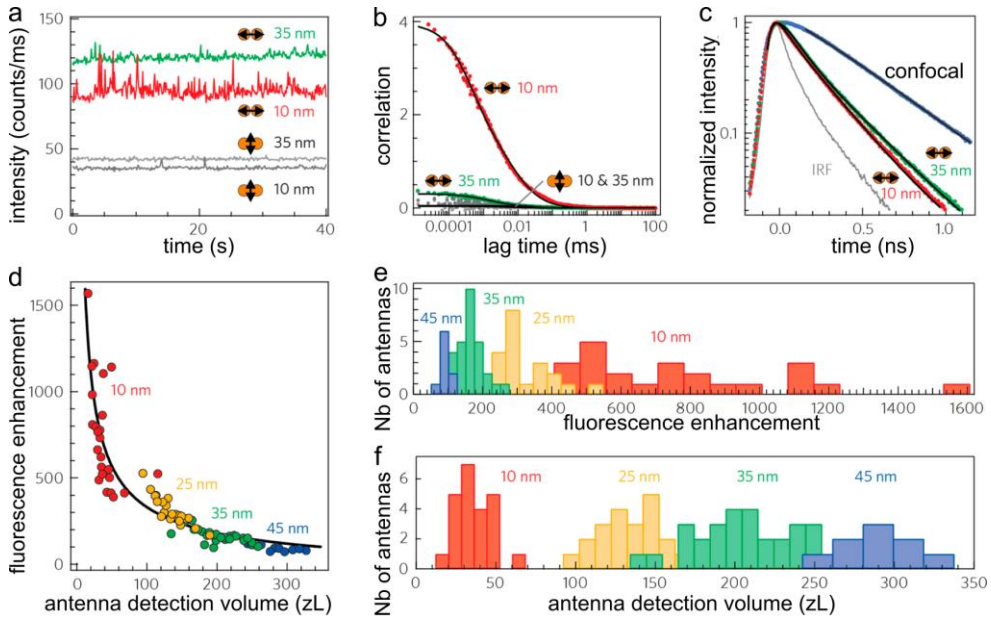

Figure 2-5. ***Nano-antennas enhance the fluorescence detection of Alexa Fluor 647 molecules in solution.*** *(a) Fluorescence time traces and (b) corresponding FCS correlation functions (dots, raw data; lines, numerical fits) for nano-antennas with 10 and 35 nm gap sizes with the excitation polarization set parallel or perpendicular to the antenna's main axis. The experimental conditions correspond to 26 µM of Alexa Fluor 647 with 200 mM of Methyl Viologen as chemical quencher under 2.3 kW/cm² excitation intensity at 633 nm wavelength. (c) Normalized time-resolved decay traces show Alexa Fluor 647 fluorescence lifetime reduction as the gap size is reduced. Black lines are numerical fits convoluted by the instrument response function (IRF). (d) Scatter plot of the fluorescence enhancement versus the nano-antenna's detection volume as deduced from FCS analysis on 83 different nano-antennas. The black line fit follows a power law dependence with a fixed -2/3 exponent. (e) Distribution of fluorescence enhancement factors deduced from the data in (d) for different gap sizes. (f) Distribution of the nano-antenna detection volume.*

From the same data set we normalize the fluorescence intensity by the number of detected molecules to measure the average fluorescence brightness per emitter. The number of detected molecules is simply the inverse of the correlation amplitude at zero lag time, and the fluorescence brightness per emitter can be computed by normalizing the average fluorescence intensity by this number of detected molecules. For the antenna with 10 nm gap size, we find a brightness of

370 counts/ms. This value is 1 600× higher than the 0.24 counts/ms found for the dye in the confocal reference setup, and clearly demonstrates the occurrence of large fluorescence enhancement in the nanogap. Simultaneously, the fluorescence lifetime is significantly reduced from 380 ± 15 ps in confocal illumination to 45 ± 10 ps in the 10 nm gap antenna (Figure 2-5 c).

Several additional test experiments confirm the near-field origin of the FCS signal. First, all the relevant observables, nanoscale volume confinement, fluorescence enhancement and lifetime reduction, disappear when the laser polarization is oriented perpendicular to the main antenna axis or when the gap size is increased. We have also performed control experiments on an antenna sample with an extra 8 nm thick silica layer deposited on top of the antennas to prevent the molecules from accessing the hotspot region. In that case, the FCS signal is lost confirming the crucial role of the few nanometer region surrounding the antenna gap. A study of the excitation power dependence validates that no saturation, photobleaching or triplet blinking affect our data. We also checked that the residual background luminescence from the gold antenna (in the absence of fluorescent molecules) remains negligible and shows no temporal correlation.

To assess the statistical reproducibility of the antenna fabrication, we repeated FCS experiments on a set of more than 80 different antennas and measured for each antenna its fluorescence enhancement and near-field detection volume. The scatter plot in Figure 2-5 d indicates a clear correlation between the fluorescence enhancement and the detection volume following an empirical power law with a −2/3 exponent. This exponent value can be understood because the volume scales as the cube power of the typical near-field size, while the fluorescence enhancement is dominated by the gain in local excitation intensity which scales as the square power of the typical near-field size. For each value of the desired nominal gap size, the histograms of the fluorescence enhancement and detection volume illustrate the statistical dispersion of the data around the average (Figure 2-5 e, f). This dispersion comes as a natural consequence of the variability of the gap sizes as characterized by TEM in Figure 2-3, especially for the smallest gaps where a nanometer variation in the gap size can have a large influence on the antenna's performance and the measured enhancement factors.

Importantly, the performance of these novel plasmonic nano-antennas significantly outperforms the values achieved previously using focused ion beam lithography,[118] which obtained at best a 60 zL detection volume and 1 100× fluorescence

enhancement for an 11 nm gap size and identical experimental configuration. This demonstrates the advantage of back etching combined with template stripping to achieve ultra-confined detection volumes of only a few zeptoliters and giant fluorescence enhancement factors.

Emitters with low quantum yields access to higher fluorescence enhancement factors, as the nano-antenna provides a larger benefit to increase the emission quantum yield[99,101] as explained in Section 2.2.2. To probe this effect, we perform experiments on Crystal Violet (CV) molecules, which have a 2% quantum yield.[102,103] The CV solution was set to a concentration of 1 µM in a water-glycerol 1:1 solution to slow down the diffusion of molecules crossing the antenna hotspot, allowing for direct analysis of the fluorescence bursts for individual molecules. Using the detection volume estimated previously with FCS, the 1 µM concentration ensures that, on average, less than 0.02 CV molecules are present in the 10 nm gap region. This low number rules out the possibility that the estimated count rates per burst originate from more than one single molecule diffusing in the nanogap. Intense fluorescence bursts are clearly detected on the fluorescence time traces (Figure 2-6 a-c), with their amplitude decreasing as the gap size is enlarged. This feature confirms that the fluorescence bursts stem from the antenna gap region. To measure the fluorescence enhancement, we fit the photon count histograms in Figure 2-6 d-f with exponentially decaying probability distributions and record the maximum peak amplitude in the fitted distribution. The reference peak fluorescence count per CV molecule is estimated at 0.18 counts/ms at the same 2.30 kW/cm^2 excitation power, in agreement with values reported independently in Refs 102,103. For the smallest 10 nm gap size, the maximum count is 2 750 counts/ms with a background of 100 counts/ms (set by the fluorescence from the CV molecules diffusing away from the hotspot region and the residual photoluminescence from the metal). This leads to an impressive fluorescence enhancement of 15 000 times.

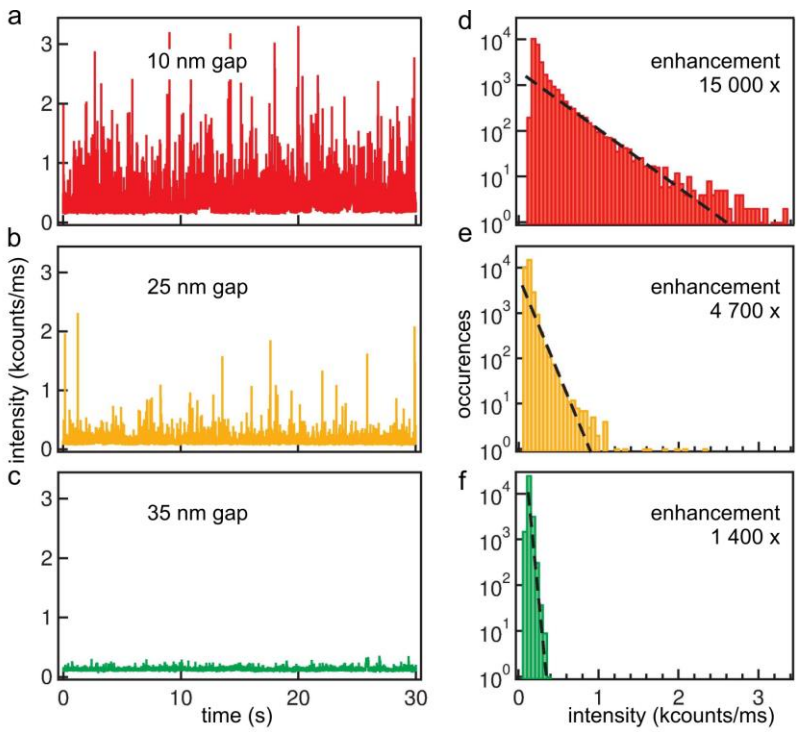

Figure 2-6. ***Fluorescence enhancement on Crystal Violet molecules measured with fluorescence bursts analysis.*** *(a-c) Fluorescence time traces recorded on nano-antennas with increasing gap sizes using 1 µM of Crystal Violet in water-glycerol (1:1) solution with 2.3 kW/cm² excitation intensity at 633 nm. The binning time is 1 ms. (d-f) Photon count rate histograms deduced from the traces in (a-c). The dashed lines are fits by exponentially decaying probability distributions.*

The same procedure performed on Alexa Fluor 647 with 200 mM Methyl Viologen (8% quantum yield) indicates a fluorescence enhancement of 5 300× for a 10 nm gap size (Figure 2-7). The relative change in the enhancement factors results from the differences of the quantum yields between CV and Alexa 647 measurements, which is in line with our initial expectations and our measurements. Note that the enhancement factor for Alexa 647 estimated from the burst peak intensity is about 3× higher than the one measured with FCS (Figure 2-5 d), as the burst analysis favors the best event when the emitter's position and orientation lead to the highest fluorescence intensity.

The measured fluorescence enhancement factors come very close to the values predicted theoretically by merging **Eq. 2-17** and **Eq. 2-18**, as introduced in Section 2.2.2:

$$\eta_F = \frac{I^*_{exc}}{I_{exc}} \frac{\Gamma^*_{rad}}{\Gamma_{rad}} \frac{1}{1 - \phi_0 + \frac{\phi_0(\Gamma^*_{rad} + \Gamma^*_{loss})}{\Gamma_{rad}}} \qquad \textbf{Eq. 2-21}$$

This equation states that the fluorescence enhancement η_F is the product of the excitation intensity enhancement in the nanogap I^*_{exc}/I_{exc} times the enhancement of the radiative decay rates $\Gamma^*_{rad}/\Gamma_{rad}$ and a third term which depends on the initial quantum yield ϕ_0 of the fluorescent molecule and an additional decay rate Γ^*_{loss} describing the non-radiative energy transfer to the antenna's material induced by ohmic losses.

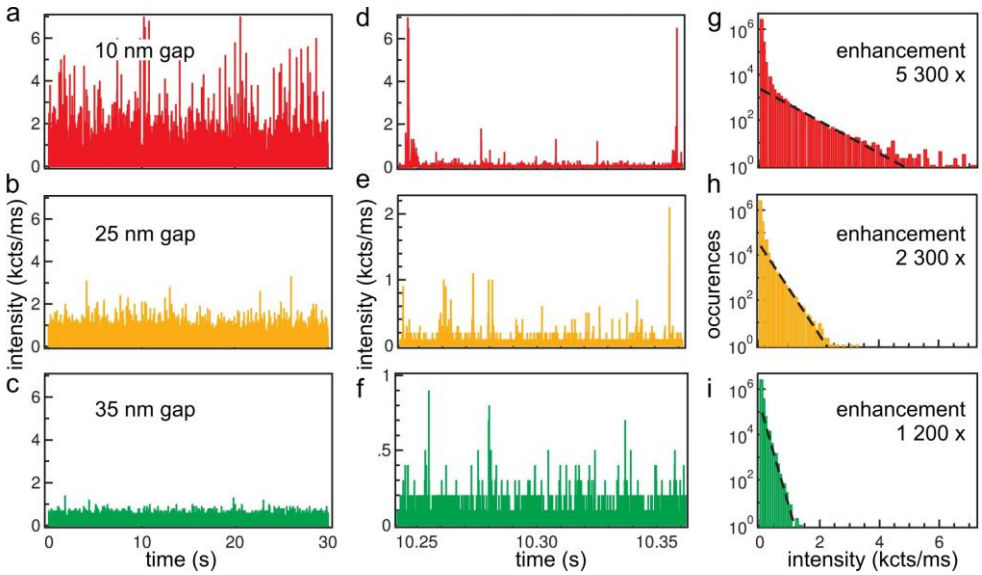

Figure 2-7. ***Fluorescence bursts analysis on Alexa Fluor 647 molecules.*** *Fluorescence bursts analysis to determine the enhancement factors for Alexa Fluor 647 molecules with 200 mM Methyl Viologen. (a-c) Fluorescence time traces recorded on nano-antennas with increasing gap sizes using 1 µM Alexa Fluor 647 in water-glycerol (1:1) solution with 2.3 kW/cm² excitation intensity at 633 nm. The binning time is 10 µs. (d-f) Enlarged temporal windows showing discrete bursts that correspond to individual molecules crossing the antenna detection volume. (g-i) Photon count rate histograms deduced from the traces in (a-c). The dashed lines are fits by exponentially decaying probability distributions. A reference of 0.85 counts/ms for Alexa Fluor 647 (with 200 mM Methyl Viologen as chemical quencher) is used to compute the fluorescence enhancement factors.*

In our case we neglect the collection efficiency improvement brought by the antenna (backfocal plane imaging confirms this assumption[118,156]). For the smallest 10 nm gap and a dipole emitter located in the gap center, the FDTD simulations estimate the different contributions to be $I^*_{exc}/I_{exc} = 600$, $\Gamma^*_{rad}/\Gamma_{rad} = 700$ and $\Gamma^*_{rad} + \Gamma^*_{loss}/\Gamma_{rad} = 1\,100$. These values predict fluorescence enhancement factors of 18 000× for Crystal Violet and 4 700× for Alexa 647, which are in excellent agreement with our experimental data.

2.4 Conclusion

In this chapter we have described the combination of EBL followed by post-processing and template stripping as a powerful and versatile method to fabricate nano-antennas with direct accessibility of the hotspot region, large-scale availability, and gap sizes as small as 10 nm with sharp edges. This design provides fluorescence enhancement factors up to 15 000×, together with nanoscale detection volumes in the range of 10 zL allowing for single-molecule sensitivity at µM concentrations over gap sizes between 10-45 nm. In the next chapters we will showcase the capabilities of our innovative planar plasmonic nanogap antenna platform to resolve the spatiotemporal organization of lipids and proteins on biological membranes at the nanoscale.

3 Planar nano-antennas to resolve transient nanoscopic heterogeneities in multicomponent mimetic membranes[3]

Nanoscale membrane assemblies of sphingolipids, cholesterol and certain proteins, also known as lipid rafts, play a crucial role in facilitating a broad range of important cell functions. Whereas on living cell membranes lipid rafts have been postulated to have nanoscopic dimensions and be highly transient, the existence of a similar type of dynamic nanodomain organization in multicomponent lipid bilayers has been questioned.

In this chapter, we exploit planar plasmonic antenna arrays as introduced in Chapter 2 to assess the dynamic nanoscale organization of mimetic lipid membranes. Our approach takes advantage of the highly enhanced and confined excitation light provided by the nano-antennas together with their outstanding planarity to investigate membrane regions as small as 10 nm in size with microsecond time resolution. By combining fluorescence correlation spectroscopy (FCS) with nano-antennas of different gap sizes, we generate FCS diffusion laws that reveal transient nanoscale heterogeneities on ternary lipid mixtures containing cholesterol. Our diffusion data are consistent with the coexistence of transient nanoscopic domains in both the

[3] The content of this chapter has been published in:

Winkler, P.M., Regmi, R., Flauraud, V., Brugger, J., Rigneault, H., Wenger, J. and García-Parajo, M.F., *Transient nanoscopic phase separation in biological lipid membranes resolved by planar plasmonic antennas.* ACS Nano, 2017 11(7), pp.7241-7250.

liquid-ordered and the liquid-disordered microscopic phases of multicomponent lipid bilayers. Thus, although microscale phase separation occurs on mimetic membranes, nanoscopic domains also coexist, suggesting that these transient assemblies might be similar to those occurring in living cells which in the absence of raft-stabilizing proteins are poised to be short-lived.

3.1 Introduction

The spatiotemporal lateral organization and the biological function of the eukaryotic plasma membrane are intricately interlaced at the nanoscale. It is well accepted that the landscape of the cell membrane is highly heterogeneous and shaped by a variety of lipids and proteins that differ in their physicochemical properties. In the plane of the membrane, lateral heterogeneities resulting from the formation of specialized regions enriched in sphingolipids, cholesterol and specific proteins are commonly known as lipid rafts.[1,2,6,7] These lipid assemblies are thought to constitute a tightly packed, short-range, liquid-ordered (Lo) phase coexisting with a more liquid-disordered (Ld) phase within the surrounding fluid membrane.[9,13,29,157] While the existence of phase separation in the plasma membrane has been debated for many years, a large amount of recent experimental data is convincingly demonstrating that lipid rafts in living cell membranes have nanoscopic dimensions and are highly dynamic.[13,45,62–64,158] Importantly, lipid rafts play a crucial role in many cellular processes that include signal transduction, protein and lipid sorting and immune response amongst others.[1,19,45,157,159] Understanding the formation mechanism and properties (e.g. size, composition) of lipid rafts and relating their structure to their functional role is of paramount interest.

Model lipid membranes represent a simple mimetic system that recapitulates some of the most important features of biological membranes, i.e., spatiotemporal compartmentalization and lipid phase separation. On the microscopic scale, ternary lipid membranes composed of unsaturated phospholipids, saturated sphingolipids and cholesterol separate into coexisting Ld and Lo phases, which can be resolved by diffraction-limited optics.[21,22,24] The large microscopic size and the stable nature of Lo domains observed on mimetic membranes strongly contrasts with the highly transient and nanoscopic size of lipid rafts inferred on living cells. Interestingly, recent works suggest that the microscopically homogeneous Lo and Ld phases on lipid model membranes might in fact also be heterogeneously organized at the nanometer scale.[9,76,160]

The possibility that nanoscale lipid heterogeneities also exist within the supposedly homogenous Lo and Ld phases of synthetic mimetic membranes is intriguing and of particular interest as they might be the underlying basis for lipid raft formation in living cells. Indeed, earlier work from Hancock and co-workers predicted that in

the absence of stabilizing proteins, the size of lipid nanoassemblies would be smaller than 10 nm in diameter and short-lived, with lifetimes below 1 ms.[9,161] Consistent with this hypothesis, deuterium-based nuclear magnetic resonance (d-NMR) experiments revealed the presence of cholesterol and sphingolipids in the Ld phase as well as of unsaturated lipids in the Lo phase, suggesting that nano-sized clusters may exist in both phases.[160] Stimulated emission depletion (STED) nanoscopy combined with FCS (STED-FCS) has been applied to study the nanoscale dynamics occurring in Lo and Ld phases of ternary lipid-cholesterol mixtures with a spatial resolution of 40 nm.[65] The results showed fully homogenous Lo and Ld phases with no evidence of nanoscopic domains at the tested spatial scales (40-250 nm). By using a similar approach, Sarangi et al. reported on the appearance of dynamic nanoscopic heterogeneities in two-component model lipid membranes at the length scale of 80-150 nm, close to their instrumental spatial resolution (~ 80 nm).[69] However, the authors suspected the existence of even smaller domains that might remain unresolved and suggested that higher resolution (e.g. gated STED-FCS providing ~30 nm resolution) might uncover their existence in binary as well as in ternary mixtures of model lipid membranes.

Moreover, high-speed single particle tracking (SPT) of 20 nm gold beads attached to individual lipids showed anomalous diffusion on the Lo phase consistent with the occurrence of nanoscale heterogeneities, while homogeneous lipid diffusion was observed on the Ld phase.[76] The estimated sizes of the nanodomains on the Lo phase varied between 20 to 40 nm with lipid trapping times inside the domains below 1 ms.

A different and potentially powerful approach to investigate dynamic nanoscale heterogeneities of lipid bilayers is provided by the use of plasmonic antennas. As introduced in Chapter 1, these metal nanostructures enhance and confine light down to nanoscale dimensions, sustaining localized hotspot regions of the excitation light.[95,117,162,163] In addition, when combined with FCS, single-molecule detection at ultra-high sample concentrations with microsecond time resolution can be obtained, both in solution and living cell membranes.[79,101,104,118,120] However, in most antenna designs the region of maximum field localization and enhancement (i.e., hotspot) is buried into the nanostructure, and thus difficult to access. As demonstrated in Chapter 2, we overcame this drawback by fabricating planar dimer antenna arrays where the gap region is located at the sample surface.[119] This design provides direct accessibility to the antenna hotspot region and drastically

improves the optical performance to yield fluorescence enhancement factors of up to 10^4–10^5 together with nanoscale detection volumes in the zeptoliter range. Moreover, we showed in Chapter 2 that this type of antennas is quite flat, facilitating studies on biological membranes without introducing membrane curvature artifacts as a result of topographic differences on the antenna substrates.

In this chapter, we describe the application of this type of planar antenna arrays to inquire into the nanoscale dynamics of multicomponent lipid bilayers. Our results show the coexistence of transient nanoscopic domains in both the Lo and Ld phases, in the microsecond time regime and with characteristic sizes below 10 nm. These nanoscale assemblies might be reminiscent to those naturally occurring in living cells, which in the absence of raft-stabilizing proteins are expected to be highly transient.

3.2 Methods

3.2.1 Lipids

1,2-dioleoyl-*sn*-glycero-3-phosphocholine (DOPC) and N-stearoyl-D-*erythro*-sphingosyl-phosphorylcholine 18:0 (SM) were purchased from Avanti (*Avanti Polar Lipids, Inc.*). Cholesterol (Chol) ≥99% was purchased from *Sigma-Aldrich* and the fluorescent dye $DiIC_{18}(5)$ solid (DiD) from *Molecular Probes, Life Technologies Corporation*.

3.2.2 Preparation of lipid model membranes and substrate support

For the preparation of glass-supported lipid bilayers, glass coverslips were extensively cleaned with acetone, ethanol, ultrasonic bath and in a UV/ozone cleaner with intermediate rinsing steps with pure MilliQ water and immediately used afterwards. Lipid mixtures of DOPC, DOPC:SM (1:1) and DOPC:SM:Chol (10/20 mol%) dissolved at 1 mg/mL in chloroform:methanol (9:1) together with 0.01 mol% of the fluorescent dye DiD were mixed in small glass bottles on ice at 4 °C and immediately deposited on the cleaned coverslips or antenna substrates. The gold antenna substrates were carefully cleaned with acetone, ethanol and MilliQ water followed by a short UV/ozone plasma exposure (between 2-5 min) immediately prior to lipid bilayer deposition. The latter treatment removes any residual organic layer from the gold substrate, guaranteeing a chemically inert and hydrophilic surface.[164] All the steps were carried out under a fume hood. The

different lipid mixtures were allowed to dry for roughly an hour in the presence of a weak nitrogen flow, and then kept in vacuum for an additional hour. Consequently, the samples were hydrated in PBS (pH 7.4) and carefully rinsed to remove excess lipids. Samples were imaged and probed by FCS immediately after preparation. All measurements were performed at room temperature.

3.2.3 Fabrication of planar nano-antenna arrays with different gap sizes

Planar gold dimer antenna arrays with gaps of different sizes were fabricated onto glass-coverslips at the EPFL, in the group led by Prof. J. Brugger within a European collaboration following a procedure described in more detail in Chapter 2.

In brief, the antenna fabrication process was performed on a thin silicon nitride layer deposited on silicon substrates that provided suitable electrical conductivity and chemical stability for the subsequent process steps. Hydrogen-silsesquioxane (HSQ) resist was first spun and then patterned using electron-beam lithography on top of the substrate. A thin layer of gold (50 nm thick) was deposited by electron beam evaporation over the patterned HSQ structures followed by a planarization step by flowable oxide spin coating. After etching back by Ar-based ion beam etching and removal of the remaining HSQ, the final antenna dimers were stripped from the substrates using a UV curable polymer. This step provided flipped over antennas with accessible gap regions onto optically transparent microscope coverslips. Prior to lipid bilayer deposition, the antenna substrates were carefully cleaned with ethanol, MilliQ water rinsing and UV light exposure for 1 minute followed by 3 minutes of ozone treatment.

3.2.4 Fluorescence Microscopy and FCS

Experiments have been performed on a commercial *MicroTime 200* setup built around an inverted Olympus microscope and using a 60×, 1.2 NA water-immersion objective (*Olympus UPLSAPO*). The sample was positioned with a three-axis piezoelectric stage (*Physik Instrumente, Germany*) allowing us to scan the sample and precisely position the focus on individual nano-antennas. Excitation was provided by a picosecond laser diode (*PicoQuant LDH-D-C-640*) with a linearly polarized beam operating at 640 nm in continuous wave mode. A half-wave plate was used to control the polarization of the incoming light. The fluorescence signal was collected back through the same objective, separated from the laser light by a

dichroic mirror, split by a 50/50 beam splitter cube and sent onto two avalanche photodiodes (APDs) (*PicoQuant MPD- 50CT*) after passing through a 30 µm pinhole conjugated to the focus plane guaranteeing a 0.5 fL detection volume. An emission filter and a 650–690 nm bandpass filter just before each detector were used to suppress the scattered light by the excitation laser and to maximize the fluorescence signal collection. We used two APDs to perform cross-correlation between the two channels instead of the autocorrelation of one channel, since it reduces artifacts due to the dead time of each detector after-pulses. FCS measurements were performed by illuminating the sample at an excitation power density of ~2 kW/cm^2.

The fluorescence intensity time traces were recorded with a TCSPC module in the *PicoQuant* time-tagged time-resolved mode and were correlated by the commercial software package *SymPhoTime 64 (PicoQuant)* afterwards.

Note that the *SymPhoTime 64* software package was used for the overall handling of the experiment, detection of fluorescent counts, computation of the autocorrelation curves $\boldsymbol{G(\tau)}$ and fitting routines for the FCS analysis.

The setup was calibrated by measuring the known three-dimensional diffusion coefficient of Alexa Fluor 647 in solution. Fluorescence time traces on individual nano-antennas were recorded for either 30 or 60 seconds with a temporal resolution of 4 ps. Autocorrelation function (ACF) curves were generated over time windows of at least 10 s in length.

The calculated correlation curves $\boldsymbol{G(\tau)}$ were fitted using a two-dimensional Brownian diffusion model, assuming a Gaussian beam profile as introduced in Section 2.2.1 in **Eq. 2-16** but without a triplet contribution, thus yielding **Eq. 3-1**:

$$\boldsymbol{G(\tau) = A_1 \frac{1}{1 + (\tau/\tau_{D,1})} + (1 - A_1) \frac{1}{1 + (\tau/\tau_{D,2})}} \qquad \textbf{Eq. 3-1}$$

where $\boldsymbol{A_1}$ and $\boldsymbol{\tau_{D,1}}$ are the amplitude and diffusion time of the contribution of the first diffusing species and $\boldsymbol{1 - A_1}$ and $\boldsymbol{\tau_{D,2}}$ are of the second one. We used a two-component fitting since the excitation of the dimer antenna inside the nano-aperture leads to two distinct diffusion times as explained in Section 2.2.1. The

shortest diffusion time corresponds to direct excitation at the antenna gap while the second component corresponds to the diffusion times of molecules inside the nano-aperture but away from the antenna hotspot region. These molecules contribute weakly to the overall correlation curve since they are only excited by the residual light inside the nano-aperture. We also attempted to fit the curves using a three-component fitting, but in general the amplitude weight of the third component was either very small (below 3%) and/or rendered a fitting error.

3.3 Results

3.3.1 Experimental approach and determination of the illumination areas of the different nano-antenna gaps

Model lipid bilayers with different compositions were prepared on glass coverslips or on top of antenna substrates following a modified protocol from Ref. 165 and explained in the Methods Section 3.2.2. Bilayers were composed of the unsaturated phospholipid DOPC alone, DOPC in combination with sphingomyelin (18:0 SM, 1:1 molar proportions) and of ternary mixtures of DOPC, SM (1:1) with addition of 10 or 20 mol% cholesterol (Chol). The different bilayers were labeled with the lipophilic fluorescent dye DiD which preferentially partitions in the Ld phase.[23,166] We first characterized the quality of the glass-supported bilayers by means of FCS using a diffraction-limited confocal microscope. The results are shown in Figure 3-1 for different lipid mixtures and upon addition of cholesterol. The obtained diffusion values are summarized in Table 3-1 and are in good quantitative agreement with values reported for similar lipid mixtures.[23]

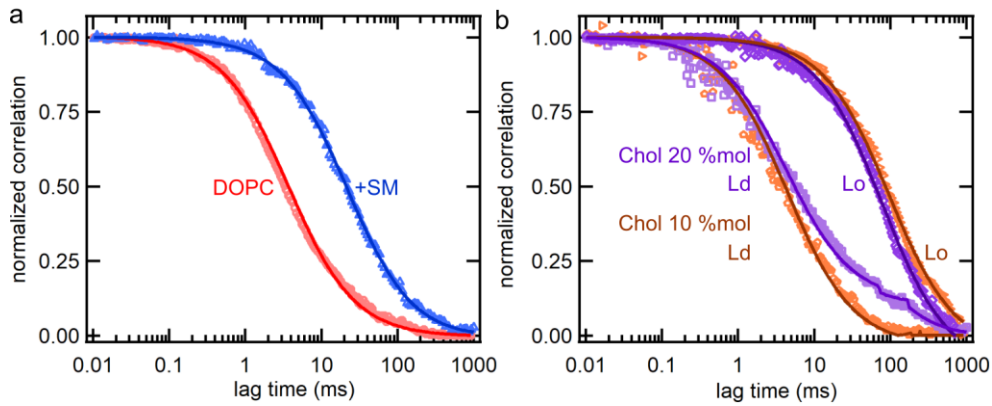

Figure 3-1. ***Experimental quality assessment of the four different model lipid bilayers by confocal excitation.*** *(a) Normalized autocorrelation functions (ACFs) on pure DOPC and DOPC:SM (1:1) bilayers. (b) Same as (a) but for ternary mixtures of DOPC:SM with the addition of 10 and 20 mol% Chol. Upon addition of cholesterol microscopic phase separation into Ld and Lo phases occurs and hence two respective ACFs are shown in (b).*

Table 3-1. *Diffusion coefficients of DiD for the different lipid model membrane mixtures as obtained from confocal measurements.*

Lipid mixture	**DOPC**	**DOPC: SM (1:1)**	**DOPC:SM (1:1) + 10%Chol**		**DOPC:SM (1:1) + 20%Chol**	
Diffusion coefficient ($\mu m^2/s$)	**5.8±0.3**	**1.7± 0.4**	**2.3±0.3 (Ld)**	**0.19±0.06 (Lo)**	**2.9±0.4 (Ld)**	**0.27±0.05 (Lo)**

To investigate the existence of nanoscale heterogeneities in the different lipid mixtures, we then used the same preparation protocol to prepare lipid bilayers on top of the planar antenna platform as schematically illustrated in Figure 3-2. The antenna design consists of gold dimers of 80 nm in diameter separated by nanogaps of different sizes (from 10 nm to 45 nm) and surrounded by nano-apertures to further constrain the excitation area and reduce background contribution from fluorescent molecules diffusing outside the antenna hotspots. For more details please refer to the results reported in Chapter 2.

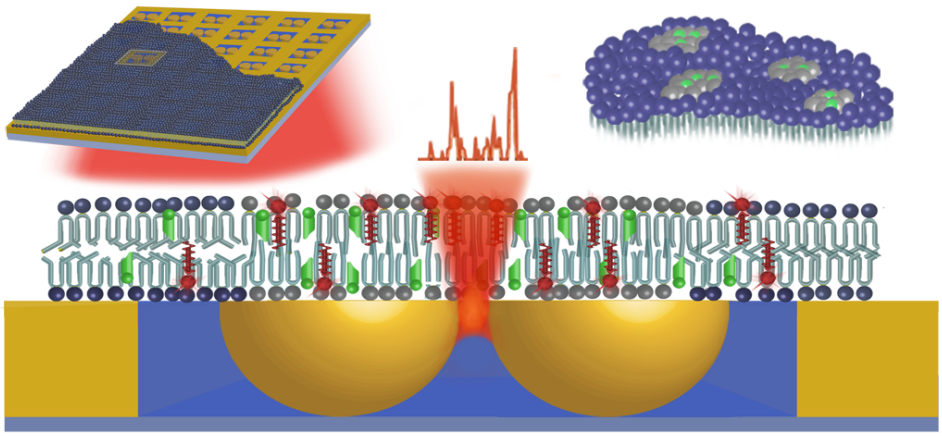

Figure 3-2. ***Biological lipid membranes probed by planar gold nano-antenna arrays.*** *The schematics of our experimental approach is shown. Bilayers of different lipid compositions are deposited on top of the planar nano-antenna arrays. Each antenna consists of a gold dimer separated by a nanogap and embedded in a nano-aperture. The lipids DOPC and SM are depicted in grey with their respective different shape of the tails. Cholesterol is shown in green and the fluorescent dye DiD in red. Individual antennas are excited using a confocal setup. The confined and enhanced field at the antenna hotspot excites individual DiD molecules embedded in the bilayer. Fluorescence fluctuations arising from the passage of molecules through the hotpot of the antenna are recorded and autocorrelated in time to generate ACF curves.*

To estimate the illumination areas from our antenna gaps, we considered for the x-direction the mean values of the three gap sizes as directly measured from TEM images (refer to Figure 2-3 in Chapter 2), while for the y-direction, we took the distances corresponding to the full-width-at-half-maximum (FWHM) of the respective antenna excitation intensity profiles, as obtained from FDTD simulations (Figure 3-3). The calculated gap areas are (200 ± 50) nm^2, (1080 ± 80) nm^2 and (2025 ± 110) nm^2 for the nominal 10 nm, 30 nm and 45 nm gap sizes, respectively.

The sizes of the illumination areas were further calibrated by measuring the diffusion times of the Alexa Fluor 647 dye in solution for five different antenna sizes (10, 25, 30, 35 and 45 nm) considering the reported diffusion coefficient of the dye (300 $\mu m^2/s$).[155] Results of the calibration are shown in the Figure 3-4. From the calibration curves, we experimentally determined values of (300 ± 50) nm^2, (1080 ± 80) nm^2 and (2025 ± 110) nm^2 for the 10, 30 and 45 nm gap antennas respectively. The sizes of the illumination areas are between one to two orders of

magnitude smaller than the ones of confocal excitation, underscoring the extreme light confinement afforded by plasmonic antennas.

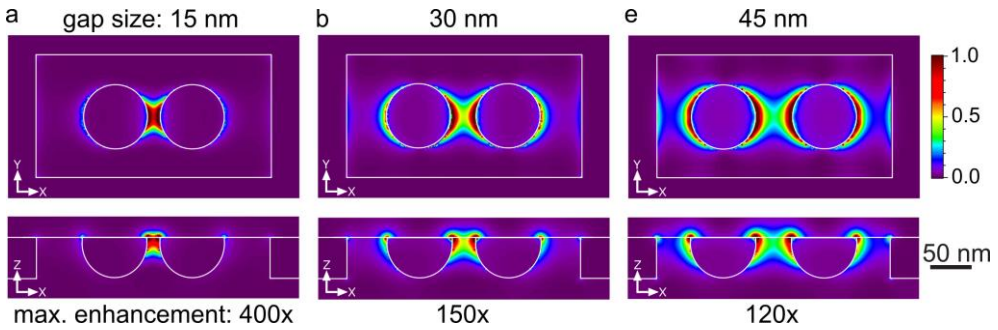

Figure 3-3. ***FDTD simulations of planar nanogap antennas.*** *(a-c) The normalized excitation intensity enhancement at 633 nm is computed using the finite-difference time-domain method (FDTD) for a gold nano-antenna (diameter 80 nm) in a nano-aperture for different gap sizes (15, 30 and 45) nm, approximately matching the three antenna gap areas used in the experiments. Computations are performed using the FDTD method (RSoft Fullwave software). The mesh size is 0.5 nm for (a), 1 nm for (b) and 1 nm for (c). We used 214 temporal steps of 8.1 10^{-19} s. The permittivity of gold is modeled according to the data in Ref. 167. The intensity is recorded at the antenna surface for the cuts in the plane (y-x) and along the planes crossing the antenna's center in case of the z-x cuts.*

The FCS experiments on the model lipid membranes on top of nano-antennas were conducted using a commercial confocal setup, as explained in the Methods Section. In brief, the samples were excited by focusing the incoming laser light (λ = 640 nm, laser power density ~2 kW/cm^2) onto individual antennas using a water-immersion objective (NA =1.2). Under these excitation conditions, the temperature increase at the antenna hotspots due to optical heating was estimated to be only within 1-3 K.[168]

The fluorescence signal was collected in reflection mode by the same objective, filtered from the excitation light and sent to two single photon-counting APD detectors. As the antennas show a polarization-dependent response, we used excitation polarization parallel to the antenna gaps to achieve maximum field enhancement and confinement.[119] Fluorescence fluctuations arising from the diffusion of DiD in the bilayers were recorded for at least 30 seconds at each individual antenna and the resulting normalized ACFs were calculated.

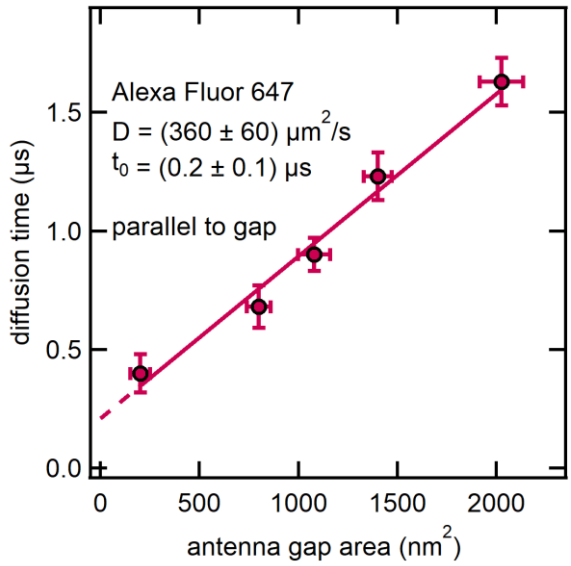

Figure 3-4. ***FCS diffusion plot for the free dye Alexa Fluor 647 to calibrate the antenna gap areas.*** *The average diffusion times vs. antenna gap areas are shown resulting from measurements on 83 different nano-antennas to probe the free diffusion of Alexa Fluor 647 molecules in solution at a concentration of 26 μM and chemically quenched with 200 mM Methyl Viologen to allow the maximum fluorescence enhancement possible.*

3.3.2 FCS measurements in pure DOPC bilayers using nano-antennas of different gap sizes

Representative fluorescent intensity time traces of DiD diffusion in a pure DOPC membrane over three different antenna gap areas are shown in Figure 3-5 a together with enlarged views of representative single bursts. The burst duration increases with gap area, confirming that the detected signal arises from the excitation of the dye at the gap regions. This is further substantiated by the normalized ACFs obtained for different gap sizes and compared to confocal measurements (Figure 3-5 b). To extract the diffusion times from individual ACF curves, we performed two-component 2D Brownian fittings to account for both direct excitation from the gap region (≥ 55-90% of the weighted amplitude) and residual excitation of DiD diffusing through the nano-aperture consisting of the sum of two terms (refer to **Eq. 3-1** in Methods Section 3.2.4). Results of the main component of the fitted curves shown in Figure 3-5 b render τ_{DOPC} values of (6 ± 1) μs, (25 ± 3) μs and (71 ± 25) μs for the respective gap areas of (300, 1080, and 2025)

nm² compared to τ_{DOPC}=3.5 ms for confocal excitation. The complete results of the fittings and relative contributions of the gap and nano-aperture excitation are shown in Table 3-2.

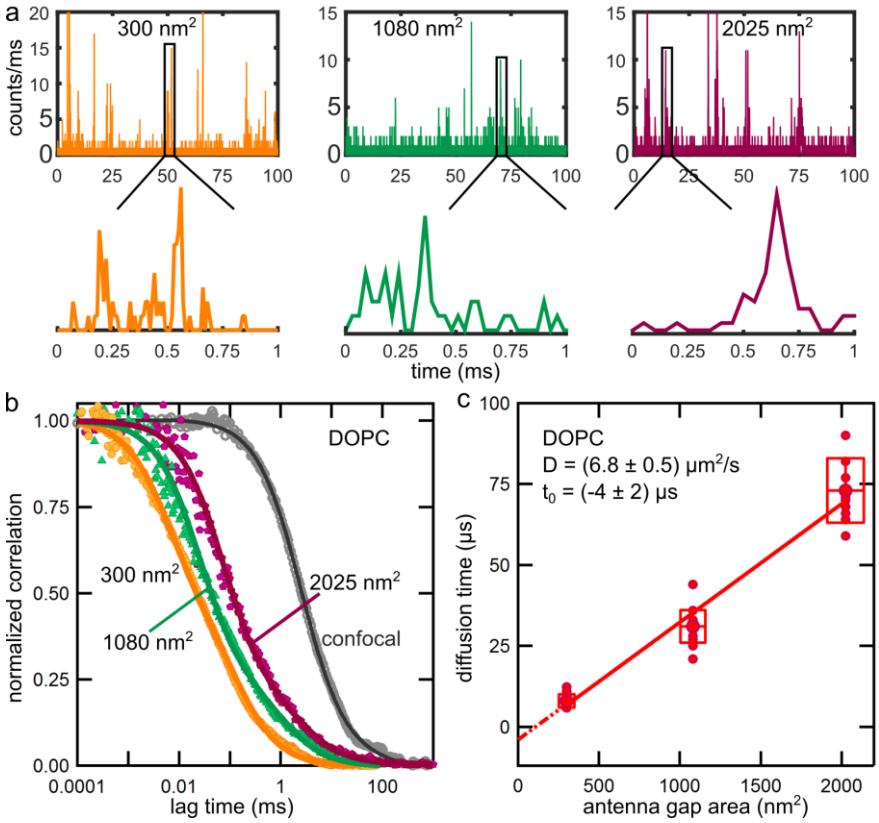

Figure 3-5. ***FCS measurements in pure DOPC bilayers using planar plasmonic antenna arrays of different gap sizes.*** *(a) Representative fluorescence intensity time traces of DiD embedded in a pure DOPC bilayer for three different antenna gap areas together with enlarged views of representative bursts. (b) Normalized ACF curves as obtained from different antenna gap areas and by confocal excitation. (c) Diffusion times as extracted from the ACF fitting as a function of the antenna gap area. Each dot corresponds to an individual ACF measurement in a single antenna. Number of measurements: 13, 8 and 12 for antenna gap areas of 300 nm², 1080 nm² and 2025 nm² respectively on five different samples. Fitting by orthogonal distance regression (red line) has been performed through the mean diffusion time values of each respective antenna gap area minimizing the error for the gap area and ± std in diffusion time (horizontal and vertical line of the red box, respectively).*

Diffusion times obtained from multiple measurements on individual antennas as a function of the probed gap are shown Figure 3-5 c. To obtain the FCS diffusion law plot (as introduced in Chapter 1) extended to the nanoscale for DOPC, the mean values of the diffusion times versus gap area could be well-fitted to a straight line according to

$$\boldsymbol{\tau(\omega^2) = \tau_0 + \omega^2/(4 \times D)} \quad \textbf{Eq. 3-2}$$

The obtained y- intercept is close to the zero-origin point, indicating that τ_{DOPC} scales linearly with the gap area, consistent with free Brownian diffusion of the dye in the pure DOPC membrane. The slope of the fitting rendered a diffusion coefficient of (6.8 ± 0.5) $\mu m^2/s$ which compares well to our confocal measurements as shown in Table 3-1 and to values reported elsewhere.[23]

To further validate that these short diffusion times arise from the strong optical confinement occurring at the surface of the gap regions, we performed experiments on similar antennas with excitation light perpendicular to the antenna gap. In these conditions, the antennas are not resonantly excited, and the excitation field essentially corresponds to that of the surrounding nano-apertures alone. Accordingly, the fluorescence signal is much weaker, and the ACF curves look much noisier as compared to parallel antenna excitation (Figure 3-6). ACF curves for perpendicular excitation could be fitted with a single Brownian diffusion component yielding much longer transient times (1.2 ms – 1.9 ms), which are close to the values obtained upon excitation of the nano-aperture alone (i.e., with no antennas inside). These values are also comparable to the t_2 values of the second contribution obtained from the two-component fitting performed on the ACF curves for parallel polarization excitation of the antennas (please compare to Table 3-2.).

Overall, these results on pure DOPC bilayers validate the application of plasmonic antennas to record the diffusion of individual molecules in lipid bilayers with microsecond time resolution and clearly demonstrate their nanoscale excitation confinement. Additionally, our results show that DOPC bilayers are homogenous down to the nanoscale. It further confirms that the antenna substrates supporting the bilayers are of extreme flatness and quality as no hindering effects on the dye diffusion were observed, neither on the DOPC bilayers nor in solution.

Table 3-2. Fitting of the ACF curves on DOPC bilayers for different antenna gap areas. *Extracted values of the diffusion times $t_{1,2}$ and respective amplitudes $A_{1,2}$ as obtained from the fitting of ACF curves shown in* ***Figure 3-5*** *using a two-component Brownian diffusion model. The shorter times (t_1) correspond to the diffusion times of DiD through the antenna hotspot regions while t_2 corresponds to residual excitation of the dye inside the nano-aperture. The diffusion time values plotted in* ***Figure 3-5 c*** *(and remaining figures in this chapter) correspond to τ_1.*

	τ_1	A_1 (%)	τ_2	A_2 (%)
300 nm²	**(6±1) µs**	**67±3**	**(170±15) µs**	**33±8**
1080 nm²	**(25±3) µs**	**79±8**	**(1.4±0.2) ms**	**21±7**
2025 nm²	**(71±25) µs**	**75±9**	**(1.6±0.3) ms**	**25±10**

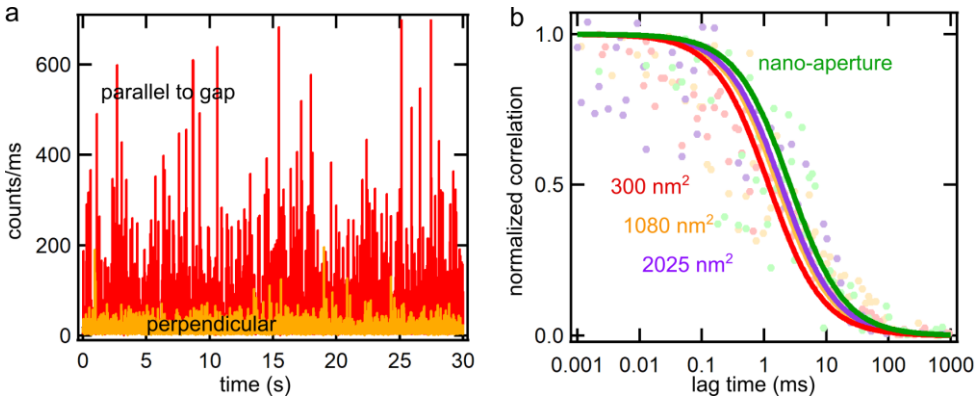

Figure 3-6. ***Fluorescence intensity time traces and ACF curves for DOPC obtained upon parallel and perpendicularly polarized excitation of the antennas.*** *(a) Representative time traces of DiD in DOPC obtained for the smallest antenna gap area (300 nm²) upon parallel (red) and perpendicular (orange) antenna excitation. (b) Fitting of the ACF curves for perpendicular polarization yields diffusion times of (1.2, 1.65, 1.9) ms for the (300, 1080, 2025) nm² antenna gap areas respectively, and 2.6 ms for the nano-aperture.*

It has been recently reported that molecular pinning and interleaflet membrane coupling effects leading to deviations from free Brownian diffusion at the nanoscale are influenced by the properties of the substrate, e.g. plasma-cleaned glass vs. mica

support.[73] We believe that these effects are not present in our DOPC measurements for the following two reasons. First, we observed Brownian diffusion of DOPC down to the nanoscale, with a t_0 intercept close to zero. Second, the gold antenna substrates have been pre-treated with UV/ozone plasma cleaning immediately prior to the bilayer deposition (see Methods Section of this chapter). This treatment leads to a chemically inert and hydrophilic gold surface.[164]

3.3.3 FCS measurements at the nanoscale for binary and ternary lipid mixtures

To shed light on the diffusive behavior of lipid membranes composed of binary and ternary mixtures, lipid membranes composed of DOPC:SM (1:1) alone and with the addition of 10 and 20 mol% of Chol were prepared on top of the antenna array substrates and probed by means of FCS. Figure 3-7 a shows characteristic fluorescent intensity time traces of DiD diffusing across the smallest gap antenna (300 nm^2 hotspot area) in DOPC:SM bilayers and on a ternary mixture containing 20 mol% of Chol. In the presence of Chol, stable macroscopic phase separation occurs, so that depending on the antenna location with respect to the membrane, different fluorescence trajectories are recorded, either probing the Ld phase (Figure 3-7 a, middle trajectory) or the Lo phase (Figure 3-7 a, right trajectory). The enlarged views of single bursts of the individual trajectories show increasing burst durations for the binary and ternary mixtures as compared to DOPC (Figure 3-5 a) consistent with slower diffusion of the dye in these lipid mixtures. ACF curves for DOPC:SM and the ternary mixture of DOPC:SM with 20 mol% Chol for both phases (Ld and Lo) are depicted in Figure 3-7 b.

As for the DOPC measurements, we fitted all the ACF curves using a two-component 2D Brownian diffusion model to account for two distinct diffusion times arising for diffusion within the dimer antenna inside the nano-aperture. We attempted to fit the curves using a three-component fitting but in general the amplitude weight of the third component was either very small (below 3%) and/or rendered a fitting error. We attempted to fit the two ACF curves of the ternary mixture to an anomalous diffusion model which introduces an anomaly parameter $\alpha \neq 1$ in the exponent. However, leaving α as a free parameter did not improve the fitting and rendered α values larger than 1 which, which are unrealistic since they would hint towards super-diffusion such as cellular transport. Hence, we opted for the use of the two-component 2D Brownian diffusion model. The derived diffusion times at

the smallest gap regions (300 nm²) for the different lipid compositions resulted in $\tau_{DOPC:SM}$ = (36 ± 4) µs, and τ_{Ld} = (39 ± 9) µs and τ_{Lo} = (229 ± 30) µs for the 20 mol% Chol ternary lipid mixture. The diffusion times obtained from multiple ACF curves on different 300 nm² gap areas for all the different lipid mixtures are summarized in Figure 3-7 c.

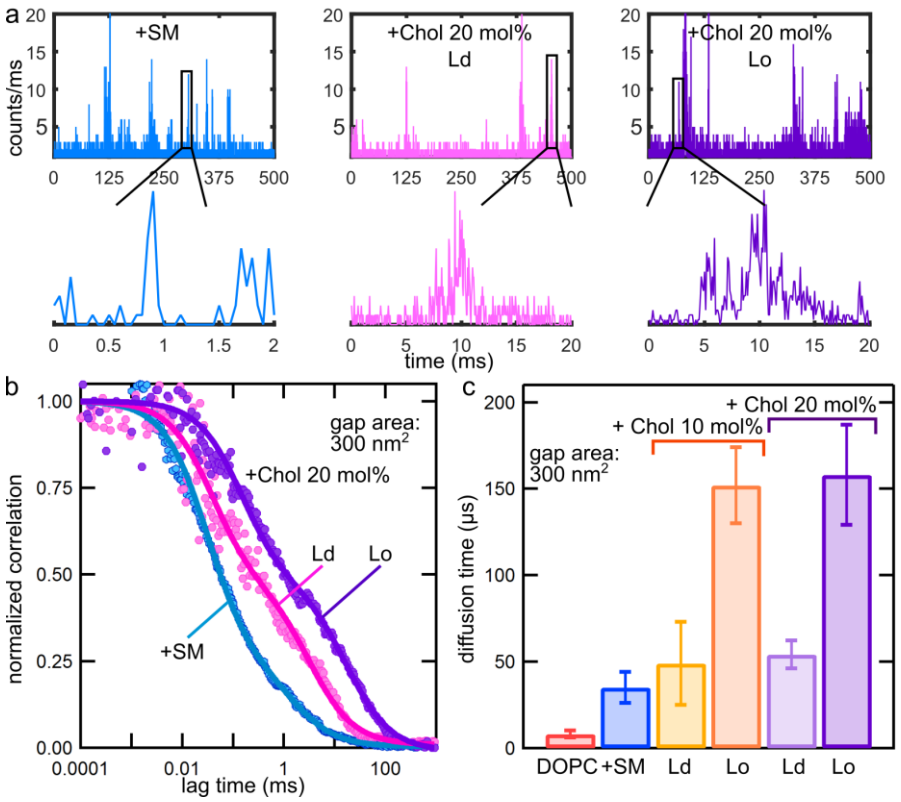

Figure 3-7. ***FCS measurements recorded in nanogaps of 300 nm² area for binary and ternary lipid mixtures.*** *(a) Fluorescence intensity time traces of DiD diffusion in DOPC:SM (1:1) (left, blue) and DOPC:SM (1:1) + Chol (20 mol%) in the Ld (middle, magenta) and Lo (right, purple) phases. Enlarged views of single bursts are also depicted for visual comparison. (b) Normalized ACF curves for the different lipid mixtures. (c) Mean diffusion times of the four probed lipid membranes ± std obtained for the smallest gap area (300 ± 48) nm². Number of measurements: 20 for DOPC; 19 for DOPC:SM; 18 and 15 for Ld and Lo, respectively with Chol 10 mol%; and 17 and 15 for Ld and Lo, respectively with Chol 20 mol%. Between 5 and 10 different antennas of 300 nm² area on 4 to 5 different samples were used for each lipid composition.*

While DiD in DOPC shows the shortest diffusion time, addition of SM slowed down the dye diffusion, consistent with the confocal results. The longest diffusion times were observed for the Lo phase of the ternary mixtures. Interestingly, the diffusion times of DiD in the Ld phase are significantly longer than those obtained in the pure DOPC bilayer, which may already indicate the presence of transient nanoassemblies of Chol in the Ld phase.

To gain more insight into these results we measured the diffusion times for all the lipid mixtures for different antenna gap sizes and over multiple antennas. The data were fitted through the mean diffusion time values to obtain diffusion laws for each lipid composition (Figure 3-8). Two main parameters can be directly extracted from the fitting, i.e., the effective diffusion coefficient which is calculated from the slope of the curves and the y-intercept of the fitting at zero gap areas (τ_0). In the case of DOPC and DOPC:SM bilayers, the intercepts of the fitting cross the origin at nearly zero diffusion time (Figure 3-8 a) consistent with free diffusion of the dye in these lipid bilayers: albeit the diffusion in the DOPC:SM mixture is significantly slowed down as compared to the pure DOPC membrane due to the tighter packing of saturated SM. In strong contrast, positive τ_0 values are obtained for both the Ld and Lo phases in the ternary mixtures containing 10 and 20 mol% Chol indicating that the diffusion of the dye is not Brownian (Figure 3-8 b, c).

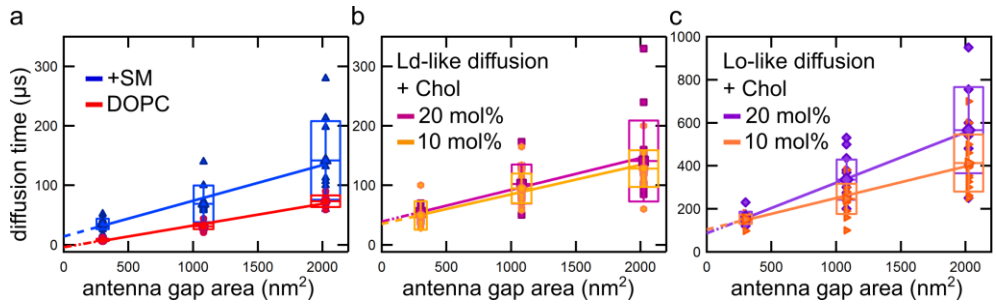

Figure 3-8. ***FCS diffusion laws extended to the nanoscale for different lipid mixtures.*** *Diffusion times vs. antenna gap areas in (a) DOPC and DOPC:SM bilayers. (b) Ld phase for 10 and 20 mol% Chol; and (c) Lo phase for 10 and 20 mol% Chol. The colored dots represent diffusion times acquired from FCS on individual nano-antennas of different gap sizes, while the solid lines are fits through the mean values. Measurements were performed on at least 15 different nano-antennas for each lipid composition on five different samples.*

Results of the effective diffusion coefficients together with the τ_0 values for all lipid compositions are shown in Figure 3-9 a, b. For the ternary mixtures containing cholesterol, the diffusion coefficients in the Ld phase are significantly slower than the one of pure DOPC (mean values of 5.1 and 4.7 $\mu m^2/s$ for 10 and 20 mol% Chol respectively, compared to 6.8 $\mu m^2/s$ for DOPC) (Figure 3-9 a), which is consistent with the longer diffusion times reported in Figure 3-7 c. Moreover, the positive τ_0 values indicate a deviation from Brownian diffusion due to the presence of heterogeneities in the Ld phase caused by the occurrence of nanodomains (Figure 3-9 b). These nanoscopic domains are most probably formed by the presence of SM and Chol in the Ld phase, which reduce the effective diffusion of the dye as compared to the pure DOPC bilayer. A similar and even more pronounced trend is also observed in the Lo phase, where the dye experiences very slow effective diffusion and strong deviation from Brownian motion, indicating also the presence of heterogeneities and nanodomains in this phase (Figure 3-9 a, b). Altogether, these results clearly indicate the occurrence of transient nanoscale heterogeneities in both phases of lipid model membranes which have remained so far beyond the detection limits of conventional microscopy.

Further evidence of the heterogeneity within the Lo and Ld phases for ternary lipid bilayers containing Chol can be inferred from the spread of the diffusion times for similar antennas as a function of the gap area, which we quantified as the deviation from the mean diffusion time. Since the metal thin-film morphology affects the fabrication process of the antennas and leads to variations on the real gap areas, we first estimated the spread in diffusion times arising solely from the differences in gap areas (see Chapter 2, Figure 2-3). Assuming the effect of fabrication inaccuracies to be the origin for a spread in diffusion times, we expected the spread in diffusion times to reduce with increasing gap area as the fabrication process becomes more accurate. In pure DOPC bilayers, DiD shows a spread of the diffusion times that reduces with increasing gap size, confirming this assumption (Figure 3-9 c). In striking contrast, the spread of the diffusion times for the binary and ternary compositions increases significantly with gap size (Figure 3-8 a-c and Figure 3-9 c), suggesting that the dye samples heterogeneous regions of faster and slower diffusion.

These results directly correlate with the positive τ_0 values measured, indicating the occurrence of heterogeneities in both the Lo and Ld phases due to nanoscopic domains that diffuse through the hotspot gap area during the measurements.

Notably, in the case of DOPC:SM, large spreads of the diffusion times are observed for both the (1080 and 2025) nm² antennas, although diffusion is largely free and homogeneous (notice that τ_0 for the DOPC:SM mixture is slightly positive, i.e., (14 ± 4) μs).

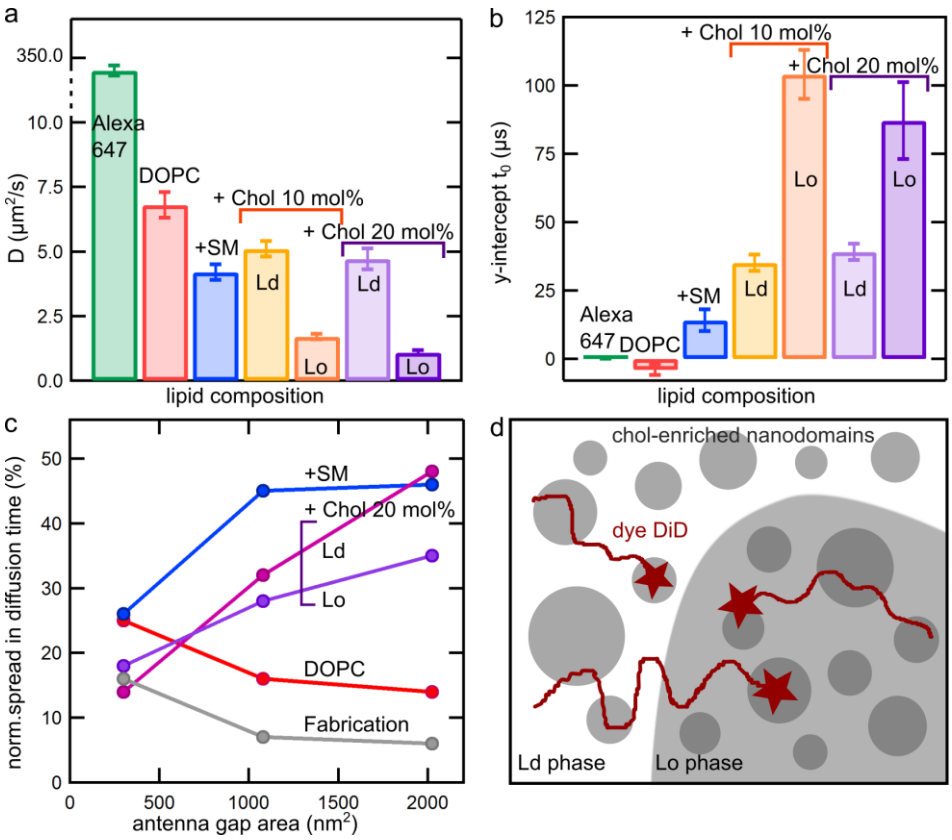

Figure 3-9. ***Planar plasmonic nanogap antennas reveal nanoscopic heterogeneities in the Ld and Lo phases of biological lipid membranes.*** *(a) Effective diffusion coefficients D and (b) y-intercepts t_0 (with ± std for the errors) as extracted from FCS diffusion laws shown in* ***Figure 3-8*** *for the different lipid membrane compositions. Data of the dye Alexa Fluor 647 is included for comparison and showing its expected Brownian free diffusion in solution, i.e., $\tau_0 = 0$ (taken from Ref. 95). (c) Normalized spread in diffusion times (± std/mean × 100%) as a function of the antenna gap area for three different lipid compositions. The gray dots and line correspond to the spread in diffusion times resulting from fabrication inaccuracies of the antenna gaps (variation in gap size/mean gap size) (d) Sketch illustrating the presence of dynamic nanoscopic domains inside microscopic Lo and Ld phases of lipid mixtures containing cholesterol.*

We interpret these results as the occurrence of extremely transient local concentrations of SM within the otherwise homogenous DOPC layer that lead to differences in transient diffusion times but without the occurrence of detectable nanodomains.

The characteristic residence time τ_{res} of the dye in a single nanodomain can be estimated from τ_0 through the relation $\tau_0 = 2\alpha\tau_{res}$, since the confinement time is much larger than the free diffusion time inside the domain, and where α corresponds here in this context to the partition coefficient of the dye in the Ld and Lo phases.[41] In the case of DiD, the values of α correspond to 0.66 for the Ld phase and 0.33 for the Lo phase evaluated for microscopically phase-separated domains[23], and we assume no significant deviations at the nanoscale. Therefore, the residence times inside the different nanoscopic domains yield values for the Ld phase of τ_{res}= (27 ± 3) µs and (30 ± 3) µs for 10 and 20 mol% Chol respectively, and for the Lo phase of (158 ± 9) µs and (132 ± 14) µs for 10 and 20 mol% Chol, respectively. Although from our measurements we cannot directly estimate the sizes of these nanoscopic domains, the large spread of the diffusion times observed for the two larger gap areas (1080 nm^2 and 2025 nm^2) indicates that these gap areas already probe different nanoscopic regions during our measurements. On the other hand, the spread on the diffusion times reduces for the smallest antennas (300 nm^2) and are similar to the variations obtained from the fabrication procedure (Figure 3-9 c). Reduced variations in the diffusion times implies that the sizes of the nanoscopic domains become comparable to the illumination area, which for the smallest antennas is 10 nm in size.

3.4 Discussion

Overall, the results presented in this chapter provide compelling evidence for the existence of nanoscopic domains in both the Ld and Lo phases of multicomponent lipid bilayers containing cholesterol, as illustrated in Figure 3-9 d. We find nanodomains with sizes around 10 nm and short transient residence times around 30 µs for the Ld, and 150 µs for the Lo phase. Nanoscopic domains in the Lo phase have also been recently detected by high-speed single particle tracking reporting on sizes and residence times that agree remarkably well with the values reported in this work using a completely different technique and experimental approach.[76] Interestingly, earlier stochastic models predicted that lipid rafts in living cells would have to be small (≤ 14nm) with an average residence time of ~ 60 µs in order

to facilitate intermolecular collisions between different proteins.[161] These values come very close to our experimentally measured values. Moreover, molecular dynamics simulations of lipid diffusion within rafts and non-raft domains have predicted the existence of transient clusters with sizes around 10 nm and lifetimes in the microsecond range,[169] once more in excellent agreement with our experimental values. Thus, although the plasma membrane of living cells has a much higher complexity than our model lipid bilayers, we propose that the nanoscopic and highly transient domains detected in this model system might exhibit similar biophysical properties as those predicted in living cells.

Strikingly, our results also show the occurrence of nanoscopic domains in the Ld phase, which to our knowledge, have not been detected before the completion of this research. However, there is ample experimental data that supports their existence. Indeed, earlier Förster resonance energy transfer (FRET) measurements showed heterogeneities in the Ld phase that depended on the amount of cholesterol and persisted even at physiological temperatures, hinting towards the existence of nanoscale domains in the Ld phase.[170,171] Furthermore, d-NMR experiments showed a relatively large percentage of saturated lipids (17%) and Chol (20%) in the Ld phase, which is supposedly composed of only DOPC.[160] The presence of SM and Chol will lead to nanoscopic phase separation within the Ld phase with sizes and lifetimes that would most probably depend on the amount of Chol and SM.[74,171] In our experiments, we find that these nanoscopic domains are extremely short-lived with residence times below 30 μs, being probably the reason why they have not been detected before. In fact, the temporal resolution of the high-speed SPT experiments reporting the presence of nanoscopic domains on the Lo phase was 20 μs, which is not enough to detect transient confinements around 30 μs.[74] By combining nanoscale observation areas as provided by plasmonic antennas with microsecond time resolution as afforded by FCS we have been able to resolve transient nanoscopic domains coexisting in both Ld and Lo phases of mimetic lipid membranes. It is worth mentioning that recent advancements in interferometric scattering (iSCAT) microscopy currently allow nanometer localization precision together with microsecond time resolution by the use of 20-40 nm gold beads as labeling probes.[73,74,76] This approach led to high-speed tracking resolving transient nanoscopic confinement in supported lipid bilayers. Provided that careful controls on potential labeling artifacts and background characterization and removal are performed, iSCAT also constitutes an attractive tool to investigate dynamic

biophysical processes at the nanometer scale. A recent comparative study between high-speed iSCAT tracking and STED-FCS revealed that both techniques report on the same molecular diffusion dynamics and relative mobility differences but with differing results in absolute values.[77] Hence given a comparable sample preparation, it seems justified to compare results on molecular diffusion behavior of different techniques providing high spatiotemporal resolution with regard to trends and modes of the nanoscale diffusion. This conclusion appears promising to encourage a multitude of nanoscale diffusion studies by exploiting various techniques aiming at collectively elucidating membrane diffusion and organization at the nanoscale.

3.5 Conclusion

In summary, we have exploited planar plasmonic nanogap antenna arrays to investigate the lateral organization of lipid model membranes at the nanoscale with microsecond time resolution. The suitability of planar antenna arrays has been validated on pure DOPC bilayers obtaining free diffusion over the length scales investigated (down to 10 nm), consistent with a homogenous lipid distribution. Free diffusion was also observed on DOPC:SM binary mixtures, although a large spread of the diffusion times was retrieved indicating local fluctuations of SM within larger areas of solely DOPC, but without formation of detectable domains that would constrain dye diffusion. Addition of cholesterol resulted in microscopic phase separation and the formation of transient nanoscopic domains in both the Lo and Ld phases, with sizes below 10 nm and lifetimes in the microsecond time scale. Since the basic biochemistry operating in lipid model membranes is similar to the one in the plasma membrane, we propose that the nanoscopic domains detected here might correspond to the unstable lipid rafts predicted to exist in living cell membranes.

The results shown in this chapter also underscore the ultra-high spatiotemporal resolution provided by planar nanogap antennas and their enormous potential to unravel the nanoscale complexity of biological membranes. These advantages will be further exploited in Chapter 4 to study the effect of extra-cellular components on the nanoscale partitioning of mimetic biological membranes.

4 Assessing the role of extra-cellular glycans on the nanoscale organization of mimetic membranes[4]

The spatiotemporal compartmentalization of the cell membrane at different scales is arising as a key feature to regulate multiple cellular functions. Different molecular actors have been identified as potential drivers regulating the spatially heterogenous and dynamic organization of the cell membrane. Amongst those, the glycocalyx matrix, located on the extracellular cell membrane, is emerging as an important player to regulate membrane organization, and thus function. Recent intriguing studies suggest that the glycocalyx matrix not only modulates the organization of specific membrane receptors, but importantly, it might also re-pattern the lipid bilayer itself. However, sample preparation challenges and limited techniques to investigate nanoscale membrane dynamics have hampered further studies in this field.

In this chapter, we take advantage of planar nanogap antenna arrays combined with fluorescence correlation spectroscopy to elucidate the influence of glycans on the nanoscale lipid organization in mimetic bilayers of different lipid compositions. Moreover, we complement our studies by the use of atomic force microscopy and force spectroscopy allowing us to correlate dynamic measurements with the morphology and mechanical

[4] The content of this chapter has been submitted to *J. Phys. Chem Lett.* as:

Winkler, P.M., Campelo, F., Giannotti, M. I., García-Parajo, M.F., *Nanoscale imprint of glycans on lipid membrane dynamics unveiled by planar plasmonic nanogap antennas and atomic force spectroscopy.*

properties of bilayers at the nanoscale. Overall, we find that glycans have a profound effect on the dynamics, nanoscale organization and mechanical properties of lipid bilayers that are enriched in saturated lipids and/or cholesterol, such as those present in living cells.

4.1 Introduction

Plasma membranes are ~ 4 nm thick fluid bilayers composed of a plethora of lipids and proteins. The plasma membrane separates the interior from the exterior of cells, thereby controlling many fundamental cellular functions. In the last two decades, lateral compartmentalization of the plasma membrane has emerged as a prominent feature present at different spatiotemporal scales and regulating key cellular functions.[19,172] Much research has been devoted to identify the different molecular actors responsible for this far-from homogenous and dynamic organization. Within the plane of the bilayer, cholesterol together with sphingomyelin and saturated phospholipids have been reported to phase-separate in cholesterol-enriched, liquid-ordered nanodomains, also known as lipid rafts.[1,3,6,13] By selectively recruiting certain types of receptors and/or signaling molecules in to these nanodomains, lipid rafts have been proposed to orchestrate a broad range of cell functions.[2,4] In addition to this lipid-based compartmentalization mechanism, more recent research has extensively focused on the role of the cortical actin cytoskeleton to assist, either passively or actively, on the nanoscale partitioning of the plasma membrane.[3–5] Moreover, it has been postulated that cortical actin might modulate the formation and/or stabilization of lipid rafts, suggesting that different molecular actors can function in a concerted way to provide spatiotemporal modularity to the plasma membrane.[5,173]

A third actor that has been recently proposed as an important modulator of cell membrane organization and dynamics is the glycocalyx matrix, a mesh of sugars or glycans and proteins located on the extracellular side of the cell membrane.[174] Although the role of the glycocalyx matrix regulating multiple functions has been known for decades,[175,176] evidence of its implication regulating the organization of the cell membrane is much more recent. Using super-resolution and single-molecule microscopy-based approaches, we and others have revealed that by compartmentalizing the cell membrane, glycans can modulate the degree of clustering, mobility, and/or molecular interactions of different receptors in the cell membrane and ultimately regulate their function.[177–180] In particular, we showed that the glycan meshwork provides an additional organization layer at the microscale regulating receptor interactions within the cell membrane as well as with downstream partners.[178] In the context of cancer, it has been reported that bulky glycoproteins and glycan networks modulate receptor organization and activation hinting towards a broad physiological relevance.[177] The transmembrane

receptor CD44, immobilized by the cortical actin, was shown to bind to hyaluronic acid (HA), an abundant glycan on the surface of many cells forming a pericellular coat.[179] Freeman et al. further showed that the picket fence of CD44 and cortical actin together with the anchored pericellular coat of HA limit the lateral diffusion of phagocytic receptors and hence restrict the access to phagocytic targets. Along similar lines, Sil et al. showed that the glycocalyx matrix potentially repositions the mesoscale meshwork of CD44 composed of nanoclusters and generated by the underlying cortical actin dynamics.[180]

The emerging interest in elucidating the role of the glycans on cell membranes has reignited studies on mimetic biological membranes. Using confocal fluorescence correlation spectroscopy (FCS), Sahoo and Schwille reported a noticeable effect of certain glycosaminoglycans (GAGs), an important class of glycocalyx constituents, on lipid dynamics in mimetic membranes.[123] The authors concluded that the presence of certain GAGs may slow down lipid diffusion depending on concentration, chemical composition and molecular weight of the carbohydrate polymers. In an intriguing study, glycan networks of inhomogeneous density distribution were found to re-pattern the spatial organization of cholesterol-containing multiphase lipid membranes by stabilizing large lipid domains at the characteristic length scale of the glycan network.[17] Surprisingly, homogeneously distributed glycan networks led to a full suppression of microscopic phase separation. However, the effect of homogeneous or heterogeneous glycan layers on the nanoscale domain organization of cholesterol-containing membranes remains unknown. Overall, these results are exciting since they suggest that glycans might not only alter the nano-and meso-scale organization of specific receptors on the cell membrane, but also the lipid bilayer itself, by either synergizing with or overriding the effect of cholesterol to re-pattern the dynamic organization on the membrane. Unfortunately, the difficulty of creating mimetic bilayers that incorporate glycans together with the limited number of techniques able to address the dynamic organization of membranes at the nanoscale has prevented further studies in the field.

Our combined FCS-nanogap antenna approach (as introduced in Chapter 2) has proven to enable single-molecule detection at the nanoscale at physiologically relevant concentrations. Photonic nano-antennas are metallic nanostructures that enable enhancement and nanometric confinement of the excitation light into illumination hotspots.[95] Our innovative and versatile platform of planar antenna

arrays with different nanogap sizes (10-45 nm) is based on an improved nanofabrication technique combining electron beam lithography, planarization, etch back and template stripping. In benchmarking solution experiments at micromolar concentration, this planar nanogap antenna platform yielded giant fluorescence enhancement factors of up to 10^4-10^5 times together with nanoscale detection volumes in the 20 zeptoliter range (Chapter 2). As described in Chapter 3, we further exploited these planar photonic nano-antennas to resolve dynamic nanoscopic heterogeneities in mimetic membranes in regions as small as 10 nm in size with microsecond time resolution. In the work described in this chapter, we took advantage of this type of planar nano-antenna arrays combined with FCS to investigate the influence of glycans on the nanoscale lipid organization of mimetic bilayers of different molecular compositions. Moreover, we complemented our studies by the use of atomic force microscopy (AFM) and force spectroscopy allowing us to correlate dynamic measurements with the morphology and mechanical properties of bilayers at the nanoscale. Overall, we found that glycans have a profound effect on the dynamics, nanoscale organization and mechanical properties of lipid bilayers that are enriched in saturated lipids and/or cholesterol, such as those present in living cells.

4.2 Methods

4.2.1 Lipids, fluorescent dyes and hyaluronic acid

The lipids 1,2-dioleoyl-sn-glycero-3-phosphocholine (DOPC) and N-stearoyl-D-erythro- Sphingosylphosphorylcholine 18:0 (SM) were purchased from Avanti (*Avanti Polar Lipids, Inc*.). Cholesterol (Chol) ≥99% was purchased from Sigma-Aldrich and the fluorescent dye $DiIC_{18}(5)$ solid (DiD) from *Molecular Probes, Life Technologies Corporation*. Pure Hyaluronic Acid (HA), MW 250k, and biotinylated Hyaluronate Biotin, MW 250k (Purity: >95%) for the dual-color fluorescence imaging in confocal mode were purchased from *Creative PEGWorks*. The fluorescent dye ATTO488 was purchased from *ATTO-TEC GmbH* and was conjugated in-house to Streptavidin.

4.2.2 Fabrication of planar gold nanogap antenna arrays

Planar gold dimer antenna arrays with gaps of different sizes were fabricated onto glass-coverslips at the EPFL, in the group led by Prof. J. Brugger within a European collaboration following a procedure described in detail in Chapter 2. Immediately

prior to the lipid bilayer deposition, the antenna substrates were carefully cleaned with ethanol, MilliQ water rinsing and UV light exposure for 1 minute followed by 3 minutes of ozone treatment.

4.2.3 Fluorescence Microscopy and FCS

The fluorescence imaging and FCS experiments in this chapter were carried out on the same setup as described in Chapter 3. Fluorescently labeled samples were illuminated with an excitation power density of ~2–3 kW/cm^2. The typical measurement duration was 50 s per run, and we calculated the correlation function **G(τ)** of ~20-30s time windows with the commercial software package *SymPhoTime 64*.

The calculated correlation curves $\boldsymbol{G(\tau)}$ were fitted using a two-dimensional Brownian diffusion model, assuming a Gaussian beam profile as introduced in Section 2.2.1 in **Eq. 2-16** but without a triplet contribution thus yielding **Eq. 4-1**:

$$\boldsymbol{G(\tau) = A_1 \frac{1}{1 + (\tau/\tau_{D,1})} + (1 - A_1) \frac{1}{1 + (\tau/\tau_{D,2})}} \quad \textbf{Eq. 4-1}$$

where $\boldsymbol{A_1}$ and $\boldsymbol{\tau_{D,1}}$ are the amplitude and diffusion time of the contribution of the first diffusing species and $\boldsymbol{1 - A_1}$ and $\boldsymbol{\tau_{D,2}}$ are of the second one. As for the work on mimetic membranes explained in Chapter 3 we employed a two-component fitting accounting for the fast diffusion through the nanometric gap region of the dimer antenna and for the slower contribution of molecules diffusing through the nano-aperture.

For the dual-color fluorescence imaging scans of the DiD labeled lipids and the biotinylated HA molecules (labeled with Atto488 conjugated to Streptavidin) a linearly polarized 470 nm picosecond laser diode (*PicoQuant LDH-D-C-470*) in continuous wave mode was used in addition to the 640 nm laser. Both are coupled into the setup through the same optical fiber.

4.2.4 Sample Preparation

We used different substrates depending on the probing technique. The fluorescence imaging and confocal FCS measurements were performed on rigorously cleaned glass coverslips and 30 nm gold films evaporated on cleaned glass coverslips. Glass coverslips were cleaned with steps of ethanol, MilliQ water

rinsing and UV/Ozone treatment. The nanoscale FCS measurements were conducted on nano-antenna arrays following the same cleaning steps. For the AFM measurements we used freshly cleaved mica surfaces. For all substrates, the supported lipid bilayers were prepared following the protocol described in Ref. 181. In short, small unilamellar vesicles (SUVs) of the desired lipid composition of a final concentration of 3 mM were prepared by lipid film hydration with a buffer solution of 150 mM NaCl, 20 mM $MgCl_2$, 20 mM Hepes at pH 7.4 prepared in ultrapure MilliQ water. In the next step, we applied interchanging heat shocks and vortexing at 60 °C, followed by sonification and extrusion through 100 nm pore size filters at 60 °C. Since the same SUVs were used to prepare lipid bilayers for all the experiments, 0.1 mMol % of the red dye DiD was added to the SUV mixture. The SUVs formed into a single lipid bilayer once they were suspended onto the substrate of choice at 60 °C on a hotplate and left to settle for 30 minutes. The lipid compositions of the single SLB examined further were DOPC alone, DOPC:SM (1:1) and DOPC:SM + 20 mol% Cholesterol. The formed SLB on the respective substrates were carefully rinsed with buffer solution and left to equilibrate at room temperature for another 30 minutes prior to the experiments. To investigate the influence of HA on the lipid bilayer, half of the buffer solution was replaced by an HA solution (40 mg/ml) and left to incubate for 30 minutes, rinsed with buffer and equilibrated for another 30 minutes.

4.2.5 AFM and AFM-based force spectroscopy (AFM-FS)

The AFM imaging and AFM-FS experiments in this chapter were performed in a collaboration with Marina Giannotti, PhD at IBEC, Barcelona, Spain and described in some detail below.

AFM imaging was carried out in contact or AC mode using an MFP-3D atomic force microscope (*Asylum Research, Santa Barbara, CA*). Silicon nitride SNL probes (*Bruker AFM Probes, Camarillo, CA, USA*) were used for the measurements (nominal spring constant k = 0.35 N·m−1, maximal forces of 65 nN) calibrated extemporaneously applying the equipartition theorem (thermal noise routine)[182]. The scan speed was set to 1 Hz, and 256×256 pixels were imaged regardless of the image size. The images were minimally processed to enhance the contrast by performing a planefit at order 0, flattening at order 1 and then another planefit again. For the AFM-FS experiments, force-distance curves were recorded over a 2×2 μm^2 area of interest previously imaged, by approaching and retracting the

cantilever tip to the sample at constant velocity of 1 μm·s−1. Force-separation curves were acquired in the force map mode, using an array of 32×32 pixels over the area of interest.

4.3 Results

The complex interplay between the plasma membrane, the glycan network and the actin cytoskeleton is illustrated in Figure 4-1 a. The plasma membrane consists of different lipids forming a fluid bilayer and phase-separating into lipid rafts to which specific proteins partition, e.g. transmembrane receptors. The glycan network may associate with the more ordered lipid rafts and/or glycosylated proteins which can also interact with the actin cytoskeleton via adaptor proteins. This complex multi-layer organization results in the compartmentalization of the plasma membrane at different scales and in triggering signaling cascades. In here, we focus selectively on understanding whether the glycan network has an effect on the lipid membrane organization at the nanoscale or not. To this goal, we chose to work with a biomimetic system consisting of purely lipidic bilayers together with an HA network as a model glycan network. This mimicking system allows us to investigate the direct involvement of the glycan network on the lipid bilayer organization without the influence of glycosylated proteins and/or the cortical actin.

To guarantee a consistent investigation of the influence of a glycan layer on the lipid organization of mimetic membranes by applying FCS in confocal and on nano-antennas as well as by AFM, we rigorously followed the same preparation protocol, which is explained in detail in the Methods section 4.2. In short, the mimetic biological system comprises a single supported lipid bilayer (SLB) on a substrate and an adjacent HA layer obtained by exposing the SLB to an HA solution so it could interact spontaneously (without restrictions) with the SLB. This HA network mimics the glycocalyx, as HA is the most abundant glycosaminoglycan in cells.[183] To assess the influence of HA on SLBs of different molecular composition, we investigated three different lipid mixtures. The first composition is a single component fluid bilayer made of unsaturated 1,2-dioleoyl-sn-glycero-3-phosphocholine (DOPC). The second one, a binary mixture of DOPC and 18:0 sphingomyelin (SM) in equimolar proportions (1:1). And the third one, a ternary mixture composed of DOPC, SM (1:1) with 20 mol % cholesterol (Chol). This latter mixture is known to phase-separate into microscopic liquid ordered (Lo) and liquid disordered (Ld) domains, that may coexist with gel-like SM-enriched domains.[23,184]

Depending on the employed technique, the mimetic lipid bilayers were prepared on top of different substrates: a cleaned glass coverslip for FCS experiments in confocal, directly on the planar gold nano-antenna platform for FCS measurements at the nanoscale, or on freshly cleaved mica for AFM and force spectroscopy (AFM-FS) as sketched in Figure 4-1 b.

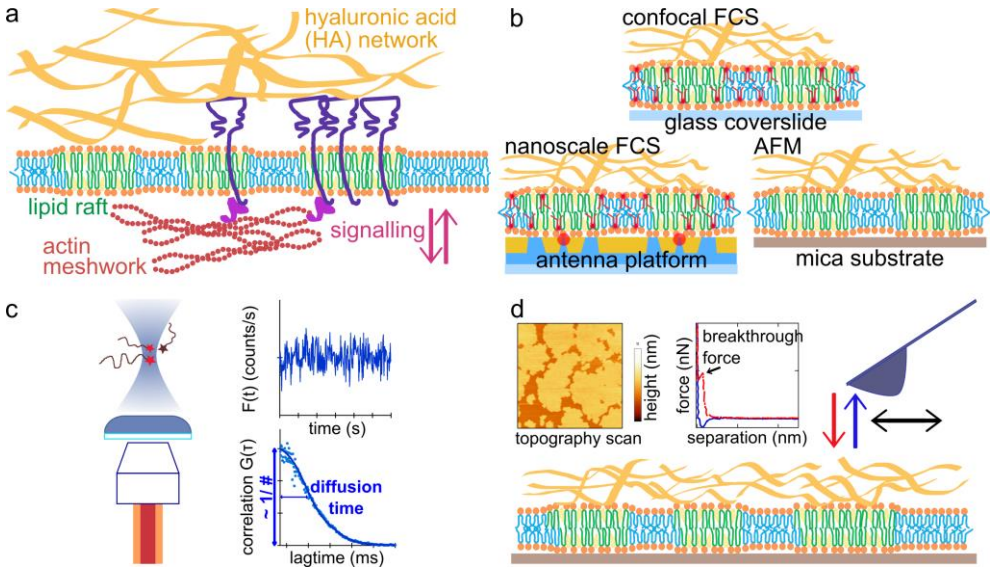

Figure 4-1. ***Experimental approach to investigate the influence of HA on nanoscale lipid organization.*** *(a) Simplified sketch of the plasma membrane of living cells, containing the lipid bilayer together with proximal intra- and extra-cellular components. (b) Illustration of how the biological membrane have been prepared on different substrates, and for the different experiments. On a glass coverslip (top), nanogap antenna platform (bottom left) and on mica (bottom right) for AFM imaging. For the fluorescence experiments on the glass coverslip in confocal and on the nanogap antenna hotspots, the biological membranes were prepared by incorporating the lipophilic fluorescent dye DiD, shown in red. (c) FCS setup, experiment and analysis principle. (d) AFM imaging and force spectroscopy approach.*

To first validate the preparation method and the quality of the SLBs we used standard confocal microcopy. We performed FCS in confocal mode on random locations of the sample to quantify the characteristic diffusion time of the fluorescent dye DiD embedded in the bilayers as sketched in Figure 4-1 c. Note that DiD partitions preferentially into the Ld regions, in our case being regions enriched in DOPC.[166] For the three different lipid bilayer compositions, we measured the

diffusion times of the dye τ_D probed by point measurements in a diffraction-limited spot with a size of ω. From there, we calculated the characteristic diffusion coefficients D by applying

$$\boldsymbol{D = \omega^2/(4 \times \tau_D)} \qquad \textbf{Eq. 4-2}$$

The results are shown in Table 4-1. The values for the diffusion coefficients of the lipid bilayers before the addition of the HA layer are in good quantitative agreement with the values reported previously,[23] thus validating our preparation method.

Table 4-1. *Diffusion coefficients D (mean ± std) are calculated according to* ***Eq. 4-2*** *for lipid bilayers of the three different lipid compositions (DOPC, DOPC:SM(1:1), and DOPC:SM (1:1) + 20 mol% Chol) before and after the addition of HA, probed in point measurements in confocal with ω=285 nm. Values are compared to those reported in Ref. 23 in the absence of HA.*

Lipid composition	***D* [µm²/s] (without HA)**	***D* [µm²/s] from Ref. 23**	***D* [µm²/s] (with HA)**
DOPC	**6.00 ± 0.3**	**6.3 ± 0.2**	**5.6 ± 0.4**
DOPC:SM (1:1)	**1.8 ± 0.4**	**2.6 ± 0.2**	**1.1 ±0.6**
DOCP:SM (1:1) + 20 mol% Chol	**4.6 ± 0.9 (Ld); 0.4 ± 0.1 (Lo)#**	**5.15 ± 0.15 (Ld); 0.255 ± 0.058 (Lo)**	**4 ± 2 (Ld); 0.3 ± 0.2 (Lo)#**

 # The distinction between the macroscopic Lo and Ld domains is based on the fluorescence intensity since the DiD dye preferentially partitions into the Ld regions.[167]

We then incubated SLBs with an HA solution to form an adjacent glycan layer, using 1 mol% biotinylated HA molecules, fluorescently labeled with Atto488 linked through a Streptavidin bond. After the incubation with the HA solution, we performed confocal FCS measurements on random locations to quantify a potential influence of HA on the diffusion of DiD in the lipid bilayers. For the single component DOPC bilayer as well as the binary DOPC:SM bilayer, we did not observe a significant influence of the HA layer on the dye diffusion. However, we measured an increased spread for the diffusion coefficient on the DOPC:SM bilayer, alluding

to a possible effect of HA on this binary mixture (see Table 4-1). In the case of the DOPC:SM:Chol mixture in presence of HA, we obtained similar values of DiD mobility as compared to the ternary mixture alone (see Table 4-1). However, the obtained values of the diffusion coefficient exhibit again a larger spread as compared to bilayers without HA. These results suggest that HA might influence the organization of the ternary lipid mixtures containing Chol, but its effect is averaged out within the observation area provided by confocal illumination.

We also performed dual-color confocal fluorescence images of the ternary lipid mixture (DOPC:SM:Chol) on a glass coverslip, containing the adjacent HA layer (Figure 4-2). The Lo lipid phase, enriched in SM and Chol, corresponds to areas of less fluorescence intensity due to the preference of the dye DiD to partition in the Ld phase.[166] Note that the presence of coexisting gel-like domains enriched in SM is also possible but would remain unresolved by fluorescence since the dye cannot penetrate at all.[166] The adjacent HA layer, shown in green, appears to anti-correlate with the brighter areas of the lipid labeling, as shown in red in the fluorescent imaging scans and line profiles plotted in Figure 4-2. These results indicate that HA preferentially partitions within the more ordered regions of the lipid bilayer.

Then, to investigate the influence of the HA layer on the dynamics of the different lipid mixtures at the nanoscale, we performed FCS experiments using planar gold nanogap antennas (Figure 4-1 c). The design of the planar nano-antenna used here features a nanogap gold dimer (half-sphere of 80 nm diameter each) centered in a 300×140 nm^2 nano-aperture. As explained in Chapter 2, the central nanogap between the gold dimer creates a highly confined fluorescence hotspot, while the surrounding nano-aperture suppresses the fluorescent background. Large arrays of these nanogap antennas of different gap sizes (10-45 nm for the measurements reported in this chapter) were nanofabricated at a spatial separation of 4 μm between antennas, allowing for multiple experiments on individual nano-antennas on the same biological sample.

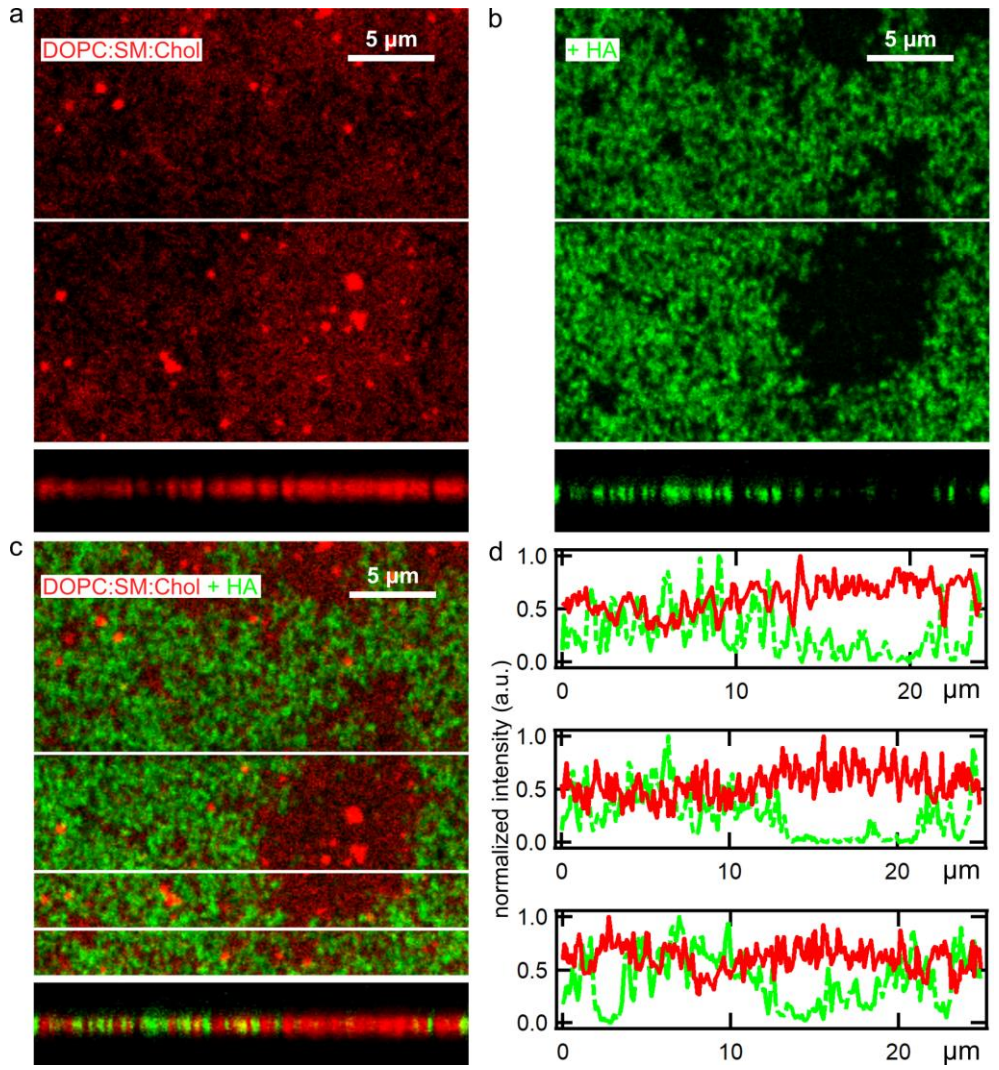

Figure 4-2. ***Confocal FCS on a ternary lipid bilayer in presence of HA****. (a) Representative fluorescence image of the DOPC:SM:Chol (20mol%) lipid membrane (red) in presence of HA (green). (b) x-z scans at the positions indicated by the white lines. (c) Merged x-y image together with the same merged z-projection as shown in (b). (d) Three representative fluorescence profiles taken at three different locations on the sample, as highlighted by the while lines in (c).*

We have previously shown that bilayers of different lipid compositions form nicely on top of the gold antenna substrates and we have not observed sticking effects that could artifactually affect the mobility of the dye within the bilayer (refer to Chapter 3). Yet, since HA can affect the organization of the lipid bilayers, we first assessed

the quality of SLB-HA deposited on bare gold substrates by standard confocal microscopy (Figure 4-3). Although the resultant bilayer becomes somewhat more heterogeneous on this type of substrate, a clear anti-correlation between the DiD and HA signals was still observed, similar to that observed on SLB + HA deposited on glass.

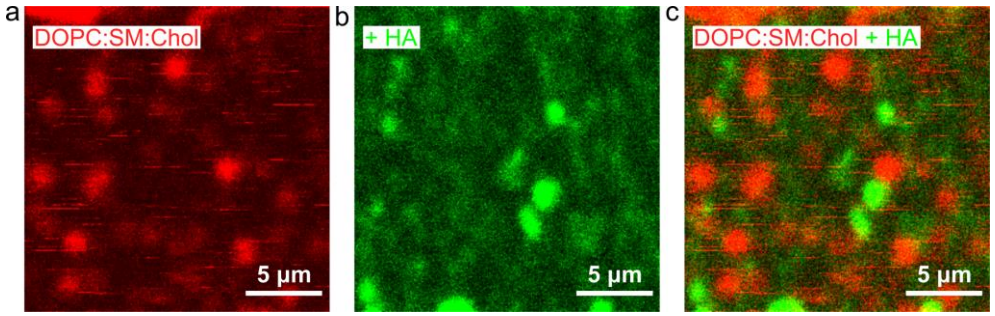

Figure 4-3. ***Confocal FCS of a ternary lipid bilayer in presence of HA deposited on a gold substrate.*** *Representative fluorescence image of a DOPC:SM:Chol SLB (a, red) incubated with HA (b, green). (c) The merge of (a) and (b) is shown.*

Our experimental pipeline to conduct nano-antenna-FCS measurements comprised the following steps. First, the lipid bilayer was prepared on top of the nano-antenna platform. Second, we excited the antennas using a single-molecule sensitive confocal set-up with 640 nm laser illumination and polarization parallel to the gap to achieve maximum field enhancement and confinement, as discussed in Chapters 2, 3. Third, the fluorescence intensity of the diffusing dye DiD was recorded on three different gap sizes of nominally 10, 30 and 45 nm for multiple antennas. Fourth, after an incubation period with HA, another series of FCS measurements on antennas of different gap sizes was performed. Finally, we correlated the collected intensity traces in time and fitted each one of them individually with a two-component 2 D diffusion model (**Eq. 4-1** in the Methods section 4.2.3) to obtain the characteristic diffusion time. We chose a two-component fit to account for the fast diffusion through the confined antenna gap area and the slower background diffusion together with other contributions from the box surrounding the antennas. We have already employed this fitting approach for the FCS analysis in solution (Chapter 2) and on lipid model membranes (Chapter 3). Finally, we plotted the obtained fast diffusion times as a function of the antenna gap size on multiple antennas to derive the FCS diffusion law at the nanoscale. The FCS diffusion law consists of a plot of the obtained diffusion times τ vs. different observation areas

(ω^2) as established by Lenne and coworkers to asses characteristic diffusion behavior at scales smaller than accessible.[40,41] We extended this plot to the nanoscale by including the three antenna gap areas in addition to the confocal area. By a linear fit to

$$\boldsymbol{\tau(\omega^2) = \tau_0 + \omega^2/(4 \times D)} \quad \textbf{Eq. 4-3}$$

the y-intercept τ_0 and the diffusion coefficient D can be obtained. In the context of FCS diffusion laws, a significant y-intercept τ_0 is a strong indication that nanoscale diffusion is deviating from free Brownian behavior due to the occurrence of domains or a meshwork at scales smaller than those accessible by the employed technique. This outlined experimental pipeline was applied to each of the three different bilayer compositions probing the lipid dynamics before and after the incubation with HA.

We first interrogated the homogeneous single component DOPC bilayer by the nanogap antennas. The purpose here is twofold. First, to validate the antenna approach and second, to investigate how HA interacts with the DOPC bilayer. In Figure 4-4 a representative FCS curves are depicted, recorded on the smallest antenna gap (nominally 10 nm in size) before and after the addition of the HA layer and compared to a representative confocal FCS measurement of the DOPC bilayer. The confinement to ultrasmall antenna hotspots is confirmed by the evident shift to shorter diffusion times when comparing the FCS curve from the nano-antenna to the confocal case, consistent with results shown in Chapters 2 and 3. Moreover, the presence of the HA layer did not significantly affect the diffusion times of DiD in the DOPC bilayer, a result that is in agreement with the confocal FCS measurements (see Table 4-1). To further validate these results, we generated diffusion law plots for multiple antennas of different gap sizes and confocal illumination (Figure 4-4 b, c). The resulting diffusion coefficients for the DOPC bilayer in the absence and in the presence of HA yield similar values (within the standard deviation), namely D_{DOPC} = 6.4 ± 0.2 μm²/s and $D_{DOPC+HA}$ = 6.3 ± 0.1 μm²/s. These two values compare well to the values obtained for confocal FCS experiments probing a DOPC bilayer (see Table 4-1), and as previously reported in Ref. 23, and in Chapter 3. In addition, the τ_0 values (y-intercept) were similar and close to zero for DOPC before and after the addition of HA (-7 ±1 μs for DOPC and -6 ±1 μs for DOPC + HA), confirming that the DOPC diffusion remains Brownian at the nanoscale in presence of the HA layer. To assess the variations in diffusion times for different

antennas we calculated the normalized spread in diffusion times (norm. spread) for each of the three gap areas for DOPC alone and DOPC + HA (Figure 4-4 d). The norm. spread is expressed as the percentage of the value of the interquartile range together with an estimation of the accuracy to fabricate each of the three gap areas divided by the respective median diffusion time per gap size. As expected, the fabrication uncertainty decreases with increasing gap area since the fabrication becomes more accurate (for details refer to Chapter 2). A similar trend was found for DOPC alone and DOPC + HA, indicating that small deviations between antenna measurements mostly stem from fabrication inaccuracies rather than from the presence of hindering nanodomains on the sample.

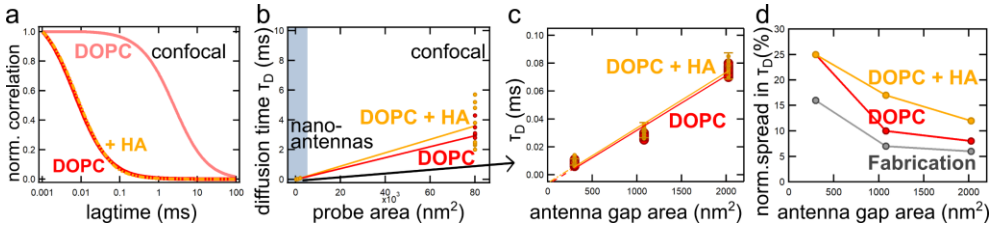

Figure 4-4. ***Confocal and nanoscale FCS diffusion dynamics of a single component bilayer before and after HA addition.*** *(a) DOPC correlation curves for the smallest antenna gap before and after HA addition in comparison to confocal (b) FCS diffusion laws extended to the nanoscale shown in (c) for DOPC before and after incubation with HA. (d) Normalized spread in diffusion times for DOPC before and after addition of HA and compared to fabrication inaccuracies.*

Besides probing nanoscale diffusion, we also examined the morphology of the SLBs by AFM following the experimental scheme shown in Figure 4-1 c. The addition of the HA layer on top of the single component DOPC bilayer did not lead to any obvious reorganization such as the occurrence of nanodomain formation or reshaping of its topography (Figure 4-5). Altogether, the lack of changes in the obtained diffusion coefficients, the negligible y-intercepts obtained from the FCS diffusion law plots down to 10 nm inspection, and an unaltered topography from AFM images, strongly indicate that HA does not affect the spatiotemporal organization of DOPC bilayers at the micron- nor the nanoscale.

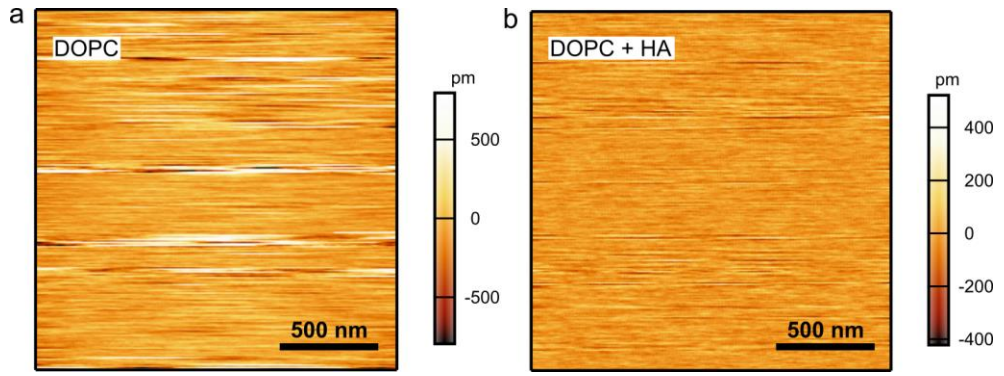

Figure 4-5. ***Nanoscale topography of a single component lipid bilayer prior to and after HA addition****. AFM topography images of a DOPC bilayer before (a) and after (b) the addition of HA.*

We then prepared bilayers composed of a mixture of SM and DOPC at equimolar concentrations DOPC:SM (1:1) and studied the effect of HA on these bilayers. Representative topography images by AFM for the binary mixture before and after addition of the HA layer are shown in Figure 4-6 a and b, respectively. In both cases we observed the presence of domains of heterogenous sizes, indicative of the formation of different lipid phases. However, a qualitative, visual inspection of both topographic images (see also the enlarged AFM images, Figure 4-6 c, d) indicate differences in the domain morphologies. While for DOPC:SM the domain edges appear quite sharp, well-defined and spiky, they become more homogeneously distributed and spherically shaped upon HA addition.

To corroborate this first visual impression we performed atomic force spectroscopy measurements to quantitatively analyze the membrane remodeling taking place after HA incubation. In this type of measurements, a vertical compression of the membrane by the AFM tip at constant loading rate induces an elastic deformation and sudden breaking of the membrane.[185] The maximum force applied by the AFM tip at which the bilayer breaks, so-called the yield or breakthrough force F_b, is seen as a discontinuity in the approaching force curve (Figure 4-1 d). The breakthrough force is directly related to the membrane lateral packing. Therefore, F_b is characteristic of the chemical structure of the lipid molecules and of the bilayer's composition when formed by more than one lipid.[186] F_b is furthermore affected by the surrounding environment altering lateral interactions between the lipid molecules.[187]

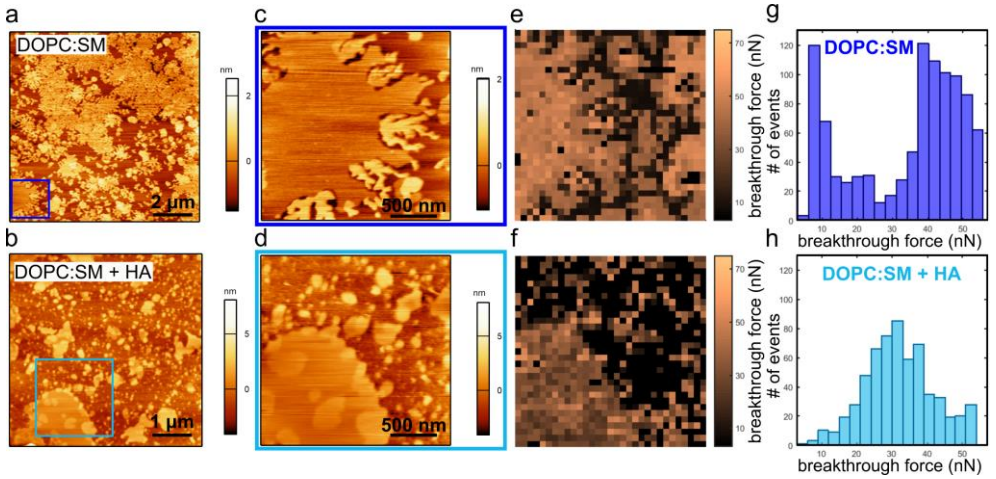

Figure 4-6. ***AFM topography of a binary lipid bilayer before and after HA addition.*** *Representative AFM topography images of the DOPC:SM (1:1) bilayer before (a) and after the HA addition (b) together with 2 µm ×2 µm zoom-ins (c, d, respectively). (e, g) Breakthrough force map (e) together with the evaluated breakthrough force histogram (g) for the same DOPC:SM region as in (c). (f, h) Breakthrough forcemap (f) and breakthrough force histogram (g) for DOPC:SM + HA in the region of (d). Note that for both breakthrough force histograms (g, h) values close or equal to zero were excluded since they correspond to regions where no clear discontinuity in the approach force curve could be distinguished.*

We acquired pixel-by-pixel force-retraction curves (pixel size of 63 nm) on the same zoomed-in regions as imaged in topography (Figure 4-6 c, d), calculated the F_b for each curve and generated 2D breakthrough force (F_b) maps of the DOPC:SM membrane before and after HA incubation (Figure 4-6 e, f). Besides a slight lateral shift due to the mechanical drift of the set-up, the F_b maps correlate well with the topographical features observed on the AFM images. Indeed, for the DOPC:SM bilayer, the thicker domains observed in the topography image (Figure 4-6 c) correspond to larger F_b values (Figure 4-6 e) and can therefore be most likely attributed to the more ordered domains enriched in SM.[188,189] To better quantify these differences, we generated histograms of the F_b values, excluding values close to zero on regions where we were not able to distinguish a clear discontinuity in the approach force (Figure 4-6 g, h). The F_b histogram for the DOPC:SM bilayer (Figure 4-6 g) exhibits a clear bimodal distribution with a lower force centered around 8 nN and a considerably higher force with a larger spread centered at ~38 nN. The lower force is higher than the F_b value of ~4-5 nN reported in the literature

for a pure DOPC bilayer.[190] Hence, we assign this lower force peak at ~8 nN to Ld bilayer regions composed of mainly DOPC and mixed with a small fraction of SM. The second broader histogram with a peak at higher rupture forces of ~38 nN, lies within the range reported for gel-like membranes.[191] Compared to literature, the coexistence of gel-like domains in binary DOPC:SM model membranes has been shown for compositions containing 23-81% of SM, and nanodomains have been detected to occur in the range of 10-15% SM already.[192–194] Therefore, we assign these higher rupture forces to regions of SM of different packing densities containing fewer DOPC molecules. In strong contrast to the results obtained on DOPC:SM, addition of the HA layer resulted in a much broader and unimodal distribution of F_b values (Figure 4-6 h). Indeed, the F_b distribution is centered at around 29 nN which is between the most probable values of the bimodal distribution obtained for the DOPC:SM bilayer. Although the correlation between the topography and the F_b maps is somewhat preserved, the mechanical stability of the distinct phases observed for the DOCP:SM bilayers becomes similar and more indistinguishable upon the addition of HA.

To further investigate the effect of HA on DOPC:SM bilayers and to rationalize the AFM results described above, we moved to fluorescence measurements. Confocal images of DOPC:SM + HA confirmed the presence of HA as well as its preferential partitioning to higher ordered regions of the bilayer (i.e., where the DiD signal is weaker) (Figure 4-7 a). FCS measurements at the nanoscale by means of antennas of different gap sizes showed a considerable influence of HA on the dynamics of the DOPC:SM bilayers. Measurements performed on the smallest antenna gap (10 nm) yielded a diffusion time of $\tau_{DOPC:SM}$ = 24 ± 3 µs for the correlation curve shown in Figure 4-7 b (dark blue). Upon HA incorporation we obtained a diffusion time of $\tau_{DOPC:SM+HA}$ = 36 ± 4 µs, showing a slowdown of DiD diffusion (Figure 4-7 b). The strong influence of HA on the packing of a DOPC:SM bilayer becomes more apparent if looking into the mean diffusion times of the 10 nm gap size depicted in the diffusion law plots in (Figure 4-7 c) yielding values of $\tau_{DOPC:SM}$ = 36 ± 9 µs and $\tau_{DOPC:SM+HA}$ = 92 ± 26 µs, respectively. After fitting all the correlation curves for three different nano-antenna gap sizes, we obtained diffusion law plots for DOPC:SM with or without the HA layer (Figure 4-7 c). In the absence of HA, the plots could be accurately fitted using **Eq. 4-3**, yielding values of $D_{DOPC:SM}$ ~4.14 ± 0.03 µm²/s and a small but significantly positive offset of τ_0 = 18 ± 4 µs. This positive offset is indicative of the occurrence of nanodomains.[40,41,122] Moreover, the normalized

spread in diffusion times for the DOPC:SM membrane follows an opposite trend to the one resulting from the fabrication inaccuracies (Figure 4-7 d), i.e., increased spread in diffusion times for the larger antenna gaps. The spread in diffusion times can be explained by the occurrence of nanoscale heterogeneities that alter the diffusion of DiD, with shorter diffusion times corresponding to more fluid-like nanoscale regions and longer diffusion times associated with a more compact nanoenvironment. Overall, these results can be directly correlated to the AFM data shown in Figure 4-6 a-d and indicate the existence of nanodomains with a broad range of sizes, the smallest detected ones having sizes comparable to our smallest gap (10 nm) or smaller.

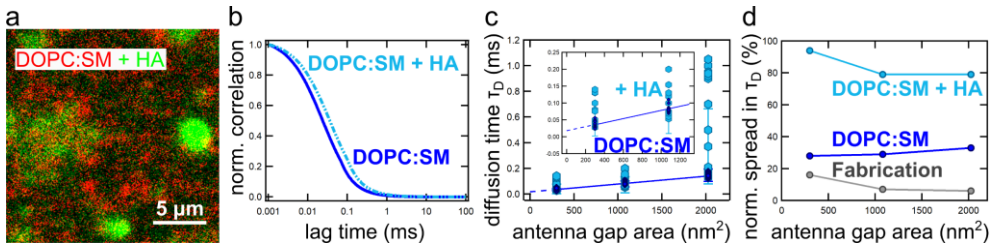

Figure 4-7. ***FCS dynamics of a DOPC:SM lipid bilayer before and after HA addition.*** *(a) Dual color confocal fluorescence image of a DOPC:SM bilayer (red) and HA layer (green) deposited on a glass coverslip. (b) Representative correlation curves of DOPC:SM before and after HA addition, obtained with the nominally 10 nm gap antenna. (c) FCS diffusion laws for the two bilayer conditions (the inset focuses on the two smaller gaps). (d) Normalized spread in diffusion times for the DOPC:SM bilayer before and after HA addition and compared to fabrication inaccuracies.*

Remarkably, HA addition led to a shift to longer and much more disperse diffusion times for all three investigated gap sizes. The disperse data sets of the diffusion times for each gap size yields an inadequate linear regression fitting with a coefficient of determination R^2 = 44% for the DOPC:SM + HA. In contrast, R^2 for the pure DOPC:SM bilayer is 92%. Although we are not able to draw conclusions about the explicit nature of the HA interaction with DOPC:SM bilayers from these ill-defined diffusion time plots, our results clearly indicate that HA has a major impact disturbing the full ordering of the bilayers down to scales of 10 nm in size. Qualitatively, these results also agree with the F_b plots, in which distinct phases became indistinguishable in terms of the rupture forces upon HA incorporation (Figure 4-6 h).

We finally assessed the effect of HA on ternary lipid mixtures composed of DOPC:SM (1:1) and 20 mol% Chol. First, we imaged the SLB with AFM (Figure 4-8 a, left). Three clearly different phases are resolved in the AFM images, which were also confirmed by force-retraction measurements at arbitrary locations. Comparing to literature,[184] the ternary mixture of DOPC:SM (1:1) + 20 mol% Chol is prone to phase-separate in three phases with the thickest domains being reminiscent of gel-like SM-enriched domains (indicated with arrows in Figure 4-8 a, left). However, these three phases could only be detected by AFM and not in confocal fluorescence images since DiD cannot penetrate into gel-like regions.[166] HA addition visibly perturbed the DOPC:SM:Chol bilayers, as inspected by AFM, so that the three-lipid phases could not be unambiguously identified (Figure 4-8 b). In general, these samples were much more difficult to image and appeared systematically blurrier due to increased interactions between the AFM tip and the sample. We also performed phase-shift contrast imaging on the same regions of both samples (Figure 4-8 a, b, right images). In general, the phase signal changes when the probe encounters regions of different compositions.[195] While the phase image of the DOPC:SM:Chol bilayer is sharp and capable of retrieving the different phases of the bilayer (Figure 4-8 a), a much more blurred behavior was obtained upon HA addition (Figure 4-8 b). Thus, although these images clearly show the presence of HA and visual perturbation of the bilayers, it was not possible to make further conclusions regarding a potential HA-dependent re-patterning in the lipid organization of these bilayers.

Since AFM can potentially introduce unwanted tip-sample interactions, in particular in the case of sticky molecules such as HA, we moved once more to fluorescence measurements. As mentioned above, confocal FCS measurements yielded similar dye mobility in presence of HA as compared to the ternary mixture alone. However, we obtained a significantly larger spread for the dye mobility suggesting that the influence of HA is averaged out by the larger illumination area provided by confocal detection (see Table 4-1). To discern alterations of the nanoscale lipid dynamics triggered by the adjacent HA layer on a ternary mimetic membrane, we performed FCS experiments on the nanogap antenna platform. Representative FCS curves for the smallest antenna gap size of 10 nm are shown in Figure 4-8 c.

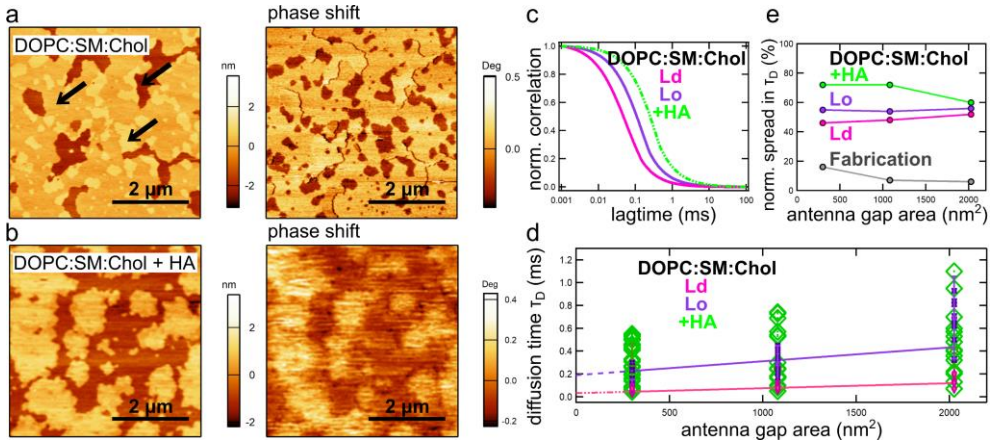

Figure 4-8. ***FCS dynamics and topography of a ternary lipid bilayer before and after HA addition.*** *Representative AFM topography and phase shift images of the ternary lipid mixture before (a) and after HA incubation (b). Black arrows in the topographic image (a) pinpoint to the three different phases retrieved. (c) Representative correlation curves for the smallest antenna gap size of the ternary mixture with and without HA. In the absence of HA, correlation plots could be assigned as belonging to the Lo or Ld phases (magenta and purple lines). In the presence of HA this distinction could not be made (green line). (d) FCS diffusion laws obtained from measurements on the three different gap sizes. (e) Normalized spread in diffusion times.*

As previously reported, the two representative correlation curves for the ternary mixture in the absence of HA correspond to DiD diffusion in the Ld (i.e., shorter diffusion times) and Lo (i.e., longer diffusion times) phases (Chapter 3). In presence of the HA layer, this distinction is abrogated, and on average the dye is further slowed down. Figure 4-8 d shows the calculated diffusion times versus the three gap sizes investigated (diffusion law plots) for multiple antennas for the ternary mixture alone and after HA addition. In the absence of HA, we recover the two characteristic diffusion coefficients D_{Ld} = 6 ± 1 µm²/s, D_{Lo} = 2.1 ± 0.4 µm²/s and positive offsets of τ_{Ld} = 32 ± 9 µs, τ_{Lo} = 190 ± 10 µs corresponding to nanodomains inside the Ld and the Lo phases, respectively, and in full agreement with previous findings (Chapter 3). Remarkably, in the presence of HA, the diffusion times become largely spread, regardless of the antenna gap size (Figure 4-8 d). The spread is significantly larger than the one already obtained for the binary DOPC:SM + HA system, preventing also in this case further fitting of the data. The normalized spread in diffusion times confirms the existence of nanoscopic heterogeneities within both the Ld and Lo phases in the absence of HA (Figure 4-8 e), as previously

reported (Chapter 3). However, the spread in diffusion times after addition of HA becomes even larger suggesting a considerable glycan-lipid interaction already emerging at 10 nm or less, since the largest spread is recorded for the smallest gap size (Figure 4-8 e). We propose that the HA layer stabilizes and further enhances the nanoscopic heterogeneities which already coexist in the ternary mixture due to the presence of Chol. Both the results by AFM and on the nano-antennas jointly confirm the influence of the HA layer on the micro- and nanoscale lipid organization which is reported here for the first time to our knowledge.

4.4 Discussion

To get a hint of a possible mechanism driving the interaction between HA and SM we looked into the chemical molecular structures of SM and HA in comparison to the one of DOPC. Both SM and HA have a high H-bonding capacity facilitating bonds formed between the OH groups of HA and the NH groups of SM.[196,197] Via these bonds, HA could partially penetrate in between the SM head groups, which would thus help in the partitioning of the membrane.[196,198] One hypothesis is that HA plays an intercalating role in a similar way as Chol does to induce or facilitate nanodomain formation in lipid mixtures containing SM. In fact, we observed less microscopic segregation between SM and DOPC in favor of enhanced nanoscopic heterogeneities. However, resolving if HA is playing this intercalating role and inducing the formation of nanoscale heterogeneities would demand more chemically sensitivity methods. Indeed, the importance of the chemical structure and affinities for the lipid-glycan interaction has been already pointed out in the study of Sahoo and Schwille.[123] In that work, the authors probed the influence of different glycosaminoglycans on the lipid dynamics of a supported DOPC bilayer (doped with 5 mol% 1,2-Dioleoyl-3-trimethylammonium propane (DOTAP), a cationic lipid surfactant) and reported a noticeable effect related to the presence of certain carbohydrate polymers. Their work further stated the glycan concentration and molecular weight as influencing parameters, which would be interesting to study at the nanoscale.

Earlier investigations on the role of glycans re-patterning phase separation on ternary mixtures containing cholesterol showed that homogeneously distributed glycan networks suppress microscopic phase separation in these membranes.[17] However, that work was performed by using diffraction-limited confocal microscopy leaving the open question of whether suppression of phase separation

also occurs at the nanoscale or not. By exploiting our combined planar nanogap antenna arrays together with FCS and AFM we were able to resolve the influence of HA on lipid organization at the nanoscale. We observed that HA preferentially interacts with SM, inducing and enhancing the formation of nanoscopic heterogeneities in multicomponent lipid membranes. To reconcile our findings with the confocal studies, we put forward that the presence of HA enhances the formation of nanoscopic lipid heterogeneities in multicomponent lipid membranes which may appear as a microscopically "smeared out" or homogeneous when inspected by techniques that lack the required nanometric spatial resolution.

The occurrence of an induced and/or enhanced formation of nanoscopic lipid heterogeneities in multicomponent lipid membranes by HA, as observed here, might have implications for our understanding of living cell membranes, which are abundant in glycolipids and glycoproteins. In a similar way by which the cortical actin cytoskeleton has been implicated in the formation and/or the regulation of lipid raft sizes,[3,5,13] our results advocate for a role of the glycocalyx matrix regulating the lipid bilayer organization at the nanoscale. Such a glycan-dependent re-patterning might have consequences for the way receptors and lipids interact with each other in the plane of the bilayer, and thus potentially influence their function.

4.5 Conclusion

In summary, we have demonstrated that planar photonic nanogap antennas together with FCS and combined with AFM can be exploited to elucidate the impact of glycans on the lipid nanoscale organization of mimetic biological membranes of different compositions. Our data strongly suggest that HA and cholesterol synergistically contribute to nanodomain partitioning of multicomponent membranes at the nanoscale. Our combined approach provides the required spatiotemporal resolution, mechanical sensitivity, and delivers quantitative parameters at the nanoscale that might highly benefit the modeling of biological systems.

In the scope of this dissertation we resolve the nanoscale lipid dynamics in living cells with our combined FCS-nanogap antenna platform in the subsequent Chapter 5. In the last project in Chapter 6 we address the questions of how multiplexing FCS on our antenna platform in living cells at the nanoscale becomes reality.

5 Planar antennas to address the complexity of living cell membranes[5]

One of the overarching goals of this thesis has been to gain insight into the nanoscale dynamics of the plasma membrane in living cells. The spatial organization and diffusion dynamics of membrane constituents (lipids and proteins) occurring at the nanoscale largely influence cellular processes such as transmembrane signaling, intracellular trafficking, and cell adhesion.[2,157] In Chapters 3 and 4 of this thesis we demonstrated the application of planar photonic antennas of different gap sizes to address the dynamic nanoscale complexity of mimetic biological membranes with unprecedented spatiotemporal resolution.

In this chapter, we exploit similar nano-antenna platforms together with fluorescence correlation spectroscopy (FCS) to study the characteristic diffusion dynamics of phosphoethanolamine (PE) and sphingomyelin (SM) in the plasma membrane of living cells at the nanoscale. Fluorescence burst analysis and FCS measurements performed on nano-antennas of different gap sizes show that, unlike PE, SM is transiently trapped in cholesterol-enriched nanodomains of 10 nm diameter with short characteristic trapping times around 100 µs. Removal of cholesterol led to the free diffusion of SM, consistent with the dispersion of nanodomains. Our results thus confirm the

[5] The content of this chapter has been published in:

Regmi, R., **Winkler, P.M.**, Flauraud, V., Borgman, K.J.E., Manzo, C., Brugger, J., Rigneault, H., Wenger, J. and García-Parajo, M.F., *Planar optical nanoantennas resolve cholesterol-dependent nanoscale heterogeneities in the plasma membrane of living cells.* Nano Letters, 2017 (10), pp.6295-6302.

existence of highly transient and fluctuating nanoscale assemblies enriched by cholesterol and sphingolipids in living cell membranes, also known as lipid rafts. Quantitative data on sphingolipids partitioning into lipid rafts is crucial to understand the spatiotemporal heterogenous organization of transient molecular complexes on the membrane of living cells at the nanoscale. In addition, the results presented in this chapter demonstrate the full biocompatibility of our planar nano-antenna arrays and their usefulness for biophysics and live-cell research to reveal details that remain hidden in confocal diffraction-limited measurements.

5.1 Introduction

The nanoscale spatial organization and diffusion dynamics of the plasma membrane constituents (lipids and proteins) play key roles influencing cellular processes such as transmembrane signaling, intracellular trafficking and cell adhesion.[2,157] It has been postulated that sphingolipids, cholesterol, and certain types of proteins can be enriched into dynamic nanoscale assemblies or nanodomains, also termed lipid rafts.[9,13,45] Lipid rafts have been defined as highly dynamic and fluctuating nanoscale assemblies of cholesterol and sphingolipids that in the presence of lipid- or protein-mediated activation events become stabilized to compartmentalize cellular processes.[2,4,7] However, the true nature of these nanodomains remains debated with many conflicting results and predicted domain sizes in the broad range of 10-200 nm, primarily because of their transient nature and nanoscopic sizes.[7,9,10,36,40,54,76]

Most of the investigations on the living cell membrane dynamic organization have been based on fluorescence recovery after photobleaching (FRAP)[199] and single particle tracking (SPT)[3,35]. Both techniques are limited either in space (with μm^2 probe area in FRAP) or in time (with millisecond temporal resolution in SPT). Fluorescence correlation spectroscopy (FCS) is a widely adopted alternative for studying dynamics and biomolecular interactions as introduced in Chapter 2. However, conventional FCS on confocal microscopes is unable to resolve the nanoscale organization of lipids due to the limited 200-350 nm spatial resolution set by diffraction. Various approaches have been implemented over the past decade to breach the diffraction limit in FCS, but dynamic membrane studies have so far remained above a 40-50 nm detection size. For instance, stimulated emission depletion (STED) microscopy constrains the excitation spot down to ~40 nm[200] and has been combined with FCS to explore the nanoscale dynamics occurring in lipid membranes of living cells.[60,62–64]

An alternative strategy takes advantage of nanophotonic structures to engineer the light intensity distribution at the nanoscale.[80] As summarized in Chapter 1, notable designs include zero-mode waveguides,[87–90,93] bowtie structures,[104,201,202] gold nanorods,[120] and subwavelength tip based NSOM probes.[57,203] These various approaches allow confinement of the illumination light in the range of 50-100 nm. Resonant optical nanogap antennas have shown great potential to further constrain the laser light on a sub-20 nm scale[95] and greatly enhance light-matter interactions.[99–101,118] However, so far the applications of such resonant nanogap

antennas have been mostly employed to probe fluorescent molecules in solutions at micromolar concentrations.

As outlined and benchmarked in Chapter 2 our gold nanogap antenna approach offers high spatiotemporal resolution at physiologically relevant concentrations together with excellent accessibility to the hotspot region, planarity and biocompatibility. Hence, after validating our methodology using model lipid membranes (Chapters 3, 4), we were eager to exploit its high potential to investigate for the first time the dynamic nanoscopic organization of lipid rafts in the plasma membrane of living cells at a spatial resolution of 10 nm. In this chapter we report on the application of this type of nano-antennas with gap sizes of 10 and 35 nm to investigate the diffusion dynamics of phosphoethanolamine (PE) and sphingomyelin (SM) on the plasma membrane of living Chinese hamster ovary (CHO) cells. Compared to earlier works using confocal FCS,[36,40,41] nano-aperture FCS,[87–90,92,93] or STED-FCS,[60,62–64] our study is the first to breach into the sub-30 nm spatial scale on living cell membranes. Together with cholesterol depletion experiments, we provide compelling evidence for the existence of short-lived cholesterol-induced ~10 nm nanodomain partitioning in plasma membranes. We further discuss the impact of our results in the context of lipid rafts.

5.2 Methods

5.2.1 Fabrication of planar nano-antenna arrays

Large-scale planar nano-antenna arrays were fabricated by our collaborators of the group of Prof. J. Brugger at EPFL, Lausanne as part of a European collaboration. The approach combines electron beam lithography (EBL) with planarization, etch back, and template stripping as explained in detail in Chapter 2. This fabrication procedure makes that the narrowest gap region, where confinement is highest, becomes readily accessible to the sample. Moreover, the planarization step renders the antenna perfectly suitable for membrane studies as it precludes the occurrence of curvature effects that might influence the dynamics of molecules within the bilayer (for more details see Chapter 2).

5.2.2 Cell culture, Atto647N-labeling and cholesterol depletion of CHO cells

CHO cells were seeded on a coverslip containing planar nano-antennas with surface nanogaps and were allowed to grow and spontaneously attach at 37 °C in a controlled atmosphere with 5 % of CO_2 for nearly 48 h. Lipid conjugates were

separately prepared by labeling 1,2-dipalmitoyl-sn-glycero-3-phosphoethanolamine (DPPE) and sphingomyelin (SM) with the organic dye Atto647N (*Invitrogen*) as described in Ref. 60. Just before the fluorescence measurements, the fluorescent lipid analogues dissolved in the Ham's F12 nutrient medium were incorporated into the plasma membrane of the living CHO cells for an incubation period of three minutes at room temperature. Next, the stained cells seeded on the nano-antenna platform were carefully rinsed with medium to remove excess dye molecules and placed onto the piezo stage in the confocal setup. For cholesterol depletion experiments, the CHO cells were incubated in serum-free buffer with 10 mM methyl-β-cyclodextrin (MCD) for 30 min at 37 °C, and then the fluorescent labeling was carried out as previously described. The initial staining concentration for all experiments was targeted for ~ 300 nM of Atto647N. Note that we carried out the FCS experiments on tens of antennas per platform within ~ 30 minutes after completing the live-cell staining to avoid artifacts due to dye internalization. We estimate that the density of fluorescent lipids for the antenna experiments is on the order of 20–80 probes per μm^2 (based on the number of detected fluorescence bursts and the FCS amplitude of the data shown in the Results section).

5.2.3 Experimental setup for fluorescence spectroscopy

The experiments were performed on the same setup as explained in detail in Chapter 3. All fluorescence measurements were performed by illuminating the sample at an excitation power density of ~2–3 kW/cm^2. The measurements were acquired for a typical run time of 50 s, and the correlation amplitudes were computed for ~20 s windows with the commercial software package *SymPhoTime 64*. Cells were cultured on different antenna samples, each sample containing different gap sizes.

5.2.4 Fluorescence burst analysis

Single-molecule fluorescence time traces were acquired in the tagged time-resolved (TTTR) mode (recording each event at its arrival time) with 4 ps temporal resolution. Fluorescence burst analysis was carried out with a likelihood-based algorithm to test the null hypothesis (no burst, recording compatible with background noise) against the hypothesis that a single molecule burst arises as a consequence of a molecule crossing the excitation area. Probabilities associated with false positive and missing event errors were both set to 10^{-3}.[204]

5.2.5 Fluorescence Correlation Spectroscopy (FCS)

FCS curves were generated as explained in detail in Chapter 2. For the living cell experiments reported in this chapter, we have taken into account that molecular diffusion in living cells might deviate from purely Brownian motion and thus consider the possibility of anomalous diffusion. In these conditions, the temporal correlation $\boldsymbol{G(\tau)}$ of the fluorescence intensity $\boldsymbol{F(t)}$ can be written as[37]

$$\boldsymbol{G(\tau) = \sum_{i}^{n_{diff}} \frac{A_i}{1 + \left(\tau/\tau_{diff,i}\right)^{\alpha_i}}} \quad \textbf{Eq. 5-1}$$

where $\boldsymbol{\tau_{diff,i}}$ is the average residence time of the ith diffusing behavior, $\boldsymbol{A_i}$ denotes the respective amplitude contribution, and $\boldsymbol{\alpha_i}$ is the anomaly parameter of the same.[64] Note that $\boldsymbol{\alpha}$ = 1 corresponds to Brownian, free diffusion and $\boldsymbol{\alpha}$ values < 1 correspond to anomalous subdiffusion.[142]

To fit the obtained autocorrelation curves obtained on this type of planar nanogap antennas, we take advantage of the key feature in FCS, namely that the molecules contribute to the correlation amplitude in proportion to the square of their fluorescence brightness. Hence the signal from molecules in the nanogap experiencing maximum enhancement will have a dominating contribution to the FCS curves.[109] We find that the FCS curves recorded with a nanoscopic illumination can be fitted with a model assuming two different diffusion species (i.e., $\boldsymbol{n_{diff} = 2}$), accounting for the (shorter) diffusion of fluorescent probes transiting the antenna hotspot in the nanogap and a second, longer diffusion time resulting from the background contribution in the nano-aperture region. For the experiments of FCS in living cells of this chapter, we account for diffusion probably deviating from free Brownian by leaving the anomaly parameter $\boldsymbol{\alpha}$ free for the first component fitting the gap distribution.

To define the probe areas used in the FCS diffusion laws, we use the product of the gap size (measured by TEM) with the full-width at half-maximum of the intensity profile along the direction perpendicular to the antenna main axis (computed by FDTD), following a calibration for model lipid membranes discussed in Chapter 3, Therefore, 10 and 35 nm gap sizes are associated respectively with 300 and 1250 nm^2 probe areas.

5.3 Results

Figure 5-1 a, b depicts the strategy chosen for the living cell experiments using nanogap antenna arrays as substrates for cell seeding. We focus the laser light (λ = 640 nm) onto individual antennas using a high-NA water immersion objective. Throughout this study, the linear polarization of the laser beam is set parallel to the antenna main axis so as to excite the nanometric hotspot on the surface of the nanogap region which is in direct contact with the adhered plasma membranes of living CHO cells. Importantly, the planarization strategy avoids possible curvature induced effects on the cell membrane.

CHO cells were incubated on the nano-antennas at 37 °C for nearly 48 hours prior to the experiments to allow them to freely grow and adhere onto the antenna platform. Lipid analogues (either PE- or SM complexes) were fluorescently labeled with the lipophilic organic dye Atto647N (see the Methods Section 5.2 of this chapter for more details). We choose Atto647N as fluorescent dye since it has an excellent overlap with the antenna's main plasmonic resonance guaranteeing maximum fluorescence enhancement in the nanogap. A representative confocal image of the morphology of the CHO cells adhered on a glass coverslip taken after the incorporation of the fluorescent lipid analogs is shown in Figure 5-1 b.

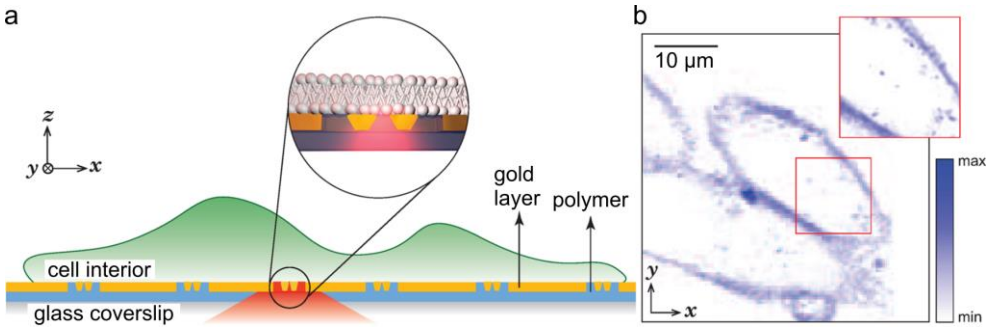

Figure 5-1. ***Planar nano-antennas for investigating membrane dynamics in living CHO cells.*** *(a) Schematics of our experimental approach with living cells seeded on top of the nano-antenna array. (b) Confocal image of adherent living CHO cells after labeling the SM lipid analog with Atto647N.*

Figure 5-2 a, b shows representative single-molecule fluorescence time traces for PE and SM in the confocal and in the nano-antenna configuration. The resolution given by the diffraction limited spot in the confocal scheme does not allow us to resolve heterogeneities that may occur at the sub-200 nm spatial scale, and as a result, the time traces for both PE and SM appear indistinguishable. In contrast, the

highly confined excitation hotspot originating from the 10 nm gap antenna clearly reveals differences in the characteristic diffusion dynamics for PE and SM. As shown in Figure 5-2 b, PE displays sharp peaks in the fluorescence time trace as a result of the sub-diffraction excitation hotspot created by the planar nanogap antenna. Unlike PE, the signature of SM is discernibly different at the nanoscale: the short bursts (a hallmark of free diffusion in ultrasmall detection areas) are accompanied by high intensity bursts of significantly longer durations. This is a direct indication that the nanoscopic diffusion of SM on the cell membrane is deviating from free Brownian diffusion as compared to larger macroscopic scales.

To provide more quantitative information about the fluorescence time traces, we performed a fluorescence burst analysis to represent the distributions of burst duration versus burst intensity. From Ref. 104,204 we adapted and implemented in *Matlab* a burst analysis based on a likelihood algorithm to find single molecule bursts stemming from diffusion across our excitation area against the fluorescence background of 20-30 counts/ms which we determined empirically (see Methods Section 5.2). Figure 5-2 c shows the results for both PE and SM for the 10 nm nanogap antenna compared to the confocal configuration. The scatter plots for PE and SM in the confocal configuration (black crosses) show no visible differences with burst durations in the range 1–100 ms and intensities around 20–30 counts/ms. However, in stark contrast, the distributions obtained on the nano-antennas show clear differences between PE and SM. Diffusion events in sub-millisecond time scales are notably observed with the nano-antennas exhibiting burst durations as short as 10 µs. Such short events are more than two orders of magnitude faster than in the case of the confocal reference. Regarding the diffusion dynamics for PE (red dots) probed with the nanogap antennas a general trend can be deduced; namely, brighter events arise at shorter time scales. These can be understood as the detection of a "best burst event" directly resulting as a consequence of an individual molecule diffusing through the hotspot in the optimal position and orientation for maximum enhancement. The tighter the excitation beam confinement, the higher is the local intensity which leads to higher fluorescence intensity and shorter burst duration. Thus, we relate the events with burst durations below 1 ms to the trajectories occurring within the nanogap region.[104] In the case of PE, the bursts with durations above 1 ms feature a lower intensity in the range of 20–70 counts/ms, which is only slightly increased as compared to the confocal level. We assign these longer burst duration events to the residual excitation of diffusing molecules within the larger 300 × 140 nm^2 box

aperture region where the electromagnetic field intensity enhancement is negligible yielding similar intensity values and durations as the confocal reference.

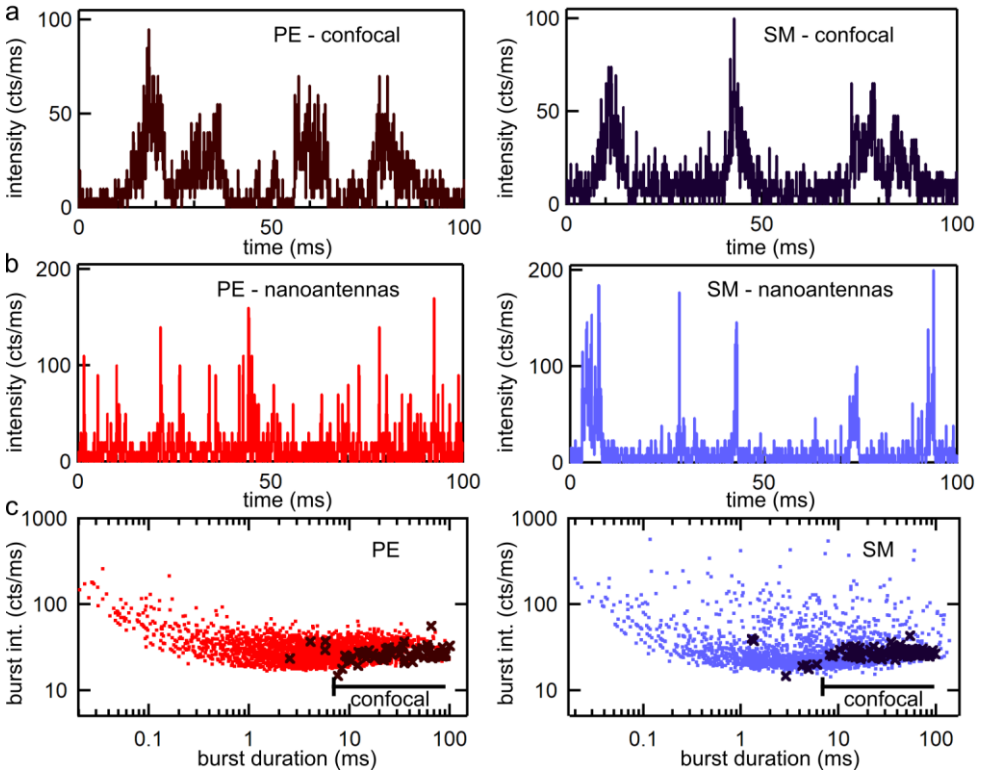

Figure 5-2. ***Single molecule time traces in living CHO cells.*** *(a, b) Fluorescence intensity time traces for the lipid analogs for phospoethanolamine (PE, left) and sphingomyelin (SM, right) labeled with Atto647N monitored in a confocal configuration (a) and on a planar nanogap antenna of 10 nm size (b). The binning time is 0.1 ms for all traces. (c) Burst intensity vs. burst duration obtained from multiple fluorescence intensity time traces for PE (left) and SM (right). Short (sub-ms) single molecule events are observed when probing on the nano-antenna platform (color dots) in comparison to predominantly longer events obtained with confocal illumination (dark crosses).*

In contrast to PE, SM probed with the nano-antenna arrays shows a significantly broader distribution of burst lengths against peak burst intensities (Figure 5-2 c). High intensities are observed for burst durations below and above 1 ms. Since these events were not observed for PE, we relate their occurrence to nanoscopic heterogeneities such as transient molecular complexes on the cell membrane hindering the diffusion of SM.

To support this conclusion, we perturbed the cholesterol composition in the cell membrane with methyl-β-cyclodextrin (MCD), as cholesterol is expected to play a significant role in the formation and stability of the lipid nanodomains. The result of the burst analysis for SM after MCD treatment recovers a distribution which closely resembles the one for PE (Figure 5-3). In other words, the intense bursts of duration between 0.1 and 10 ms disappear after cholesterol depletion, consistent with the loss of nanodomains. Altogether, the results from the fluorescence burst analysis demonstrate the benefits of planar nanogap antennas to explore the nanoscopic organization of lipids in live cell membranes. Clear differences between PE and SM diffusion dynamics are unveiled that otherwise would remain hidden in confocal measurements.

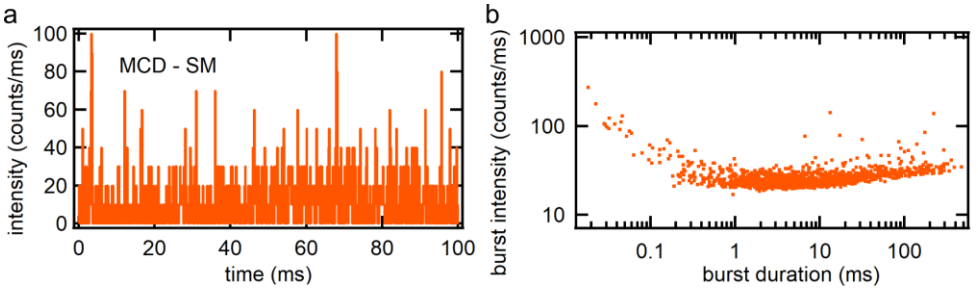

Figure 5-3. ***Single-molecule traces in living cells after cholesterol depletion.*** *(a) A representative single-molecule intensity time trace of the fluorescent analog for SM labeled with Atto647N after cholesterol depletion (MCD-SM) measured on a planar nanogap antenna of 10 nm size with a binning time of 0.1 ms. (b) Burst intensity vs. burst duration obtained from multiple fluorescence intensity time traces for SM after cholesterol depletion.*

To further support these results, we performed FCS analysis. FCS records the fluorescence intensity fluctuations as the fluorophores transit through the detection spot. These fluctuations are analyzed by computing the temporal autocorrelation function, averaging over thousands of single molecule diffusion events. As anticipated, autocorrelation curves of PE and SM taken under confocal illumination yielded comparable diffusion times of 24 ± 4 ms (PE) and 30 ± 4 ms (SM), respectively (Figure 5-4). These results further justify the need of reducing the illumination volume by means of photonic antennas.

We used two different gap sizes (10 and 35 nm) to quantify the lipid dynamics for increasing detection areas in cell membranes with single-molecule sensitivity. Moreover, we normalized the correlation curves of data from individual traces in order to compare the two different gap sizes of the nano-antennas with the confocal

reference. Each of these traces is taken on an individual nano-antenna consistently representing many antennas probed of the same size.

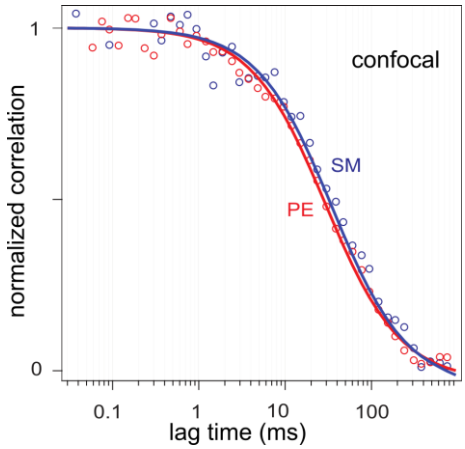

Figure 5-4. ***Confocal FCS for SM and PE on living cells.*** *The normalized FCS curves for the fluorescent analogs for PE and SM labeled with Atto647N recorded on the confocal setup show only minor differences.*

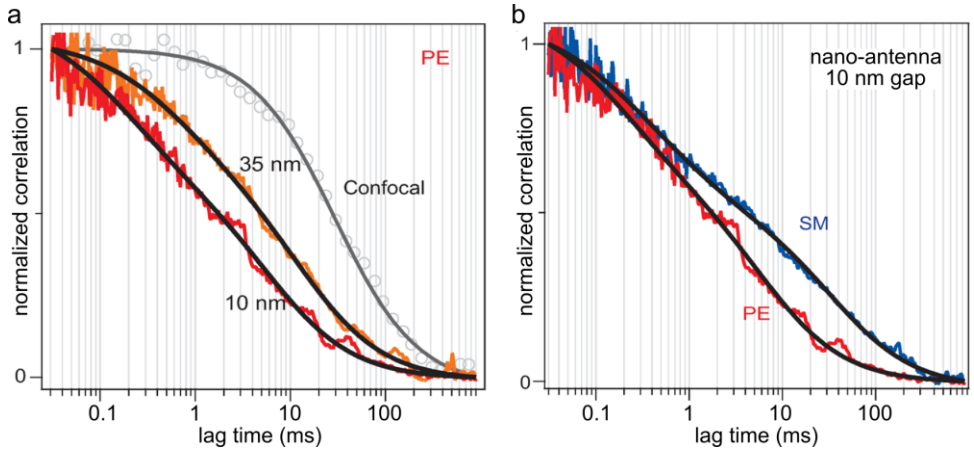

Figure 5-5. ***Nano-antenna FCS for PE and SM on living cell membranes.*** *(a) Normalized fluorescence correlation curve for Atto647N labeled PE lipid analog probed with nano-antennas of varying gap size. The color lines are experimental data, and the black curves are numerical fits. Each FCS trace is a representative example taken on an individual nano-antenna. The diffraction-limited confocal measurements are shown in gray for direct comparison. (b) Comparison of FCS curves for PE and SM for a 10 nm gap antenna. Unlike the confocal reference, the nano-antenna reveals clear differences between the dynamics of PE and SM at the nanoscale.*

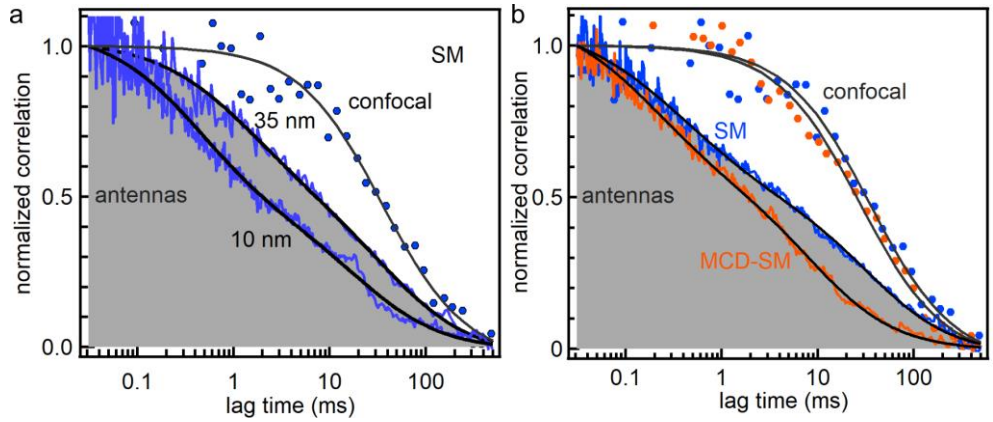

Figure 5-6. ***Nano-antenna FCS for SM before and after SM depletion on living cell membranes.*** *(a) Normalized correlation curves for Atto647N labeled SM lipid analogs probed with nano-antennas of varying gap size in comparison to the confocal illumination spot. The color lines/circles are experimental FCS data, and the black curves are numerical fits. The grey shaded area indicates the correlation curves and fits obtained on nano-antennas. Each FCS trace is a representative example on an individual nano-antenna. (b) FCS curves of SM before (blue) and after (orange) cholesterol depletion. The SM diffusion dynamics is significantly faster when probing on a representative nano-antenna of 10 nm gap size which is not apparent in the confocal configuration.*

We use a two-component model to fit the FCS data (**Eq. 5-1**) in order to account for the fluorescence contributions stemming from the nanogap and from the surrounding aperture area (for details refer to the Methods Section 5.2). We have been successfully applying this fitting approach in solution and on model lipid membranes. (compare to Chapters 2,3,4). The complete results and values for the FCS fits are detailed in Table 5-1. The differences between PE and SM diffusion dynamics are highlighted in Figure 5-5 b where a direct comparison of the FCS data for the 10 nm gap antenna is shown for the two different fluorescent lipid analogs of PE and SM. Contrarily to the confocal case (Figure 5-4) where the diffusion times of PE and SM are comparable, the difference in diffusion times between the two lipids becomes more prominent at the nanoscale. For instance, for a 10 nm gap antenna, PE exhibits a diffusion time of 0.25 ±0.06 ms, whereas the value for SM is 0.35 ± 0.04 ms (Figure 5-5 b). Moreover, after MCD treatment, the diffusion dynamics for cholesterol-depleted SM closely resembles that of PE with a diffusion time of 0.19 ± 0.03 ms (Figure 5-6 b). These FCS results at the nanoscale confirm the presence of cholesterol-enriched nanodomains hindering the diffusion of SM, in agreement with the results found for the fluorescence burst analysis. In addition, we retrieved an anomaly value $\alpha < 1$, indicating a deviation from Brownian

diffusion, for which α = 1. Interestingly, the anomaly value α for SM depended on the probed area, deviating from unity as the illumination area reduced, from α ~ 0.85 (for the 35 nm gap antenna) to α ~ 0.65 (for the 10 nm gap antenna), which is fully consistent with hindered diffusion (refer to Table 5-1).

Table 5-1. *Obtained parameters of the fitted autocorrelation curves for representative nano-antennas of different gap sizes (indicated in parentheses in the Table). The results are shown for fluorescence experiments on PE, SM and MCD-SM based on a two-component diffusion model with the anomaly parameter α left free for the first component.*

	PE (10 nm)		**PE (35 nm)**			
component	**1st**	**2nd**	**1st**		**2nd**	
diffusion time	**(0.25±0.06) ms**	**8 ms**	**(0.75±0.15) ms**		**16 ms**	
anomaly (α)	**0.85**	**1**	**0.8**		**1**	
corr. amplitude (G_{00} in %)	**(53±4)**	**(47±5)**	**(50±3)**		**(50±5)**	
	SM (10 nm)		**MCD-SM (10 nm)**		**SM (35 nm)**	
component	**1st**	**2nd**	**1st**	**2nd**	**1st**	**2nd**
diffusion time	**(0.35±0.04) ms**	**38 ms**	**(0.19±0.03) ms**	**10 ms**	**(1.4±0.2) ms**	**45 ms**
anomaly (α)	**0.7**	**1**	**0.85**	**1**	**0.85**	**1**
corr. amplitude (G_{00} in %)	**(59±4)**	**(41±5)**	**(53±4)**	**(47±4)**	**(55±5)**	**(45±6)**

In contrast, the α values were significantly larger and closer to unity for the cases of PE and SM after MCD treatment (α ~ 0.85) and did not depend on the probe area, as expected for Brownian, unhindered diffusion.

To further analyze and exploit the FCS data, we take advantage of the large number of planar nano-antennas with controlled gaps to carry out an FCS analysis over 60 different antennas and cells. To obtain a hint of the characteristic diffusion behavior of PE and SM, we follow the approach of the FCS diffusion laws. As introduced in Chapter 1, a FCS diffusion law plot represents the diffusion time versus the detection area. Extrapolation of the experimental curve to the intercept with the time axis provides information on the type of diffusion exhibited by the (probing) molecule. i.e., free diffusion is characterized by a linear curve crossing the origin (0,0), while hindered diffusion due to the occurrence of nanodomains leads to a positive intercept on the time axis.[41,90] We already applied this approach for studies on model lipid membranes (Chapter 3) using nano-antennas of different gap sizes and extended the FCS diffusion law plot to the nanoscale. The nano-antenna detection area for the 10 and 35 nm gap antennas correspond, respectively, to 300 nm^2 and 1250 nm^2 illumination areas. As the diffusion time proportionally scales with the detection area, the diffusion coefficient *D* is retrieved from the slope of the linear fit, matching the measured transient diffusion times obtained from the FCS curves versus the effective detection areas according to the relation:

$$\boldsymbol{\tau(\omega^2) = \tau_0 + \omega^2/(4 \times D)} \quad \textbf{Eq. 5-2}$$

The characteristic diffusion times versus the two gap areas are summarized for PE in Figure 5-7 a, and in Figure 5-7 b, c for SM and SM after cholesterol depletion (MCD-SM). Note that in Figure 5-7 b we also include the results obtained from diffraction-limited confocal measurements.

From these graphs we derive the following three values plotted in Figure 5-7 d-f: the diffusion coefficient (from the slope), the time axis y-intercept (by extrapolating the linear fit for vanishing probe area) and the normalized spread in the data points (defined as the width of upper and lower quartiles divided by the median value). The diffusion coefficients derived from nano-antenna measurements are D_{PE} = 0.44 ± 0.07 $\mu m^2/s$, D_{SM} = 0.38 ± 0.19 $\mu m^2/s$, and $D_{MCD\text{-}SM}$ = 0.46 ± 0.07 $\mu m^2/s$ (Figure 5-7 d), and they are consistent with the confocal measurements and values reported independently using STED-FCS.[64] These coefficients represent the diffusion speed

in the lipidic region between the nanodomains, with an additional contribution from diffusion within the nanodomains and diffusion of the domains themselves.

Extrapolating the fits in Figure 5-7 a-c toward diminishing probe area leads to the intercepts with the time axis as summarized in Figure 5-7 e. The almost zero intercept hitting the origin observed for PE confirms the expected free Brownian motion diffusion mode. In stark contrast, SM features a positive y-intercept of ~ 110 ± 80 µs, which highlights a significant deviation from free Brownian diffusion and the occurrence of nanoscopic domains hindering SM diffusion. The depletion of cholesterol results in SM diffusion with a close-to-zero time intercept (~20 ± 15 µs), demonstrating the crucial role of cholesterol establishing the nanodomains and hindering SM diffusion. Such small nanoscale heterogeneities have never been detected so far with confocal microscopy, although STED-FCS down to a 1000 nm^2 detection area could infer their occurrence.[64] Our results are fully aligned with these previous findings and importantly, we further reduce the detection areas down to 300 nm^2.

Lastly, we take a closer look at the statistical dispersion of the diffusion times for each gap area and introduce the normalized data spread as the width from upper to lower quartiles divided by the median value (Figure 5-7 f). The spread in diffusion times for PE and SM after the MCD treatment remains under 25 % and can be partially assigned to nanometer variations of the gap size between nano-antennas. These variations stem from inaccuracies in the nanofabrication process, as a consequence of the finite grain size of gold and/or scattering of electrons used during the electron beam lithography. In contrast to PE and MCD-SM, the data for SM feature a significantly higher statistical dispersion around 50 %, which cannot be related solely to dispersion in the nano-antenna sample, but instead it results from large variations in the SM diffusion behavior, as already noted for the fluorescence burst analysis (Figure 5-2 c). These results are fully consistent with the presence of cholesterol-enriched nanodomains affecting SM diffusion.

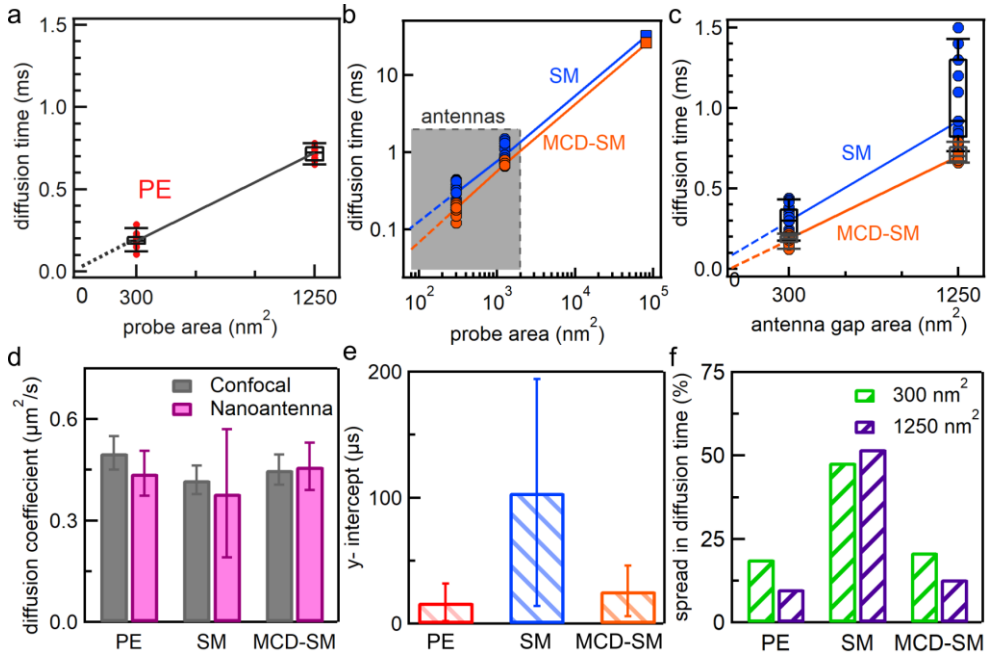

Figure 5-7. ***Characteristic diffusion dynamics of membrane lipids probed with nanometric antenna hotspots in comparison to the confocal configuration.*** *The characteristic diffusion times obtained by fits to the FCS data (for 60 different nano-antennas) are plotted as a function of the probe area for PE (a), SM and SM after MCD treatment resulting in cholesterol depletion (b and magnified on the nano-antenna probe area in c). The solid lines are linear fits through the median values. In the case of free diffusion, the origin (0, 0) is aligned with the expected line, while a positive intercept at the y-axis hints toward hindered diffusion due to emerging nanodomains. Diffusion coefficients are shown in (d) which were computed from the slopes of the linear fits in a-c. PE and MCD-SM exhibit a near-zero y-intercept consistent with free diffusion, while a significant y-intercept indicates SM diffusion constrained by nanodomains (e). The normalized spread in diffusion times (width of upper and lower quartiles/median) are depicted in (f) for the three conditions on the two different nano-antenna gap sizes.*

5.4 Discussion

Altogether, our results provide compelling evidence for the existence of highly transient and fluctuating nanoscale assemblies of sterol and sphingolipids in living cell membranes. Our experimental observations stand in excellent agreement with the notion that, without stabilizing proteins, lipid rafts can be viewed as intrinsic nanoscale membrane heterogeneities that are small and highly transient.[2,9,13,45] To estimate the characteristic trapping time of SM within nanodomains, we rely on the

y-intercepts shown in Figure 5-7 b ,e, and also consider the free diffusion of the dye in solution. As shown by Ruprecht and coworkers,[42] in the case of immobile nanodomains and an exponential distribution of trapping and diffusion times, the time offset t_0 is the product of the trapping time τ_{trap} with the fraction β of trapped fluorophores: $t_0 = \beta \times \tau_{trap.}$ Thus, the effective diffusion coefficient D_{eff} measured from the FCS diffusion laws can be expressed $D_{eff} = (1-\beta) \times D_{free}$ where D_{free} is the diffusion coefficient for the free dye. Using the experimental values measured for SM before and after MCD treatment (and substituting in the previous equations $D_{SM} = D_{eff}$ and $D_{MCD\text{-}SM} = D_{free}$), we obtain β=0.17 and τ_{trap} =0.6 ms. A slightly modified set of equations allows us to take into account also the mobility of the nanodomains.[42] Assuming that the diffusion coefficient for the nanodomains is ten times slower than for free diffusion $D_{trap} = D_{free}/10$, we obtain slightly modified values for the trapped fraction and trapping time, i.e., β =0.19 and $\tau_{trap.}$ =0.9 ms. These results stand in good agreement with the 1-2 ms trapping time inferred from STED-FCS using an anomalous diffusion fitting.[64] The typical size of the nanodomains could in principle also be deduced from the FCS diffusion laws which should feature a characteristic transition from confined to normal diffusion.[41,90] As we do not observe this characteristic transition in our data, we conclude that the typical size of the nanodomains is smaller than the smallest gap size of our nano-antenna, that is 10 nm.

Our results stand in good agreement with the predictions from stochastic models[161] and recent high-speed interferometric scattering (iSCAT) measurements on mimetic lipid bilayers containing cholesterol.[76] Our nanogap antenna approach is straightforward to implement on any confocal microscope equipped for FCS, and does not require the addition of supplementary illumination schemes, as compared for instance to STED. As additional advantage, the excellent planarity of the surface rules out any artifact potentially induced by the curvature of the cell membrane.[92] We believe that these advantages and the excellent spatiotemporal resolution largely compensate for the need for nanofabrication and the more complex FCS fitting procedure.

5.5 Conclusion

In conclusion, we have demonstrated the promising approach of exploiting planar optical nano-antennas with accessible surface nanogaps to investigate the nanoscale architecture of living cell membranes. The key strengths of our approach rely on the 10 nm spatial resolution combined with a microsecond time resolution

on a nearly perfectly flat substrate compatible with live cell culturing. The single-molecule data on nano-antennas reveal striking differences between PE and SM diffusion dynamics that remain hidden in confocal measurements. Fluorescence burst and correlation spectroscopy analysis for PE are consistent with a free Brownian diffusion model. In contrast, the diffusion dynamics of SM at the nanoscale show heterogeneities in both time and space which are dependent on cholesterol. Indeed, the removal of cholesterol leads to a recovery of free Brownian diffusion for SM, consistent with the loss of nanodomains.

Our results are consistent with the existence of dynamic nanodomains on the plasma membranes of living cells of ~10 nm diameter which is comparable to our measurement gap size. The corresponding transient trapping times are short of about ~0.9 ms. We believe that the combination of photonic nano-antennas with fluorescence microscopy has a high potential to investigate the dynamics and interactions of raft-associated proteins and their recruitment into molecular complexes on the plasma membrane of living cells. The proposed technique is fully biocompatible and thus provides ample opportunities for biophysics and live cell research with single-molecule sensitivity at nanometric and (sub)microsecond spatiotemporal resolution, far beyond the diffraction limit of light. These studies will ultimately improve our understanding of the cell membrane organization and its link to the cell's function.

The envisioned next steps in living cells will explore the native influence of the adjacent inner and outer environment (the cortical actin cytoskeleton and the glycan network, respectively) on templating the dynamic nanoscale organization of the plasma membrane. Reaching these goals will also require pushing the nano-antenna technology even further, to narrow the antenna gap, sharpen the metal edges, improve the overall reproducibility over the full antenna arrays and enabling multiplexed, parallel detection from hundreds of antennas simultaneously. Additional challenges comprise the development of antennas with broadband resonance enabling multi-color fluorescence detection.

In Chapter 6 we focus on one of these challenges and tackle the implementation of excitation and detection schemes for multiplexed FCS recording at the nanoscale by means of nano-antenna arrays.

6 Multiplexed FCS at the nanoscale using planar photonic antennas

The spatiotemporal organization of lipids, proteins and other molecular players in biological membranes is highly heterogeneous at multiple spatial and temporal scales and is essential for the regulation of biological processes. Fluorescence correlation spectroscopy (FCS) is a powerful single-molecule sensitive tool to study dynamic molecular processes with very high temporal resolution. The advent of fast and sensitive imaging cameras has paved the way for Imaging FCS, a technique that takes advantage of the parallel acquisition of fluorescence from addressable areas on the camera. This renders it possible to generate spatial maps of mobility and interactions in living cells from a single measurement.

Throughout the different chapters of this dissertation we have described different applications of planar plasmonic nano-antenna arrays combined with FCS to address the nanoscale complexity of biological membranes, both on mimetic systems as well as on living cells. Nevertheless, despite the availability of large arrays composed of thousands of nanogap antennas in a single substrate, so far, we have performed experiments in a serial fashion, i.e., addressing one antenna at a time.

In this chapter, we report on the implementation of widefield illumination together with sCMOS camera detection to demonstrate the multiplexing capabilities of planar plasmonic nano-antenna arrays of different nanogap sizes (10-45 nm). First, using far-red fluorescent beads we showcase the performance of the nanogap antenna arrays for multiplexed FCS at the nanoscale. Second, we have extended this approach to demonstrate simultaneous parallel detection of protein diffusion in living cell membranes

on over 50 antennas. Our approach constitutes a leap forward towards the broad application of parallelized antennas for simultaneous detection of hundreds of dynamic events in living cells at the nanoscale.

6.1 Introduction

Our understanding of the living cell membrane and its spatiotemporal organization has evolved from the initial proposal of a fluid mosaic model to an active composite model.[4,205] Within the plane of the membrane bilayer, its constituents are heterogeneously organized in space and time. Furthermore, it appears that the cell membrane is dynamically remodeling and interacting with cytoplasmic and extracellular components on either side of the membrane bilayer from the nano- to the mesoscale. Much of the current knowledge generated over the last 20 years on the dynamic organization of the plasma membrane has resulted from the development and application of highly sensitive optical techniques that provide either increased temporal or spatial resolution.

One of such optical techniques is Fluorescence correlation spectroscopy (FCS). FCS is a powerful tool to assess the dynamic diffusion behavior of molecules in vivo, as explained in detail in Chapter 2. In a standard FCS experiment, intensity fluctuations arising from the passage of labeled molecules through the illumination volume are recorded over time. By calculating the corresponding autocorrelation function, FCS provides quantitative information on the molecular concentration and its characteristic diffusion time. However, such experiments are typically performed with point detectors, thus a single (diffraction-limited) spot is probed at a time. Therefore, spatial variations of membrane constituents over the living cell surface are challenging to investigate, despite their crucial role in cell signaling and trafficking.

Various technical approaches have been developed to allow for multiplexed FCS experiments, probing multiple locations simultaneously. Electron-multiplying charge-coupled device (EMCCD) and scientific complementary metal-oxide-semiconductor (sCMOS) cameras possess millions of pixels, which could be implemented, in principle, as area detectors. But only recently, EMCCD and sCMOS cameras became fast and sensitive enough to enable time-resolved spectroscopy on a large number of pixels in parallel.[206] An alternative implementation includes the use of single photon avalanche photodiode (SPAD) arrays working as imagers, with the advantage of increased temporal resolution and zero readout noise thanks to their inherently digital nature. The drawbacks are lower overall sensitivity and a challenging technical implementation relying on microlenses and FPGA-based readout.[207]

A pioneering approach was to use an EMCCD camera in conjunction with a stationary spinning disk confocal microscope to measure tens to hundreds of spots in the living cells with conventional chemical or genetic fluorophores.[208,209] The combination of a fast and single-molecule sensitive camera with single-plane illumination (SPIM) or total internal inflection fluorescence (TIRF) configuration has paved the way for imaging FCS (imFCS). ImFCS possesses remarkable statistical power resulting from hundreds to thousands of FCS measurements from a single acquisition.[206] However, these multiplexed capabilities are limited in terms of spatial resolution, due to their implementations based on diffraction-limited optics.

The arrival of super-resolution techniques has revolutionized the field of fluorescence microscopy and made it possible to elucidate the nanoscale organization of different organelles and the cell membrane on intact cells.[4,46,54,57,64,66,210,211] Nevertheless, except from stimulated emission depletion (STED) microscopy, most single-molecule localization-based super-resolution methods lack the required temporal resolution to visualize dynamic processes in living cells. STED is amenable to a straightforward FCS implementation since the FCS technique relies on a point detector, generally a SPAD. Yet, extension of multiplexed FCS by means of STED remains challenging. One approach to be highlighted is scanning STED-FCS (sSTED-FCS) which revealed spatiotemporal heterogeneities of lipid interactions in living cells with down to ~ 30nm resolution.[63]

Metallic nanostructures are able to highly confine impinging light into nanometric volumes and to provide high fluorescent enhancement.[95] By the use of electron-beam lithography (EBL), such metallic nano-antennas can be readily fabricated at a large scale.[203] However, since FCS commonly requires the use of fast detectors (such as SPADs), fluorescence detection is performed on individual antennas in a serial fashion. If one abandons the demand for high temporal resolution, then antenna arrays can be straightforwardly combined with widefield illumination and detection. Indeed, such an approach made it possible to resolve the interactions between individual nanorods and freely diffusing fluorophores in solution in a multiplexed fashion from ensemble measurements.[212]

In this chapter we report on the implementation of multiplexed FCS at the nanoscale by means of nanogap antenna arrays combined with sCMOS camera detection. We performed benchmarking experiments with far-red fluorescent beads freely diffusing in 1.6 M sucrose solution. We quantified the ensemble photon

statistics from a single acquisition measurement on 225 nano-antennas simultaneously. Moreover, we retrieved single burst information from the multiplexed measurements and estimated the fluorescent enhancement provided by the nano-antennas. We then validated our approach for multiplexed FCS on diffusing beads in sucrose solution acquired on 50 nano-antennas in a single measurement. Finally, we performed experiments on living cells using our multiplexed approach and revealed heterogeneous diffusion of fluorescent proteins on living cell membranes. Importantly, our multiplexed nano-antenna approach allowed us to resolve ligand diffusion either freely diffusing off the cell in solution or transiently binding to cell membrane receptors.

6.2 Methods

6.2.1 Fabrication of planar nano-antenna arrays

Large-scale planar gold nano-antenna arrays with surface nanogaps were fabricated by our collaborators of the group of Prof. J. Brugger at EPFL, Lausanne as part of a European collaboration. The multistep process to nanofabricate the nano-antenna arrays is based on electron beam lithography (EBL), planarization, etch back, and template stripping (for details please refer to Chapter 2). The design of the nanogap antenna arrays consists of a gold half-sphere dimer (diameter 80 nm) of gap sizes between 10-45 nm centered in a nano-aperture of 140 × 300 μm^2 and thousands of these antennas-in-box were aligned with an antenna-to-antenna spacing of 4 µm on a single substrate. This nanofabrication method is fully scalable and shows excellent planarity. The antenna's plasmonic resonance lies at ~ 697 nm driving the strong optical near-field enhancement and is efficiently excited by far-red laser illumination at ~ 640 nm. Before each experiment we cleaned the antenna substrate carefully by ethanol and MilliQ water rinsing and N_2 drying. Just prior to the experiment the cleaned antenna array substrates were treated with 3 min/5 min UV/Ozone illumination to render the gold surface hydrophilic.

6.2.2 Cell culturing and labeling

Folate-receptor-expressing human gastric cell line AGS (FRAGS)[5] were maintained in HF12 medium containing 50 mg/ml Hygromycin. Prior to the experiment cells were detached from the flask using TrypLE Express (*ThermoFisher*), collected and washed with M1 (150 mM NaCl, 20 mM HEPES, 5 mM KCl, 1 mM $CaCl_2$ and 1 mM $MgCl_2$, pH = 7.4) buffer. Next, the cells were allowed to attach freely to a freshly

cleaned antenna substrate in M1-Gl buffer (M1 buffer containing 2 mg/ml glucose) for 2 hours at 37 °C.

Drosophila melanogaster flies were maintained at 22 °C in glass vials containing standard fly media. Collagen-GAL4 was used to drive expression of UAS-GFP-GPI (gift from S. Eaton) in the hemocytes of the larvae. Hemocytes from larvae were obtained as described previously.[213] Briefly, 6 third-instar larvae were surface sterilized and hemolymph was collected by puncturing the integument using dissection forceps into 200 µL of M1-Gl at pH = 6.9 containing 1 mg/ml BSA. Next, the solution was gently placed on a freshly cleaned antenna substrate and the cells were allowed to adhere for 1 hour at 22 °C.

The GFP-GPIs on the attached *Drosophilia* hemocytes were labeled at saturating conditions with 200 nM *Abberior Star635* conjugated nt-GFP nanobodies. The Folate receptor GPIs on the attached FRAGS cells were labeled with 200 nM *Abberior Star635* conjugated Fab fragments against the Folate receptor (Mov19).

When required, FRAGS were transfected 12-16 hours prior to the experiment with the EYFP-adenosine A2b receptor (*Addgene* plasmid #37202) using the *FuGENE* transfection reagent (*Promega*). As before, the cells were plated on a freshly cleaned antenna substrate. Just prior to the experiments, the Bodipy-Neca (a fluorescent non-selective adenosine receptor analogue from *CellAura*) was incubated for 5 min at 37 °C at a concentration of 500 nM in M1-Gl buffer. All experiments on the antenna substrates were performed at room temperature.

6.2.3 Experimental setup for fluorescence spectroscopy measurements

All the experiments were carried out during a research stay in the group of Prof. S. Mayor at NCBS, Bangalore, India, and in collaboration with Dr. T. S. van Zanten. The fluorescence experiments were performed on a home-built setup built around a *Nikon Eclipse Ti* body. The laser beam from a 642 nm cw-laser (*SpectraPhysics Excelsior-640C*) was expanded and confined to provide a uniform beam waist of around 10 mm. After a half-waveplate for polarization control, and via a set of lenses, the beam was directed into the back of the *Nikon* body and focused on the backfocal plane of a CFI Apo TIRF 60×, 1.49 NA objective. The excitation was aligned in an epi-illumination configuration and the emission was collected via the same objective separated from the excitation using a quad-edge dichroic (*Semrock*) in combination with a quad-notch filter (*Semrock*). The emission was further filtered

through a 675/68 nm bandpass filter (*Semrock*) and finally directed onto a water-cooled *Prime 95B* sCMOS camera (1200 × 1200 pixels, *Photometrics*), which was set at Sensitivity mode. For inspection of YFP or GFP fluorescence, a 488 nm laser was used in conjunction with a 520/35 nm bandpass filter, with all the other components kept identical. To allow for fast recording, the sCMOS was connected using the data-cable connector and the *μManager* software (*v2.0 gamma*) was used for image acquisition. The planar nanogap antenna arrays were illuminated at 45-50 mW laserpower at the backfocal plane, corresponding to a power density at the sample plane of about 0.05 kW/cm^2. The wavelength of the excitation (642 nm) corresponds to the resonance of the nanogap antennas and the excitation polarization (2500:1) was adjusted using a half-wave plate. Directing the polarization perpendicular to the antenna dimer axis delocalizes the near-field away from the nanogap and the detection volume becomes diffraction-limited. This allowed for a direct comparison of the nanogap antenna effect. In addition, we also performed control experiments by using nano-aperture arrays (i.e., without containing the dimer antennas) that were fabricated on the same antenna substrates.

To benchmark our multiplexed nano-antenna FCS approach, we performed experiments on far-red fluorescent beads (*F8789, ThermoFisher*) in a 1.6 M sucrose solution in 20 mM Tris buffer at 0.2 % of its original concentration. We used a high sucrose concentration to slow-down the diffusion of the beads to about D ~ 1 μm^2/s. In addition, to minimize sticking of the beads onto the antennas we added a few drops of TWEEN-20 (*Sigma*) to the bead solution.

The multiplexed traces for the burst analysis on fluorescent beads in the 1.6 M sucrose solution were extracted from over 2000 frames at 5 ms integration time (at 10 frames per second) in a field of view allowing the measurement on 225 nano-antennas simultaneously (ROI of 570 × 570 pixels, pixel size of = 122 nm).

The multiplexed FCS traces were recorded from 50 antennas simultaneously using a ROI of 950 × 50 pixels for 24000 frames at 0.9 ms integration time (typically resulting in a 1043 frames per second recording).

6.2.4 Image analysis and data processing

The analysis was performed using *ImageJ* and *Matlab*. The first objective was to obtain an intensity time trace for each nano-antenna from the recorded camera frame set. To recover the (x,y) coordinates of the antenna positions, we generated

an averaged intensity image of the respective frame set by a maximum intensity projection in *ImageJ*. This projected image yielded bright spots indicative of the lateral antenna positions as well as an (uneven) background due to gold film reflection and other backscatter light contributions. Applying a Gaussian Blur filter of 30 pixels and subtracting this image from the maximum intensity projection image allowed for a background-free detection of the antenna positions using the "Find Maximum" function in *ImageJ*. The (x, y) positions were saved to a txt file and would serve as a read-in file for the subsequent *Matlab* analysis.

The image sequence was converted from ADU (arbitrary digital units) to photons by subtracting the dark image and dividing by the gain image: both were obtained from a separate camera calibration.[214] Next, in the *Matlab* analysis routine, each identified antenna position was widened into a circular ROI having a radius of two (for FCS traces) and three (for the burst analysis) pixels. The sum number of the photons within each ROI was recorded and assigned into the intensity time trace of the corresponding antenna. The measured background for each frame, as mentioned above, was subtracted from the raw signal. Aside from the expected single frame intensity peaks, some of the intensity traces contained bursts that lasted for several frames. As these most likely correspond to beads that have remained stuck onto the antenna, they were eliminated from further analysis. A burst stemming from a fluorescent bead diffusing through the nano-antenna hotspot was classified as such if before and after the identified intensity maximum the detected signal was not higher than the average signal plus three times the standard deviation.

In the case of FCS measurements, the sum of total number of photons in the antenna ROIs were not background corrected. Here the background signal and camera noise are not expected to contribute to the autocorrelation function (ACF) that is derived from the intensity trace. The autocorrelation offset however is lowered with increasing uncorrelated photons and the ACF was corrected during the postprocessing. Other potential artefacts were removed by segmenting the trace into 6 equally long parts, from which 6 individual autocorrelation curves were calculated. In an interactive reviewing step, the original intensity time trace split into 6 parts alongside the corresponding 6 autocorrelation curves were displayed and verified manually to remove parts showing sticky/abnormal (e.g. the cell membrane moving out of focus) diffusion behavior. The remaining parts were averaged into the final autocorrelation curve for each antenna and saved for the following FCS fitting step. On average 4 parts of the intensity time trace (~15 s

trace) remained after the "removing step", from which the corresponding autocorrelation curve was calculated.

6.2.5 Fluorescence Correlation Spectroscopy (FCS)

The autocorrelation curves for each nano-antenna were obtained using a multi-tau approach in a *Matlab* routine[215] and fitted in the software *QuickFit3*[216]. Given that the antenna's near-field is axially and laterally confining the detection volume, we found that the best and simplest diffusion model fitting the correlation curves is a 2D normal diffusion fit with a single component:

$$\boldsymbol{G(\tau) = G_{00}/(1 + \tau/\tau_{diff})} \qquad \textbf{Eq. 6-1}$$

with $\boldsymbol{G_{00}}$ denoting the correlation amplitude at zero lag time and $\boldsymbol{\tau_{diff}}$ the characteristic diffusion time. Those two parameters obtained from the fitting were used for further analysis and plotting.

To define the gap sizes for the bursts statistics and multiplexed FCS we used the average gap sizes of 10, 20, 25, 30 and 35 nm as measured by TEM on 25 antennas, respectively (for details see Section 2.2.6).

6.2.6 FDTD Simulations

We calculated Finite Different Time Domain (FDTD) Simulations of planar gold nano-antennas (diameter 80 nm) for various gap sizes embedded in a nano-aperture as approximately used in the experiments. Computations were made using the FDTD method in the *RSoft Fullwave* Software with a meshsize of 1 nm with 214 temporal steps of $8.1 \cdot 10^{-19}$ seconds. The simulations were calculated at a laser excitation of 633 nm. For gap sizes in the range of 10-35 nm we simulated the antenna configuration for the lateral x-y direction at the plane of the antennas and for the centered z-x and z-y planes. From the generated simulation plots, we extracted quantitative information such as the maximum intensity and the corresponding lateral and axial extensions. For a series of z heights (axial direction) above the x-y plane of the nano-antenna (z = 0 nm) we obtained the maximum intensity in the z-x and z-y cuts for different gap sizes. For the same series of z-heights for the different gap sizes, the corresponding axial extensions of the enhancement at half of the maximum intensities were obtained, the so-called Full Width Half Maximum (FWHM) in both axial cuts (z-x and z-y).

6.3 Results

Figure 6-1 a illustrates our approach to implement multiplexed fluorescence experiments at the nanoscale exploiting planar plasmonic nano-antenna arrays. We placed the antenna substrate on a sample stage which is piezo-controlled in all three dimensions. A 642 nm cw laser, matching the antennas' plasmonic resonance, was aligned onto the antenna substrate through a set of mirrors, lenses and filters and focused on the backfocal plane of a 60× 1.49 NA objective to create epi-illumination. Note that an epi-illumination is sufficient for our experiments given the rapid exponential decay of the electromagnetic near-field of the antennas in the axial direction, and the background screening effect provided by the nano-apertures. We collected the fluorescence emission of the sample through the same objective, separated from the excitation light using a dichroic and a set of filters and sent the signal onto a sCMOS camera, on a specified region of interest (ROI). To quantify the burst statistics in presence or absence of the fluorescent enhancement afforded by the nano-antennas, we detected the fluorescence intensity of 225 nano-antennas (570 × 570 pixels) simultaneously at a typical framerate of 10 frames per second. This field-of-view of 225 nano-antennas in focus is shown as a time-averaged image on the bottom panel of Figure 6-1 a. Each antenna appears as a bright diffraction-limited spot.

To assess the performance of the nano-antenna arrays employed for multiplexed fluorescence experiments, we used a testing solution of far-red fluorescent beads of 40 nm diameter and a quantum yield of about 90 %. Fluorescent beads in solution exhibit 3 D Brownian diffusion, which renders the analysis straightforward and allows us to determine the contribution due to the near-field enhancement of the antennas. However, the free 3D Brownian diffusion of beads in solution is fairly fast ($D \gg 1\ \mu m^2/s$).

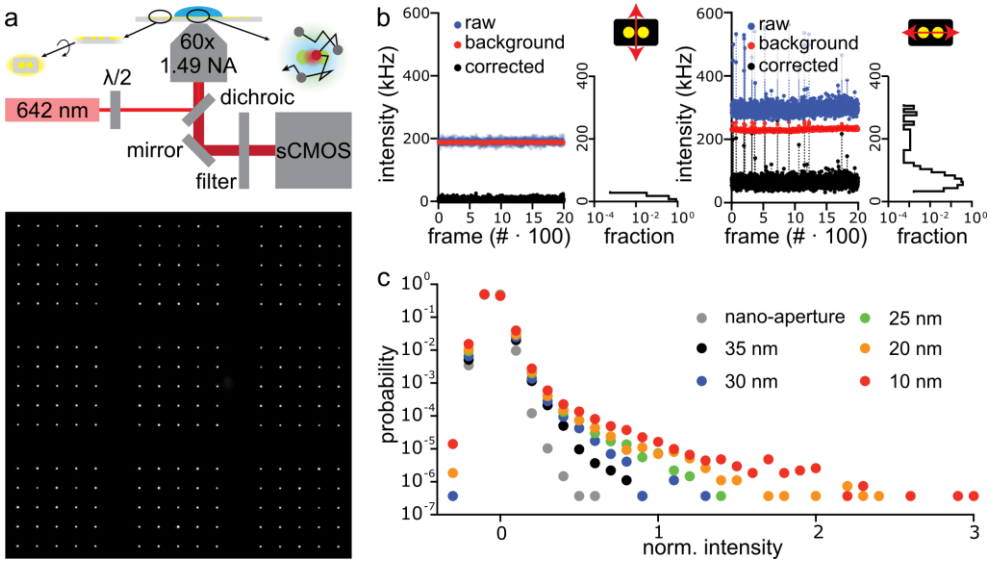

Figure 6-1. ***Multiplexed nanogap antenna detection in an epi-illumination configuration and their ensemble photon statistics distribution.*** *(a) Top panel: Schematics of the experimental configuration. 225 nanogap antennas are illuminated in the widefield using a far-red laser (642 nm) and fluorescence emission from fluorescent beads diffusing freely over the antennas is collected with a sCMOS camera. Bottom panel: A time averaged field-of-view showing the 225 nanogap antennas as bright spots in the image. (b) Representative fluorescent intensity traces of fluorescent beads (d ~ 40 nm) in a 1.6 M sucrose solution (raw data: blue dots) obtained on a single antenna of 25 nm gap size, excited with a polarization perpendicular (left panel) or parallel to the gap (right panel). Antennas become resonant only under parallel excitation along the gap, enhancing and localizing the field into hotspot regions. The raw data are decomposed into photons arriving from the nano-antenna (black dots) and background photons (red dots). The plots next to the intensity traces correspond to intensity histograms of the antenna signal (2000 frames obtained at 10 fps with 5 ms integration time). (c) Normalized ensemble photon distribution of 225 nanogap antennas measured simultaneously for gap sizes of 10, 20, 25, 30 and 35 nm, respectively, together with the nano-apertures as a control.*

In the context of antenna arrays featuring nanogaps in the range of 10-35 nm the challenge consisted in collecting the signal with a sufficiently high signal-to-noise ratio (SNR) in the short timeframe of the transiting time ($\tau \ll 100$ µs) of a fluorescent bead diffusing through the nanogap. Hence, the best trade-off yielding an acceptable SNR and allowing us to work with freely diffusing beads in solution was to slow them down in a 1.6 M sucrose solution affording a diffusion coefficient of $D \sim 1$ µm²/s.

Representative fluorescent intensity traces for a single antenna of 25 nm gap size extracted from a measurement on 225 nano-antennas with parallel and perpendicular polarization are shown in Figure 6-1 b. The fluorescence enhancement experienced by beads diffusing through the nano-antenna hotspot can clearly be distinguished as an increased signal exhibiting high intensity bursts. In Figure 6-1 b next to the intensity plotted against the sequence of frames, fractions of the occurrence of bursts at the respective intensity (same y-axis scale) are shown. It becomes evident that high intensity bursts occur frequently (depending on the fluorescent concentration) when diffusing through the nano-antenna hotspots. In contrast, such high intensity bursts remain absent for the control case of perpendicular polarization probing within an equivalent diffraction-limited spot.

A common analysis tool used in FCS is the photon counting histogram (PCH), which is used to quantify statistics of the sample such as the average number of molecules in the observation area and the photon count per sampling time and/or per molecule.[217] We generated PCHs to gain an insight into the ensemble statistics of the range of probed gap sizes in comparison with the control (nano-aperture) case. Note that for each gap size we measured the intensity from diffusing beads on 225 antennas simultaneously. To allow for a comparison among the gap sizes, each image set was normalized to its respective maximum. The resulting intensity distributions displayed in Figure 6-1 c exhibit an increasing exponential tail for the antenna nanogaps as compared to the nano-aperture control lacking the antenna dimer. This exponential tail observed on the antennas of different gap sizes indicates that bursts of increasing intensity are becoming more probable when probing within nanometric hotspots. Thus, the near-field enhancement provided by the antennas into confined hotspots is clearly evidenced, and it was obtained from a multiplexed measurement.

Next, we looked into the statistics of individual antennas, extracted from one multiplexed data set, for which we measured on 225 antennas simultaneously. The snapshot presented in Figure 6-2 a corresponds to an enlarged view of 25 antennas, all of them having a gap size of 10 nm. Bright bursts randomly occur at different antenna locations that result from the passage of individual beads through the nanogaps. On the right panel, two sequences of 30 frames out of the 2000 frame-long data set are displayed together with their corresponding (corrected) intensity traces. Both sequences show bursts of higher intensity arising at different instances. Figure 6-2 b shows the full distribution of the number of bursts recorded

during 2000 frames (10 frames/s) from an exemplary data set of 225 nano-antennas of 10 nm gap size, measured simultaneously (parallel polarization). These results demonstrate the sensitivity of our widefield excitation and detection scheme to record fluorescent bursts from individual antennas with extremely high throughput.

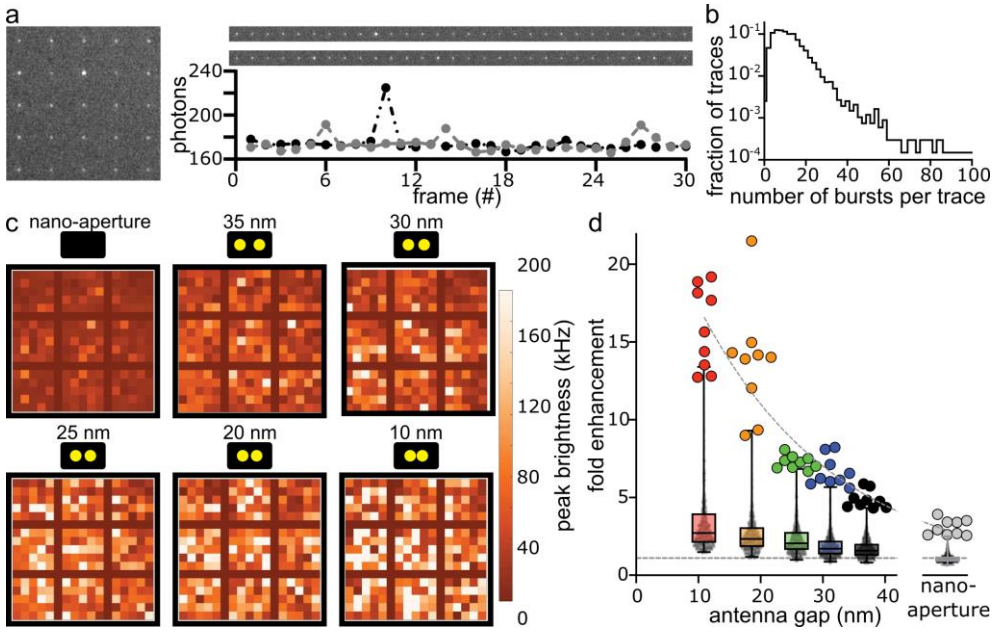

Figure 6-2. ***Single antenna burst information and enhancement per antenna.*** *(a) Left panel: A single frame of 25 nano-antennas of 10 nm gap size. The right panel displays 30 consecutive frames of the diffraction-limited spot that represents an individual nanogap antenna. The black and grey dots with dashed lines show two sets of bursts due to the diffusion of individual fluorescent beads through the nanogap hotspot. (b) The distribution of burst occurrences in a 2000 frame measurement for the nanogap antennas. (c) Peak brightness for different antenna arrays, each containing 225 antennas of the same gap size. The maximum burst intensity was extracted from traces of 2000 frames (5 ms integration time) of fluorescent beads in a 1.6 M sucrose solution. The peak brightness is color-encoded, and each pixel represents a single nanogap antenna. Each set displays nanogap antennas of decreasing gap sizes. A set of 9 nano-aperture arrays (each containing 25 nano-apertures) is also included as a control for the maximum brightness in absence of antenna near-field enhancement. (d) Fluorescent enhancement as determined from the peak brightness measurements with respect to the nano-aperture. The outliers of the distributions represent the highest peak intensities that were obtained from the best-performing antennas and follow an exponential decay as the gap sizes increase.*

We further explored the performance of the nano-antenna arrays of different gap sizes in comparison to the control (nano-aperture), equivalent to a diffraction-limited spot. For each nano-antenna we quantified the peak brightness being the maximum burst intensity over the set of 2000 images, using slowed-down diffusing fluorescent beads. Figure 6-2 c illustrates the peak performance of the nano-antenna arrays with each nano-antenna represented as a pixel and its peak brightness value encoded in the color. The measurement on 225 diffraction-limited spots (nano-apertures) exhibits uniformly spread peak brightness values, which are much weaker in comparison to measurements on the excited nano-antenna hotspots (Figure 6-2 c). The sets of 225 nano-antennas probed simultaneously reveal that with decreasing nanogap size, higher peak brightness values are obtained. For the smallest gap size of 10 nm we observe about 40 % of antennas displaying maximum peak brightness values, but even for the largest gap size of 35 nm about 3 % of the antennas may give rise to peak values of the same intensity. To quantify the fluorescence enhancement of the different antennas, the peak brightness distribution values per gap size are plotted in Figure 6-2 d, normalized to those of the control nano-aperture. Clearly, nano-antennas provide near-field enhancement with respect to the nano-aperture with the expected trend, i.e., smallest nanogaps provide highest enhancement. The outliers of the peak intensity distributions portray the best performing antennas per gap size and follow an exponential decay as the gap size decreases. The trend of increasing fluorescence enhancement with decreasing gap size has been already demonstrated in repetitive rounds of serially measuring one antenna after the other (see Chapter 2, Section 2.3). Here we validate this trend by a single multiplexed measurement on 225 nano-antennas per gap size. Indeed, with only five independent measurements (corresponding to five different gap sizes), we record statistics on over 1125 antennas.

To allow for dynamic diffusion measurements, we ramped up the framerate to 1043 fps (~ 1 ms per frame) and collected fluorescence signal for 24 000 frames. It should be noted that increasing the framerate comes at the expense of downsizing the field-of-view (FOV) on the sCMOS camera. Therefore, given our experimental conditions, we recorded information from 50 nano-antennas simultaneously, which is still a clear advantage as compared to serial recording. Figure 6-3 a shows a time-averaged image of the 50 diffraction-limited bright spots representing the nano-antennas in the FOV (i) together with a snapshot of a single nano-antenna in

focus (ii), and its respective pixel-resolved intensity shown for a cut through the antenna center (iii).

Moreover, we experimentally determined an optimal dilation radius (in number of pixels) of the camera region from which the intensity per antenna was integrated (Figure 6-3 a, iv). A dilation radius > 1 means that the signal is integrated for more than one single pixel. On the one hand, a larger area (i.e., larger number of pixels in which the signal is integrated) increases the extracted signal intensity and accounts for inaccuracies in determining the antenna position and possible lateral drift over the measurement period. On the other hand, the background contribution also increases with increasing number of pixels. Thus, a trade-off for the best achievable SNR had to be defined. To experimentally determine the best compromise in terms of pixels and SNR, we recorded intensity time traces of diffusing beads on 50 antennas of 25 nm gap size over 24 000 frames. In addition, we generated averaged autocorrelation functions following the approach explained in detail in the Methods Section 6.2.4 and determined the G_{00} values. This entire approach was performed for different numbers of pixels, and for antennas excited perpendicular to the gap.

Figure 6-3 b shows the results as a function of the number of sCMOS pixels used for photons collection for: G_{00}, (top panel); overall intensity prior to background correction (center panel); and the effective brightness of the time trace (calculated as G_{00} × mean trace intensity, bottom panel). For the delocalized antenna hotspot scenario (in red), G_{00} stays almost zero regardless of the number of pixels being used for signal integration. Moreover, although the total collected intensity scales linearly with the number of pixels, there is a negligible increase in resulting brightness. In stark contrast, for the resonant antennas (i.e., excited with parallel laser polarization, black curves), a strong dependence of the measured parameters with the number of pixels was found. Indeed, the calculated amplitude G_{00} remains constantly high up to 5 camera pixels and then, it declines steadily. Moreover, the brightness distinctly increases at the beginning, peaks for a plateau between 12 to 28 camera pixels and then decreases. Thus, we applied a dilation radius of 12 and 5 camera pixels for the photon collection to perform the burst statistics and the FCS analysis, respectively.

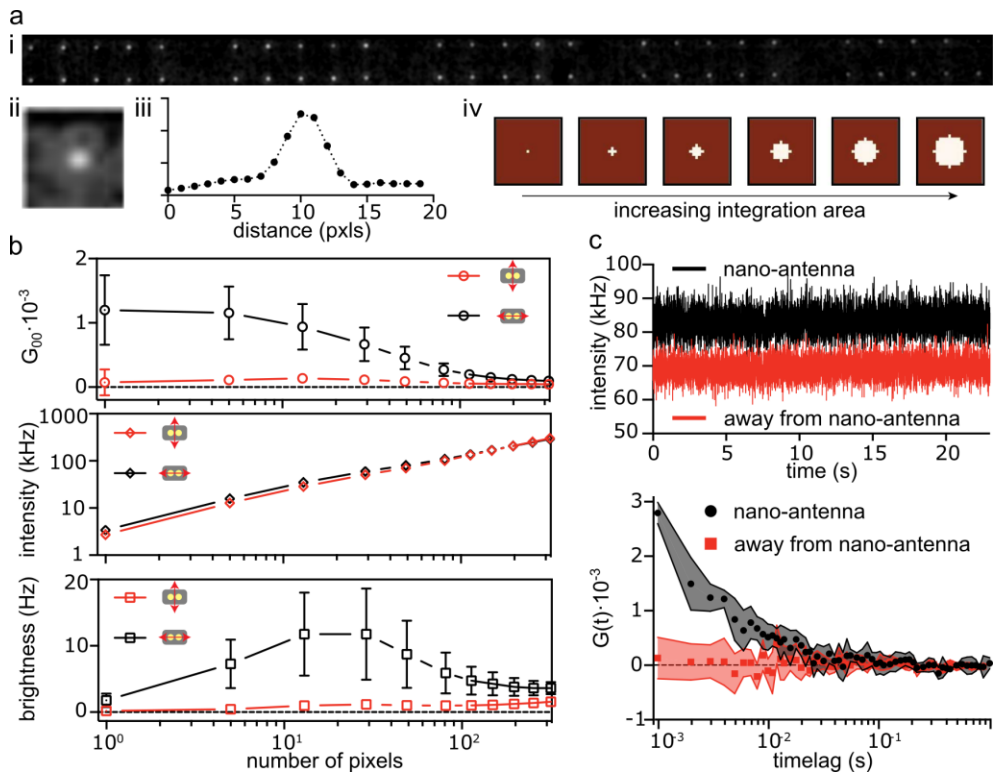

Figure 6-3. ***Simultaneous multi-antenna autocorrelation and enhancement.*** *(a) (i) A time averaged field-of-view showing 50 nanogap antennas as bright spots in the image. (ii) A magnified camera image of a single antenna depicted as a diffraction-limited bright spot. (iii) The pixel-resolved intensity is shown for a cut through the center of the antenna in (ii). (iv) Series of increasing number of sCMOS pixels from which the intensity is integrated. (b) Average over 50 nano-antennas of 25 nm gap size, as a function of the number of sCMOS pixels used for photon collection, for correlation amplitude at zero timelag, G_{00} (top panel), overall intensity prior to background correction (center panel) and mean intensity of the time trace, being G_{00} × mean trace intensity, (bottom panel) are shown. Results are shown for a laser polarization parallel to the gap (hotspot excited, black) and perpendicular to the gap (hotspot delocalized, red) as a control. (c) Top panel: Fluorescence time trace of diffusing beads recorded on a single 25 nm nanogap antenna obtained at 1043 fps (black). For the red trace signal was integrated on a camera region (of equal size) away from the nanogap antenna (bottom panel): Corresponding autocorrelation functions for the intensity traces of the top panel.*

The intensity time trace for a well-performing exemplary 25 nm gap antenna is depicted in black in Figure 6-3 c (top panel). In addition, an intensity time trace was integrated on a camera region of the same size away from the nano-antenna spot (red) and yields lower overall intensity signal with no bursts of high intensity. Thus,

this trace represents the collected background signal and validates the number of sCMOS pixels chosen for signal integration. In the bottom panel, the respective autocorrelation functions are depicted which were calculated from the intensity time traces shown in the top panel. The intensity time trace for parallel illumination exciting the antenna hotspot (black, top panel) exhibits an increased overall signal together with frequently occurring high intensity bursts if inspected closely as compared to intensity stemming from a camera ROI away from the nano-antenna. Moreover, the obtained ACF on the nano-antenna distinctly shows a diffusion behavior which can be used for further quantification such as the diffusion time. Thus, we hereby confirm our analysis routine performing with efficient background correction and artifact removal to further quantify our multiplexed data.

The experiments with slowed-down fluorescent beads demonstrate the capability of nanogap antenna arrays for multiplexed FCS at the nanoscale. Fluorescent beads in solution were suited to characterize our antenna approach in a widefield illumination configuration due to their high quantum yield and their free diffusion, so that they readily explore the 3D near-field confinement of the antenna hotspot. However, to fully exploit the advantages of our antenna arrays for parallel readout in the context of living cells, the sample's diffusion coefficient(s) should ideally lie well below 1 $\mu m^2/s$. This condition is set by the trade-off between the camera framerate, the reduced diffusion area within the nanogaps and the photon budget of the fluorescent labels to record photon counts of the actual signal well above the background level. Moreover, one should also keep in mind that the extent of the enhanced near-field excitation decays rapidly in the axial direction, as well as diverging laterally. As a consequence, the sample should be maintained in very close proximity to the nano-antennas for maximum 3D spatial confinement. This might be challenging in the context of living cells.

In order to quantify the influence of the axial position of the sample with respect to the antenna, we performed Finite Different Time Domain (FDTD) simulations for gap sizes comparable to the ones used in the experiments (see Methods section 6.2.6). The electromagnetic near-field profile of z-cuts along the x and y plane, each taken at the nano-antenna center, are displayed for the gap sizes of 15 and 25 nm in Figure 6-4 a, b. For the 15 nm gap antenna, the extremely high lateral and axial confinement into the sub-10 nm regime becomes apparent. The confinement remains high for the 25 nm gap but of decreased intensity. Furthermore, it should

also be stressed that for the larger gap of 25 nm in the z-x cut (Figure 6-4 a) the near-field becomes strongly localized at the two edges of the dimer forming the gap.

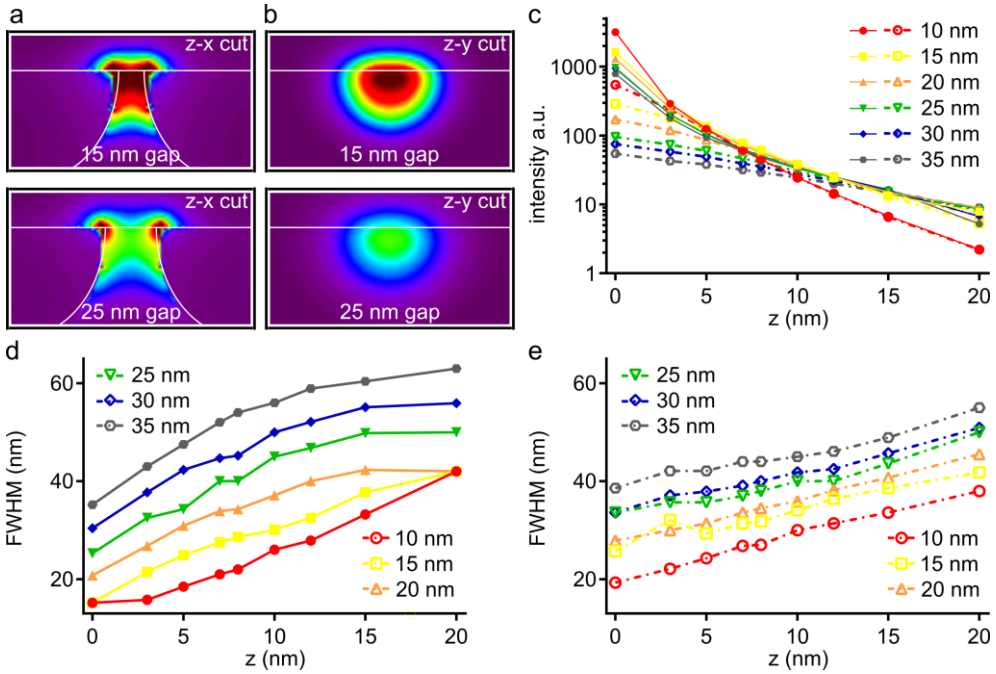

Figure 6-4. ***FDTD simulation of the axial near-field of planar nanogap antennas for different gap sizes.*** *Near-field intensity profiles along z-x cuts (a) and z-y cuts (b) for the gap sizes of 15 and 25 nm. The intensity scale is used for all the plots to allow for comparison. (c) Maximum intensity of the z-x (filled) and z-y (empty symbols) cuts as a function of the axial direction, i.e., z heights above the x-y plane of the nano-antenna (z = 0 nm), and for gap sizes indicated in the legends. (d, e) Full Width Half Maximum (FWHM) for the z-x cut (d) and z-y cut (e) as a function of axial direction and for different gap sizes.*

In Figure 6-4 c-e the quantification of the near-field in terms of intensity and lateral extension was evaluated at different z-planes above the antenna located at z = 0, for the range of gap sizes between 10-35 nm. As expected, at very short distances (< 5 nm), the near-field intensity strongly depends on the gap size, being the highest for the smallest antenna gaps. However, for z > 8 nm above the antenna plane, the field intensity decreases dramatically with negligible dependence on the gap size, except from the smallest, 10 nm gap. The common approach to estimate the lateral extension of the near-field intensity profiles is to measure the lateral distance at half of the maximum intensity of a given profile, the so-called Full Width Half Maximum (FWHM). In Figure 6-4 d, e the FWHM values are displayed for the z-x

and z-y planes, respectively, for the different gap sizes evaluated for the same z-stack as for the intensity in Figure 6-4 c. Note that also the lateral extent of the near-field becomes less dependent on the gap sizes for axial distances z > 8 nm, in particular for the z-y cut (Figure 6-4 e). As mentioned above, the larger gap sizes exhibit a strongly localized near-field at the dimer edges which explains the larger differences of the FWHM for the z-x cut (Figure 6-4 d). Such a loss of the nanogap dependence beyond 8 nm above the antenna plane has been reported previously.[93]

Having validated our multiplexed approach and analysis methodology on freely diffusing beads, we then moved to live cell experiments. For this, we concentrated on measurements of the fluorescently labeled Folate Receptor-GPI (FR-GPI) on FRAGS cells. FR-GPI is a stably transfected representative of glycosylphosphatidylinositol anchored proteins (GPI-APs).[218] GPI-APs are outer leaflet lipid-anchored proteins that associate to lipid nanodomains enriched by cholesterol, also known as "lipid rafts".[4,10,14] The GPI-AP population on living cells diffuses freely on the plasma membrane as monomers with values between ($D \sim 0.2$ - $0.5\ \mu m^2/s$).[5,14,218,219] A fraction of ~ 30% of GPI-APs expressed on the membrane have been found to form nanoclusters consisting of 2-4 molecules.[5,10,218]

FRAGS cells freely attached onto our nano-antenna platform as illustrated in Figure 6-5 a (see also in the Methods Section 6.2.2). For each single experiment, we simultaneously collected fluorescence traces of up to 50 individual antennas of similar gap size and generated individual ACFs for each antenna. Notice, that in some cases not all of the antennas excited the cell membrane as cells attached at random positions of the antenna chip. As the amount of information obtained over multiple experiments on different gap sizes is huge, we generated autocorrelation carpets (Figure 6-5 b), following a similar procedure as reported by others.[63] This so-called autocorrelation carpet visualizes the temporal evolution of the ACFs with its amplitude encoded in color over the range of monitored observation areas. The autocorrelation carpet shown in Figure 6-5 b contains a total of 84 individual ACFs, demonstrating the unprecedented high throughput of nanoscale dynamic information that can be obtained by our multiplexed approach.

In general, the autocorrelation curves exhibit higher correlation amplitudes when probing on nano-antennas in comparison to the diffraction-limited control (nano-apertures), a signature of the enhancement provided by the antennas. Importantly, a large spread on correlation amplitudes and temporal decays were obtained for all the antenna gap sizes investigated (Figure 6-5 b). These temporal and amplitude

variations are consistent with a heterogeneous organization in space and time of FR-GPI at the nanoscale.

To better quantify these results, we analyzed individual ACFs. We performed 2D Brownian diffusion fits (**Eq. 6-1**) and obtained the diffusion times and G_{00} values for all the ACFs composing the correlation carpet plot in Figure 6-5 b. As the axial distance between the cell membranes and the nano-antennas is most probably larger than 10 nm, due to extracellular components[220,221], differences arising from different gap sizes should be small (see also FDTD simulations in Figure 6-4). Therefore, to simplify our analysis, we collected all the data in single distribution plots without classifying the fittings according to antenna gap size.

In Figure 6-5 c we plot the resulting G_{00} vs. respective diffusion time τ_D (yielded by the fittings) obtained for fluorescent FR-GPI on nano-antennas (red dots) and on the control nano-aperture (green dots). As a comparison, we include the results obtained on fluorescent beads in sucrose solution (gray dots). The first observation is that the distribution of G_{00} vs. τ_D originating from multiplexed measurements on living FRAGS cells are distinctly separated from the distribution obtained from the beads. Indeed, the distribution of G_{00} vs. τ_D on beads is quite narrow, with small G_{00} values and short τ_D. As G_{00} is inversely proportional to the number of molecules observed in the observation area, the low values of G_{00} for the beads indicate a high bead concentration which was the case for our measurements. The diffusion on beads is also faster by about one order of magnitude as compared to the measurements on GPI-APs. This result is fully aligned with what is expected for freely diffusing emitters in solution in contrast to protein diffusion confined to the plane of the living cell membrane.

The distribution of diffusing FR-GPI probed by nano-antennas (red dots) is unequivocally more spread than the one probed within the diffraction-limited nano-aperture (green dots) shown in Figure 6-5 c. The distribution of the nano-aperture exhibits low G_{00} values at diffusion times which are narrowly spread around a mean diffusion time of 13 ± 5 ms (mean ± std). In contrast, when probing in nano-antenna detection areas, the resulting G_{00} vs. τ_D value pairs are widely spread with τ_D values being 15 ± 10 ms.

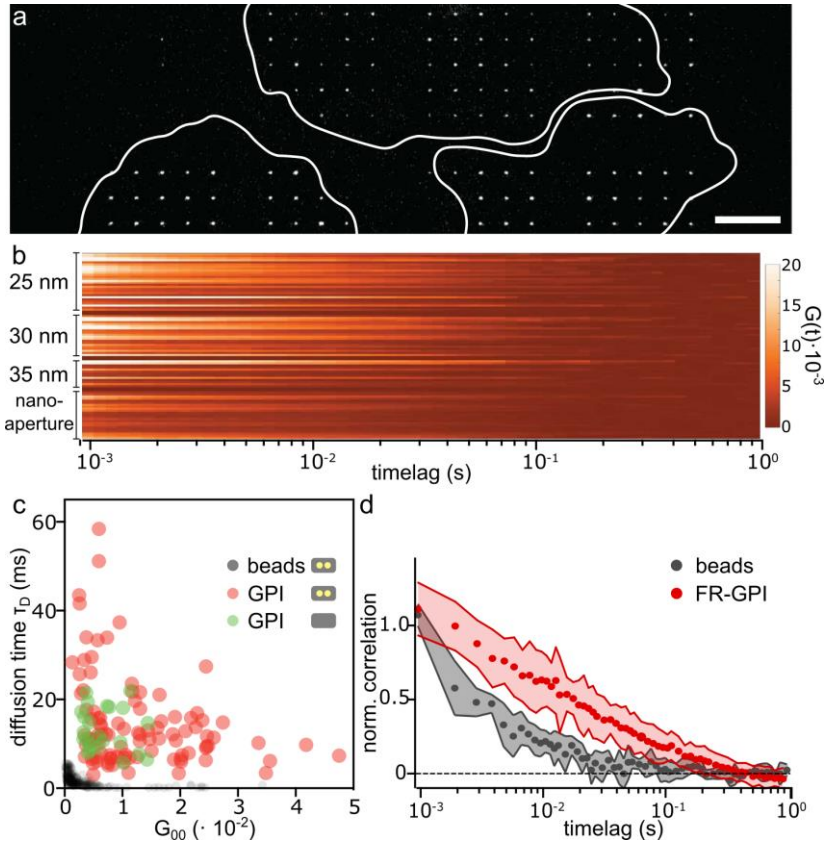

Figure 6-5. ***Multiplexed FCS at the nanoscale of fluorescent GPI-APs in the plasma membrane of living FRAGS cells.*** *(a) A camera snapshot of FRAGS cells (outlined in white) plated onto the nano antenna array platform, with the nano-antennas visible as diffraction-limited bright spots. Scale bar is 10 µm. (b) Autocorrelation carpet for three different nano-antenna gap sizes and the nano-aperture. Each line represents one autocorrelation trace of an individual antenna where the correlation amplitude G(t) is color-encoded. Data have been obtained by measuring on sets of 50 antennas of similar gap size simultaneously. The carpet displays a total of 84 autocorrelation functions. (c) Diffusion times of GPI-APs plotted against their respective autocorrelation amplitude at zero lag time (G_{00}) obtained from antennas in resonance (parallel polarization excitation, red dots), or from nano-apertures (i.e., lacking the nano-antenna, green dots). Results obtained on freely diffusing beads from resonant antennas are shown in grey for comparison. Each dot corresponds to an individual antenna measurement. (d) Normalized autocorrelation curves averaged over nano-antennas of various sizes for measurements of fluorescent GPI-AP on living FRAGS cells and compared to fluorescent beads in 1.6 M sucrose solution.*

The broad spread of G_{00} vs. τ_D values may result from varying numbers of molecules observed, nanoclusters vs. single proteins, as well as probing at different heights in the axial direction, thus resulting in the detection of molecules having experienced different degrees of fluorescent enhancement (compare to Figure 6-4). In Figure 6-5 d, normalized ACFs averaged over a multitude of nano-antennas of different gap sizes are displayed for freely diffusing beads in solution and for fluorescent FR-GPI-APs in the living FRAGS cell membrane. Herewith, we endorse the distinctly different diffusion behavior of fluorescent beads and the membrane protein FR-GPI probed in its native environment of a living cell.

We also inspected the diffusion of fluorescently labeled GPI-APs in the membrane of living primary hemocytes (for preparation details refer to the Methods section 6.2.2). Figure 6-6 a depicts the correlation carpet on different nano-antenna gap sizes in comparison to the diffraction-limited control (nano-aperture) for GPI-AP on living hemocytes. Similar to the results obtained on the FR-GPI-AP in FRAGS cells (Figure 6-5), we also observed for this cell type a heterogeneous diffusion of GPI-APs in time and space. When keeping the observation area constant, as shown for a gap size of 20 nm in Figure 6-6 b, the observed diffusion occurs over a broad range of temporal scales. From the 2D Brownian diffusion fittings we obtained diffusion times of 5.30 ms, 8.46 ms and 18.74 ms for the three exemplary ACFs on the 20 nm gap. Note that also the corresponding amplitudes exhibit variation.

The full distribution of G_{00} vs. τ_D obtained from the 2D fittings of the traces shown in Figure 6-6 a is displayed in Figure 6-6 c. In contrast to the results obtained in FRAGS cells (Figure 6-5), in hemocytes, the autocorrelation curves have in general high amplitudes (Figure 6-6). The distribution of GPI-AP diffusion in hemocytes yields mean diffusion times of 25 ± 17 ms and 35 ±15 ms for measurements on nano-antennas and nano-apertures, respectively (mean ± std, see Figure 6-6 c).

The distribution of G_{00} vs. τ_D obtained from measurements on different gap antennas shows a very large spread both on G_{00} and τ_D values. Interestingly, higher G_{00} values generally correlate with shorter τ_D values. We assign these occurrences to individual GPI-APs diffusing over the nanometric hotspot of the antennas. In contrast, lower G_{00} values tend to exhibit a large spread on τ_D. As for the case of FR-GPI-APs, there are multiple reasons that could explain such a large spread in diffusion times, including the presence of nanoclusters of different sizes and therefore od different mobilities.

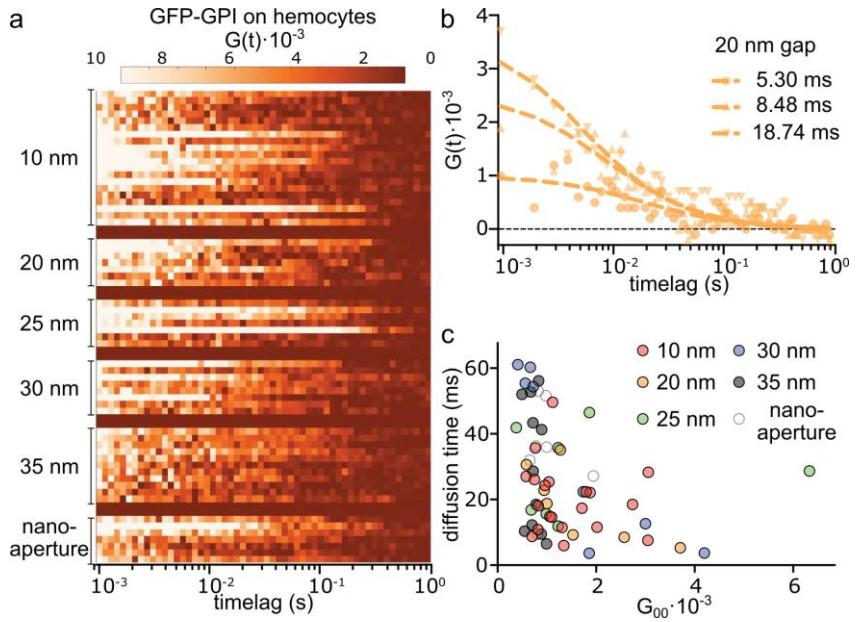

Figure 6-6. ***Multiplexed FCS at the nanoscale of fluorescent GPI-AP in the plasma membrane of living primary hemocytes.*** *(a) Autocorrelation carpet for five different nano-antenna gap sizes and the nano-aperture. Each line represents one autocorrelation trace of an individual antenna where the correlation amplitude G(t) is color-encoded. (b) Three autocorrelation curves for an antenna gap size of 25 nm together with their 2D normal diffusion fittings. The corresponding diffusion times obtained from the fittings are indicated in the legend. (c) Diffusion times plotted against their respective G_{00} values retrieved from 2D normal diffusion fittings to the traces displayed in (a).*

Finally, we performed preliminary live cell experiments of the adenosine receptor (AdoRe) on the plasma membrane of living FRAGS cells. AdoRe comprises a group of G protein-coupled receptors mediating the physiological functions of adenosine. Recently, it was reported that this adenosine receptor oligomerizes into homo- and heterodimers.[222] We investigated the nanoscale diffusion behavior of the fluorescently labeled ligand Neca transiently binding to the adenosine receptor on transiently transfected FRAGS cells using our multiplexed nano-antenna approach. Representative ACFs of fluorescent GPI-AP in FRAGS cells and in hemocytes are juxtaposed to a curve for the fluorescent AdoRe ligand Neca on a nano-antenna of 25 nm gap in Figure 6-7 a. The normalized ACF for the AdoRe ligand Neca shows slower diffusion dynamics as compared to GPI-APs. This may be a first hint for differences in the nanoscale diffusion behavior among different signaling proteins of the living cell membrane.

In Figure 6-7 b the distributions of G_{00} vs. τ_D are shown for fluorescent GPI-AP in primary hemocytes and for fluorescent AdoRe ligand Neca in FRAGS cells. Both proteins exhibit spatiotemporal heterogeneous diffusion at the nanoscale. Moreover, a rough comparison between the shapes for the clouds of the distributions of the two different fluorescent proteins corroborates the hypothesis that the diffusion behavior distinctly differs at the nanoscale.

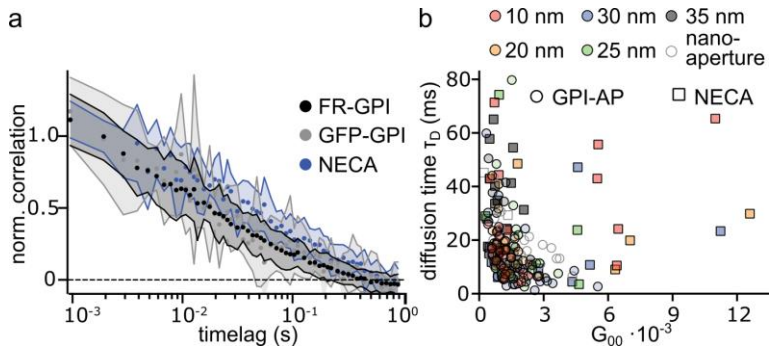

Figure 6-7. ***Multiplexed FCS to resolve nanoscale diffusion of different proteins in the living cell membrane.*** *(a) Representative normalized autocorrelation curves of fluorescent GPI-AP in living FRAGS and hemocytes in comparison to the fluorescent adenosine receptor ligand Neca on the living FRAGS membrane for a nano-antenna gap size of 25 nm. (b) Diffusion times vs. the correlation amplitude at zero lag time (G_{00}) obtained from 2D normal diffusion fittings to traces of fluorescent GPI-AP on hemocytes and of the fluorescent adenosine receptor ligand Neca in living FRAGs.*

6.4 Discussion

In this chapter, we demonstrate the multiplexing capabilities of planar gold nanogap antenna arrays implemented in an epi-illumination configuration and sCMOS camera detection for the first time to our knowledge. Furthermore, we report on multiplexed FCS measurements in living cells resolving spatiotemporal heterogeneities at the nanoscale.

First, we validate our multiplexed approach based on planar nano-antenna arrays with gap sizes of 10-35 nm with freely diffusing far-red fluorescent beads in 1.6 M sucrose solution. We assess the ensemble photon statistics. Second, we look into the single burst information per antenna extracted from a simultaneous recording on 225 nano-antennas. This allows us to quantify the fluorescent enhancement per antenna yielding the overall performance of the nano-antennas in comparison to the diffraction-limited control. Thus, we benchmark the high fluorescent enhancement and nanometric detection areas afforded by nano-antennas of

different gap sizes (10-35 nm). Third, we show the capability to perform multiplexed FCS at the nanoscale on fluorescent beads. Fourth, we apply our multiplexed nano-antenna approach to resolve the nanoscale diffusion of different proteins in the membrane of living cells. For two different cell types, FRAGS cells and primary hemocytes, we corroborate the spatiotemporal heterogeneous diffusion of fluorescent GPI-AP at the nanoscale recorded on 50 nano-antennas simultaneously. Moreover, we investigate the nanoscale diffusion behavior of the fluorescent adenosine receptor ligand Neca binding transiently to the adenosine receptor. Thus, our multiplexed approach exploiting planar nanogap antenna arrays allows us to resolve nanoscale diffusion dynamics of proteins on living cell membranes showing concurrent spatiotemporal heterogeneities.

We demonstrate in this proof-of-principle work the multiplexed capabilities of planar gold nanogap antennas in an epi-illumination configuration and sCMOS camera detection, and its suitability for multiplexed FCS in living cells. In particular, it has to be highlighted that with our approach we can readily obtain spatiotemporal data at the nanoscale with high throughput. This capability of providing an insight into nanoscale diffusion dynamics with high throughput is a clear advantage over serial recording approaches. We envision this multiplexed nano-antenna approach to be hugely beneficial in the quest of elucidating how collective molecule behavior orchestrates cellular processes.

However, we propose various ideas to further improve the performance of our approach. To exploit the camera detection area more efficiently, the spacing between the antennas could be reduced enabling more antennas to be imaged simultaneously at a higher framerate. The antenna design could also be more specifically tailored towards the cell biology question to be asked. Extremely high fluorescent enhancement might not always be required; hence the gap sizes could be larger to allow for multiplexed FCS diffusion laws extended to the nanoscale.[93,104,223224–226227]

Conclusion

This proof-of-principle work of our multiplexed nano-antenna approach using an epi-illumination configuration and sCMOS camera detection accomplished in this chapter could contribute to studies of membrane organization in living cells with high throughput. Indeed, our proof-of-principle experiments on different proteins and cell types demonstrate the highly heterogeneous organization of the cell membrane. Understanding how proteins and lipids diffuse and interact on the cell membrane is essential to decipher cell signaling. Despite the ongoing efforts over

the past decades, approaches providing high resolution in space and time at the same time in a multiplexed implementation have remained sparse. Thus, we envision a big boost for live-cell research by our successful demonstration of a multiplexed nano-antenna approach.

7 Conclusions and Future Perspectives

The principal goal of this thesis has been to elucidate the nanoscale organization of biological membranes with ultra-high resolution in space and time at the same time. We introduced an innovative planar nanogap antenna approach combined with fluorescence correlation spectroscopy providing nanometric confinement in the range of 10-45 nm together with sub-ms temporal resolution. First, we benchmarked our nano-antenna platform using freely diffusing dyes and demonstrated single-molecule sensitivity in zeptoliter detection volumes together with fluorescent enhancement factors of 10^4-10^5 at micromolar concentrations. Second, we applied our approach to reveal transient nanoscopic domains in model lipid membranes of different lipid compositions. Third, we increased the complexity of our model membrane system to study the influence of glycans, a prominent glycoprotein of the extracellular matrix, on the nanoscale lipid diffusion of model membranes. Moreover, we complemented our approach with atomic force microscopy and force spectroscopy to gain insight into the morphology and mechanical properties of these lipid mixtures at the nanoscale. Fourth, we exploited our combined FCS-nanogap antenna platform to resolve nanoscale lipid dynamics in living cells. Last, we demonstrated the multiplexing capabilities of our planar nanogap antenna arrays to follow the spatiotemporal heterogeneities of protein diffusion in living cells.

In this chapter, the main results of this PhD research are summarized, discussed and placed in perspective of promising approaches and improvements to pursue in future.

The living cell membrane is composed of a myriad of lipids and proteins forming a fluid bilayer, which separates the cytoplasm from the external environment of the cell. These lipids and proteins exhibit a range of characteristic diffusion times within the plane of the membrane. The characteristic diffusion behavior is directly related to the spatial organization of lipids and proteins into nanodomains and meshwork at the micron- down to the nanoscale. Importantly, it has been demonstrated that the spatiotemporal organization of the cell membrane is linked to its function, e.g. signaling and trafficking.[1,2,6,7,9,64,157] Single-molecule fluorescence approaches, including super-resolution techniques have enormously advanced our understanding of the dynamic nanoscale organization of the plasma membrane.[4,64,122,124] On the one hand, standard single-molecule detection is commonly performed using diffraction-limited confocal excitation implying that exploration of single-molecule dynamic events requires ultra-high dilution of the sample (i.e., working at pM range), well below the physiological concentrations at which relevant biological processes take place (µM-mM range). Super-resolution microscopy on the other hand, can explore nanoscale regions of the plasma membrane at the expense of extremely low temporal resolution, precluding studies on the transient and dynamic organization of biological membranes.

In this dissertation we have introduced an innovative technique of planar plasmonic antennas combined with fluorescence correlation spectroscopy (FCS). Our approach provides both high spatial and temporal resolution together with single-molecule sensitivity to resolve nanoscale diffusion of lipids and proteins in the living cell membrane.

As introduced in Chapter 2, our antenna design consists of a gold dimer pair with a diameter of 80 nm separated at various gap sizes in the range of 10-45 nm. In contrast to standard nano-antenna fabrication techniques that leave the region of maximum field localization buried into the substrate, we developed a new approach that makes this region directly accessible to fluorescent emitters. Our nanofabrication process combines electron beam lithography together with a planarization step, etch back and template stripping. The dimensions of the gold dimer guarantees its resonance and thus maximum near-field enhancement in the red region of the visible spectrum, while the gap sizes define the degree of the near-field enhancement and localization. The last fabrication step of template stripping planarizes the nano-aperture and flips the plasmonic hotspot to the surface, so that both the antenna and the sample are in close proximity to each other. This flipping step enables optimal near-field excitation from the antenna on the biological

sample. In addition, the gold dimers are embedded within a box nano-aperture filled with a transparent polymer rendering the surface continuously planar (of a planarity better than 3 nm) and thus an ideal platform to probe biological membranes. Spurious background fluorescence is screened by the gold layer (thickness of 50 nm) surrounding each dimer pair in the box nano-aperture. Hence, the signal-to-background ratio is highly increased and allows for the detection of individual molecules within the hotspot region provided by the nanogap antenna. Owing to these nanofabrication advances, we demonstrated giant fluorescence enhancement factors of up to 10^4-10^5 times in ultra-confined detection volumes, together with single-molecule detection in the micromolar range.

In Chapter 3 of this thesis we applied these planar gold nano-antennas in combination with FCS for the investigation of the dynamic organization of mimetic lipid membranes at the nanoscale with microsecond time resolution. First, we validated the suitability of planar nano-antenna arrays on single-component DOPC bilayers, obtaining free diffusion over the length scales investigated (down to 10 nm), and consistent with a homogenous lipid distribution. Free diffusion was also observed on DOPC:SM binary mixtures, although a large spread of the diffusion times was retrieved. These variations indicated local fluctuations of SM within larger areas of solely DOPC, but without the formation of detectable nanodomains that would constrain dye diffusion. Addition of cholesterol resulted in microscopic phase separation and the formation of transient nanoscopic domains in both the liquid ordered (Lo) and liquid disordered (Ld) phases, with sizes below 10 nm and lifetimes in the microsecond time scale. Since the basic biochemistry operating in lipid model membranes is similar to that in the plasma membrane, we proposed that the nanoscopic domains detected might correspond to the unstable lipid rafts predicted to exist in living cell membranes.

There is emerging interest in deciphering the influence of adjacent extracellular glycan components on the spatiotemporal organization of the cell membrane. In Chapter 4, we increased the complexity of our experimental system to investigate the influence of the glycosaminoglycan Hyaluronic Acid (HA) on the repatterning of mimetic lipid membranes at the nanoscale. We performed FCS measurements in confocal and at the nanoscale using our planar antenna arrays on different lipid mixtures with and without HA. Furthermore, we complemented our studies using atomic force microscopy and force spectroscopy. With our combined and extended approach, we revealed a distinct influence of HA on the nanoscale lipid organization of mimetic membranes composed of lipids constituting the more ordered phase.

We suggested a synergistic effect of HA and cholesterol on inducing and/or enhancing the formation of nanoscopic heterogeneities. Our results advocate for a role of the glycocalyx matrix regulating the lipid bilayer organization at the nanoscale, similar to the way it has been shown that the actin cytoskeleton orchestrates the occurrence of so-called lipid rafts. Our combined approach provides the required spatiotemporal resolution, mechanical sensitivity, and delivers quantitative parameters at the nanoscale that might highly benefit the modeling of biological systems.

Switching from more controllable mimetic membranes to living cell membranes, we employed our planar nano-antenna platform combined with FCS to study the nanoscale dynamics of different lipids in living cells. In Chapter 5 we investigated the diffusion dynamics of two fluorescent lipid analogs, phosphoethanolamine (PE) and sphingomyelin (SM), on living cell membranes. With our nanogap antennas we were able to breach into the sub-30 nm spatial scale on living cell membranes for the first time. Together with cholesterol depletion experiments, we provided compelling evidence for the existence of highly transient and fluctuating nanoscale assemblies of sterol and sphingolipids in living cell membranes. By means of FCS and single burst analysis we revealed striking differences between PE and SM diffusion dynamics that remain hidden in confocal measurements.

Finally, in Chapter 6, we demonstrated the multiplexing capabilities of planar plasmonic nano-antenna arrays of different nanogap sizes (10-35 nm) implemented in a widefield illumination configuration together with sCMOS camera detection. We first demonstrated simultaneous readout of more than 200 antennas at the time, which constitutes a major increase in data throughput. We assessed the performance of the nanogap antenna arrays for multiplexed FCS and burst analysis at the nanoscale with millisecond temporal resolution. We successfully extended our approach to probing protein diffusion in living cell membranes at the nanoscale in a simultaneous parallel detection scheme on over 50 antennas. We demonstrated that our approach maintains the high spatiotemporal resolution and biocompatibility offered by the antennas together with a remarkable high throughput in data acquisition. We recorded large variations in diffusion times and spatial organization on all proteins investigated, consistent with the large spatiotemporal heterogeneity of living cell membranes. Therefore, we envision many multiplexed studies with high spatiotemporal resolution at the nanoscale continuing to increase our understanding of the cell membrane organization and its link to the cell's function.

The current design of an antenna platform consisting of thousands of planar nanogap antennas-in-box of different gap sizes is the result of significant efforts in the field of plasmonics pushing antenna developments towards biosensing and biological applications in general. The large-scale availability of nano-antennas offering ultra-high spatial confinement and fluorescence enhancement into hotspots directly accessible on a planar surface has been key to conducting this PhD research. The combination of this type of planar nanogap antenna arrays with FCS has been a merging of the best of two worlds. On the one hand, the planar nano-antenna arrays provide spatial confinement to gap sizes in the range of 10-45 nm. The availability of arrays further allows probing of spatial heterogeneities of the sample under study and being ideally suited to look into the cell membrane organization from the nano- to the micron-scale. FCS on the other hand, is a powerful non-invasive optical technique with high temporal resolution down to microseconds but is commonly implemented within a diffraction-limited (~ 250 nm) spot. Thus, our combined FCS-nano-antenna approach perfectly matches the requirements to elucidate how cell membrane organization dynamically (re)patterns at the nanoscale by its interaction with intra- and extracellular components. However, as always, there is room for improvement, in particular to facilitate investigations of more complex questions of cell membrane dynamics, one being interactions between lipids and proteins for example.

Currently, the spatial arrangement of our nano-antennas on the planar substrate consists of a separation of 4 μm between antennas. In view of the multiplexing implementation based on camera detection, it would be beneficial to place the nano-antennas with a narrower spacing to allow for a more efficient use of the camera field of view. A closer antenna spacing would either allow for a higher number of multiplexed antennas or would reduce the camera detection area to attain microsecond time resolution. A limit of how close the antennas could be spaced in the array would lie below 1 μm down to ~ 500 nm. For antenna-to-antenna distances, or grating pitches, below 500 nm peculiar optical phenomena such as surface lattice resonances occur which would alter the antenna resonance position.[228–231] These lattice resonances depend on the exact antenna size and design, the grating pitch and also on the material and environment. With respect to nanofabrication challenges, antenna arrays down to 500 nm have been attained routinely by electron-beam lithography as well. Hence, when designing a novel planar nanogap antenna with less than 4 μm spacing one would need to consider lattice resonances and optimization of the nanofabrication process. However, a

grating pitch of 0.5-1 µm would definitely be achievable and constitutes a huge benefit for the increased wealth in information of cell membrane organization studies.

Moreover, depending on the question of interest, larger gap sizes might be sufficient for studying dynamics on living cells. A lateral confinement of the near-field into hotspots of 10-45 nm also implies a rapidly decaying near-field in the axial direction. As shown in FDTD simulations in Chapter 6, the fluorescence enhancement of the smallest antenna gap of 10 nm can be exploited for a high increase of the signal-to-noise if the fluorophore diffuses within less than 10 nm of axial separation to the nano-antenna. However, when plating living cells on top of the nano-antenna substrates the physical separation between the fluorescently labeled protein or lipid of interest diffusing in the plane of the membrane may easily exceed 10 nm. Thus, to permit the nanoscale extension of FCS diffusion laws in living cells using our multiplexed nano-antenna implementation, it would be favorable to adapt the antenna design to provide gap sizes of nanometric lateral confinement but less rapid axial near-field divergence. Probably the most obvious initial idea would be to enlarge the gap size. However, planarized aluminum based nano-apertures have not shown a diffusion dwell time dependence for diameters between 60 to 250 nm and above 10 nm above the aperture.[93] This shows the intricate interplay between near-field localization, thus enhancement and lateral and axial spatial extension. The smaller the gap, the stronger is the near-field enhancement but with a rapidly decaying near-field. When the gap becomes larger, the near-field weakens, however strong localizations remain at the sharp antenna edges as has been seen for the larger gap sizes in the FDTD simulations in Chapter 6 and the planarized aluminum based nano-apertures[93]. Moreover, to guarantee a sufficiently high signal-to-noise ratio very bright dyes would need to be used for larger gap sizes providing weaker enhancement. Thus, a realistic approach to allow for the nanoscale FCS diffusion law extension in a multiplexed fashion would be to still use planar antenna arrays of gap sizes below 50 nm but implementing a more sophisticated data analysis. The contribution from the sharp antenna edges must be ultra-short and of constant nature. Thus, this contribution could be eliminated as part of the data analysis routine or even filtered out if the fluorescent lifetime of the dyes is simultaneously collected.

Gold nano-antennas exhibit many advantages such as high field enhancement, nanometric field confinement, optimized nanofabrication protocols to ensure minimal surface roughness, chemical inertness and bio-combability. However, the

plasmonic resonances sustained by gold nano-antennas lie in the red to far-red wavelength range of the electromagnetic spectrum, restricting experiments to a single color. Hence, to extend to multi-color excitation and detection schemes of our planar nanogap antenna approach, the material would need to be changed. In the regime of plasmonic materials, aluminum is the most promising candidate offering moderate fluorescent enhancement over a broad range of the visible spectrum, perfectly matching the spectrum of fluorophores commonly used in live-cell research.[93,223] Aluminum antennas for biological applications have been developed and employed for membrane studies in our group already.[104] However, the antenna design for aluminum antennas would need to be optimized to afford a similar performance as the planar gold nanogap antenna approach on a broadband wavelength range together with live-cell compatibility. Furthermore, there might be new antenna approaches suited for live-cell research at the nanoscale based on silicon, two-dimensional materials, or other novel materials.[224–226]

To investigate the influence of HA, an abundant constituent of the glycocalyx matrix, on the nanoscale lipid organization, we complemented our FCS-nano-antenna approach with AFM and force spectroscopy. In addition to the diffusion dynamics at the nanoscale, this correlative approach allowed us gaining insight into the topography and mechanical properties of the lipid bilayer due to HA. Correlative approaches are emerging as feasible, reliable and yield valuable results in our quest to decode the compositionally heterogeneous cell membrane organization, and the passive and active influence of adjacent structures on the intra-and extracellular side.

To decipher the complexity of cell membrane organization and dynamics and its impact on membrane function it is of outmost importance to continue developing and improving our biophysical toolbox. As shown also in the work of this PhD research, it is essential to observe and quantify the interaction of lipids and proteins in their native environment of the living cell at a variety of spatiotemporal scales. To determine modes of diffusion and clustering behavior single particle tracking (SPT) approaches including video-rate interferometric scattering microscopy (iSCAT), yielded remarkable results.[78] Moreover, conventional SPT using small emitters, can be nowadays implemented at low and high labeling densities. This approach has recently allowed to correlate clustering of signaling proteins together with their dynamics at the nano- and meso-scale.[178,180] Another super-resolution technique capable of looking into nanoscale membrane dynamics is scanning stimulated emission depletion (STED)-FCS allowing the resolution of

spatiotemporal heterogeneities in living cells down to ~ 30 nm resolution.[63] The onset of fast and sensitive detection cameras has permitted the generation of spatial maps of mobilities and interactions in living cells from a single experiment.[206] All these approaches constitute our current biophysical toolbox and have tremendously increased our understanding of the living cell membrane dynamics. All these techniques also have their inherent technical challenges, e.g. regarding spatiotemporal resolution, and live-cell compatibility, which need to be addressed to resolve the remaining mysteries of cell membrane organization.[232]

Our combined approach of planar nanogap antenna arrays with FCS enabled us to gain insight into the spatiotemporal membrane organization at the nanoscale. In the scope of this thesis we could also demonstrate the multiplexing capabilities of our approach as an implementation in widefield illumination and with sCMOS camera detection (Chapter 6). Nano-antennas make it possible to follow cell membrane dynamics with ultrahigh spatiotemporal resolution at the nanoscale. However, they become inefficient at longer temporal and larger spatial scales. The next push forward may consist in enabling the simultaneous multiplexed readout over multiple spatiotemporal scales. A possible configuration would be the use of two opposing objectives which illuminate the fluorescently labeled sample from both sides and collect the fluorescence emission from both sides. Depending on the cell biological question to be answered, the implementation would then vary in detail. The configuration could be either in epi-illumination or in the 4Pi confocal scheme[233]. On the detection side, either two cameras, even of different dynamic range, or two single photon avalanche diodes (SPADs) or a combination could be employed. In combination with a SPAD, a pulsed laser illumination and a time correlated single photon counting module could be implemented to simultaneously collect fluorescent lifetime information. Our planar nanogap antenna arrays would remain as a sample. Thus, one detection side would collect the fluorescent emission stemming from the antennas looking into the nanoscale diffusion and the other side would collect diffusion dynamics from a widefield or confocal detection volume. With two objectives it would be even possible to collect from different planes in the sample. With two fast and sensitive cameras it could be envisioned to perform (multiplexed) Imaging FCS (ImFCS) in a diffraction-limited widefield volume and on the nano-antennas in parallel. The combination of a camera for ImFCS in the diffraction-limited spot and a SPAD to collect from the nano-antennas would allow for sub-ms temporal resolution at the nanoscale. With such a configuration of two objectives and planar gold nano-antennas, it would be straightforward to detect

two colors, namely in the red regime on the antennas and in the blue regime, i.e., labeling a molecule of interest for the diffraction-limited detection side. Overall, the optical implementation would be more complex but the increase in potential insight into the cell membrane organization correlating over multiple spatiotemporal scales would be tremendous.

Common to all of these approaches capturing the cell membrane organization at the nanoscale is the extremely intensive data acquisition and data analysis. Thus, modes of efficiently detecting and analyzing such amounts of data have to be developed further. With software advances, novel approaches of analysis based on Bayesian, machine and deep learning algorithms are improving in reliability. In particular, the endeavor goes into autonomous data analysis paradigms helping to remove the human-induced bias in sorting obtained data curves for further fitting from measurement artifacts. Such autonomous approaches may replace the decision-making of choosing the best fitting model for the obtained FCS data in the future.[227]

In summary, in this thesis we introduced an innovate approach of planar gold nano-antenna arrays of different gap sizes (10-45 nm) combined with FCS offering ultra-high spatial and temporal resolution at the same time. We validated our approach by yielding unprecedented fluorescent enhancement factors for freely diffusing molecules. Most importantly, we applied our nano-antenna approach to biological membranes. On mimetic membranes we were able to resolve transient nanoscopic heterogeneities and decoded the influence of a constituent of the adjacent extracellular matrix on lipid organization at the nanoscale. On living cell membranes, we detected for the first time lipid heterogeneities with a resolution below 30 nm. In particular, the successful demonstration of the multiplexing capabilities of our combined FCS-nano-antenna approach will serve useful in the future to enlighten the spatiotemporally heterogeneous diffusion of lipids and proteins in living cell membranes at the nanoscale. Further improvements of the antenna design allowing for multi-color detection and nanoscale FCS diffusion laws can be developed and open the door to observe heterogeneous cell membrane interactions and (re)organization from the nano- to the micron-scale.

There is a crack in everything. That's how the light gets in. *Leonard Cohen*

Publications

List of publications included in this thesis

Flauraud, V., Regmi, R., **Winkler, P.M.**, Alexander, D.T., Rigneault, H., van Hulst, N.F., García-Parajo, M.F., Wenger, J. and Brugger, J., *In-plane plasmonic antenna arrays with surface nanogaps for giant fluorescence enhancement.* Nano Letters, 2017 (3), pp.1703-1710.

Winkler, P.M., Regmi, R., Flauraud, V., Brugger, J., Rigneault, H., Wenger, J. and García-Parajo, M.F., *Transient nanoscopic phase separation in biological lipid membranes resolved by planar plasmonic antennas.* ACS Nano, 2017 11(7), pp.7241-7250.

Regmi, R., **Winkler, P.M.**, Flauraud, V., Borgman, K.J.E., Manzo, C., Brugger, J., Rigneault, H., Wenger, J. and García-Parajo, M.F., *Planar optical nanoantennas resolve cholesterol-dependent nanoscale heterogeneities in the plasma membrane of living cells.* Nano Letters, 2017 (10), pp.6295-6302.

Winkler, P.M., Regmi, R., Flauraud, V., Brugger, J., Rigneault, H., Wenger, J. and García-Parajo, M.F., *Optical Antenna-Based Fluorescence Correlation Spectroscopy to Probe the Nanoscale Dynamics of Biological Membranes*. J. Phys. Chem. Lett., 2018, 9, 1, 110-119.

Winkler, P.M., Campelo, F., Giannotti, M. I., García-Parajo, M.F., *Nanoscale imprint of glycans on lipid membrane dynamics unveiled by planar plasmonic nanogap antennas and atomic force spectroscopy.* (submitted to J. Phys. Chem. Lett.)

Winkler, P.M., Van Zanten, T. S., Mayor, S., García-Parajo, M.F., *Multiplexed Fluorescence Correlation Spectroscopy at the nanoscale using planar plasmonic antenna arrays.* (in preparation)

Other publications from the author not included in this thesis

Regmi, R., Berthelot, J., **Winkler, P.M.,** Mivelle, M., Proust, J., Bedu, F., Ozerov, I., Begou, T., Lumeau, J., Rigneault, H., García-Parajó, M. F., Bidault, S., Wenger, J., Bonod, N., *All-Dielectric Silicon Nanogap Antennas To Enhance the Fluorescence of Single Molecules*. Nano Letters, 2016, (16), 8, pp. 5143–5151.

Winkler, P.M., Campelo, F., Giannotti, M. I., García-Parajo, M.F., *Planar plasmonic antenna arrays resolve transient nanoscopic heterogeneities in biological membranes.* Proceedings Volume 11246, Single Molecule Spectroscopy and Superresolution Imaging XIII; 112460F (2020)

Conference presentations

In-plane plasmonic antenna arrays resolve nanoscopic heterogeneities in model lipid membranes. **Winkler, P.M.**, Regmi, R., Flauraud, V., Brugger, J., Rigneault, H., Wenger, J., García-Parajo, M.F*., SPIE Optics + Photonics Conference 10346*, San Diego, USA, August 2017.

Plasmonic nanogap antennas to reveal spatiotemporal heterogeneities of model lipid membranes. **Winkler, P.M.**, Regmi, R., Flauraud, V., Brugger, J., Rigneault, H., Wenger, J., García-Parajo, M.F*., 2nd IRB Barcelona PhD Students' Retreat*, 08370 Calella, Spain, November 2017.

Planar plasmonic antenna arrays resolve transient nanoscopic heterogeneities in biological membranes. **Winkler, P.M.**, Regmi, R., Flauraud, V., Brugger, J., Rigneault, H., Wenger, J., García-Parajo, M.F, *Nanolight 2018 conference,* Benasque, Spain, March 2018.

Planar plasmonic antenna arrays resolve transient nanoscopic heterogeneities in biological membranes. **Winkler, P.M.**, Regmi, R., Flauraud, V., Brugger, J., Rigneault, H., Wenger, J., García-Parajo, M.F, 15th *International conference of Near-field Optics and Nanophotonics (NFO-15),* Troyes, France, August 2018.

Planar plasmonic antenna arrays resolve transient nanoscopic heterogeneities in biological membranes. **Winkler, P.M.**, Regmi, R., Flauraud, V., Brugger, J., Rigneault, H., Wenger, J., García-Parajo, M.F, *26th International Workshop on "Single Molecule Spectroscopy and Super-resolution Microscopy",* Berlin, Germany, September 2019.

Planar plasmonic antenna arrays resolve transient nanoscopic heterogeneities in biological membranes. **Winkler, P.M.**, Campelo, F., Giannotti, M. I., García-Parajo, M.F., *SPIE Photonics West BiOS*, San Francisco, USA, February 2020.

Multiplexed Fluorescence Correlation Spectroscopy at the nanoscale using planar plasmonic antenna arrays. **Winkler, P.M.**, Van Zanten, T. S., Mayor, S., García-Parajo, M.F., *Nanolight 2020*, Benasque, Spain, March 2020.

Acknowledgements

I don't have a particular recipe… doing research is challenging as well as attractive. It is like being lost in a jungle and trying to use all knowledge that you can gather to come up with some new tricks, and with some luck you might find a way out. *Maryam Mirzakhani*

This quote by this outstanding mathematician perfectly summaries my PhD journey. To my recipe, I definitely need to include the people I had to chance to meet adding the essential salt and spices to this enrichening PhD (cocktail) experience of the past five years.

All this started with Maria, my supervisor convincing me that demystifying cell membrane organization with nano-antennas in an interdisciplinary team is the perfect mix. Maria, I am more than thankful for your guidance, frankness and exuberant enthusiasm to understand the (nano) things of life. Thanks for encouraging me to push and grow with your critical questions but always keeping in mind the bigger picture. For deciphering my (extremely) long sentences and for opening the door to verify that ICFO remains the best lab in comparison to Marseille, IBEC and Bangalore. For the freedom, I experienced to invest myself in ICONS matters and for supporting all my conference endeavors until the (lockdown) end.

The initiation to my PhD journey took place at the Institut Fresnel in Marseille, and I could not think of a better one. Thanks to Jerome, I was already in the lab exploring the diffusion of single red dye molecules on my first day. The following four months not only set the basis for the scientific side of my PhD thanks to Raju and Jerome, but above all, gave me the feeling that I am at home in the international researcher's world and that I will never walk alone. Susmita, I am looking forward to adding more (travel) memories to our list and make more dosas together (maybe iniviting Swaroop to join ^^). Thanks to Mathias (where do we meet next time?), Sid, Naveen, Sounderya, Satish, Victor, Vasyl, Juan, Hadrien, Alberto, Tassos for including me from the first day.

The transition to ICFO would never have been that smooth if not for Kyra, who not only shares my love for profound coffee chats and tight hugs, but also keeps on inspiring me how to successfully navigate a research career with your family.

Thanks to Maria and Mathieu for forming the nano-(conference)-family and enduring the takeover of the super-resolution-immunology-golgi-focal adhesion of the SMB family. Thanks to Felix and Carlo for all your in-depth questions bringing in an alternative perspective into my projects. And thanks to Nico, Juan, Alberto, Iza, Laura, Pablo, Natalia, Enric, Morgan, Jessica, Lukas and Ediz for being the amazing and unique SMB group (always finding a reason to celebrate with cake and cava).

My PhD would lack many facets if not Sarah decided that ICFO is the right place for her as well. Together we made it through so many struggles, discussions, Social Fridays and happy moments in and outside ICFO. Let's hope we explore (and test some gin) in Galicia soon.

In my case, the student chapter ICONS is intricately tied to my PhD time at ICFO. My involvement in ICONS allowed me to grow personally in so many different ways. But above all, the interaction with all the people I could connect with at ICFO and beyond was worth every single extra time spent. Thanks to all the dedicated ICONS members who I was lucky to work with and learn from. Especially thanks to Roland, Juan Miguel (also for convincing me to join which worked even without a beer ^^), Lisa, Jana and Samyo for becoming friends as well.

Bárbara, you definitely keep on adding drive and inspiration to my life since the moment you stepped in. Continue to be the *amazing girl* you are.

My PhD and ICONS time would not have been possible without the support from all the ICFO units starting with HR, in particular thanks to Manu, Anne and Mery. Big thanks to the departments of IT, Purchasing, Travel, Events and Logistics, the mechanical and electronic workshops and the Biolab with Angel, Merche and Cesar. Thanks to ICONS I was able to interact in more depth with the KTT, Financing and Communications departments. In particular, I was fortunate to work with Silvia, Alastair, Rob, Rafa and Brook. Thanks to Lluis and Dolors for managing ICFO so well that it continues to prosper incredibly.

My decision of living in Castelldefels was based on that I would be able to go for a run (+swim) on the beach instead of commuting. I was not prepared to meet the great Castefa gang of Julio, Ugaitz, Iker, Catarina, Eduardo, José, Álvaro, Antoine, Vikas, Anuja, Rinu, Vindhiya and Nitin. Cheers to many fun times at the beach, testing restaurants, cooking together and during weekend trips. Alican and Inci,

you also count to this group of great people and especially thanks for daring to get initiated to camping and “short” walks in the Pyrenees.

One reason why I never considered moving elsewhere is thanks to my lovely flatmates, Kavitha, Irene, Nick, Rurico, Stephy and Alex, with whom I had the chance to share delicious dinners, sweaty workouts and many more life-educating moments.

Kavitha and Sandra, the core of my Castefa gang, we share countless memories, and I could not feel happier that I had the chance to meet you during my PhD time. Kavitha, the brownie in my life and flat, I am looking forward to coming to (legendary) Londonderry. Sandra, finally it’s written: I am NEVER annoyed when you text me and I am eager to explore another part of the world together. Here’s to us!

Sometimes people do not only bump in one’s life but literally hit you. Pauliiins, thanks for causing me only once a blue eye and starting a conversation on electronic music. There is no time for a goodbye, my (dance) partner in crime.

Thanks Marina for not only saving my project on which I almost gave up by showing me how AFM in sugary liquid works but for becoming a mentor and friend as well. Davia, thanks for becoming my IBEC sister and lifting each other up during our PhD journey. I can’t wait to celebrate together.

My two stays at NCBS in Bangalore broadened my horizon in so many aspects. They allowed me to gain a deep insight in cutting-edge cell biology, which still keeps me in awe, but again it is about the people I met and resulting friendships I could make. Jitu, I am really grateful that you welcomed me to your group under your guidance. With your thoughtful questions, I started to see and appreciate nano-antennas in a different light. Thomas thanks for your dedication and all the hours spent together in the lab, on Skype and beyond. If someone is able to multiplex nano-FCS and life, it is you, together with Ksenia and Darya. Parijat and Farhana, our friendship was sealed in Edinburgh and I am eager to see what places we will discover together in future. Sanjeev, Arnab, Chaitra, Chandrima, Sankarshan, Joseph and Joey, thanks for all the sincere discussions, culinary delights and fun times together.

The foundation for my PhD journey was built during my studies of physics, back home in Austria. Pascal, thanks for all the discussions about physics and life and your friendship since day one. Thanks to Lukas and Robert, my partners in crime

for any experiment in and outside the lab. One time we will all celebrate together the birthday of Robert in his (Pampa-) town. Andi, thanks for all the encouraging messages, conversation and stunning pictures you shared with me whenever I was wondering about (PhD) life or just needed a push to exploit the fact that ICFO is located close to the sea and the mountains.

To my parents, Dieter and Andrea, my three sisters Melina, Pia and Lucia, my grandfather Pip and my uncle Pet no *thank you* would suffice to acknowledge my gratitude for all the support and love I received throughout the PhD years despite the distance. You gave me the confidence to pursue my dreams, thus this PhD equally belongs to you.

Stories never really end...even if the books like to pretend they do. Stories always go on. They don't end on the last page, any more than they begin on the first page. *Cornelia Funke*

And I am curious to discover the next chapter of my story.

8 References

1. Brown, D. A. & London, E. Functions of Lipid Rafts in Biological Membranes. *Annual Review of Cell and Developmental Biology* **14**, 111–136 (1998).
2. Lingwood, D. & Simons, K. Lipid Rafts As a Membrane-Organizing Principle. *Science* **327**, 46–50 (2010).
3. Kusumi, A. *et al.* Paradigm Shift of the Plasma Membrane Concept from the Two-Dimensional Continuum Fluid to the Partitioned Fluid: High-Speed Single-Molecule Tracking of Membrane Molecules. *Annual Review of Biophysics and Biomolecular Structure* **34**, 351–378 (2005).
4. Sezgin, E., Levental, I., Mayor, S. & Eggeling, C. The mystery of membrane organization: composition, regulation and roles of lipid rafts. *Nature Reviews Molecular Cell Biology* **18**, 361–374 (2017).
5. Gowrishankar, K. *et al.* Active Remodeling of Cortical Actin Regulates Spatiotemporal Organization of Cell Surface Molecules. *Cell* **149**, 1353–1367 (2012).
6. Simons, K. & Ikonen, E. Functional rafts in cell membranes. *Nature* **387**, 569 (1997).
7. Pike, L. J. Rafts defined: a report on the Keystone symposium on lipid rafts and cell function. *The Journal of Lipid Research* **47**, 1597–1598 (2006).
8. Jacobson, K., Mouritsen, O. G. & Anderson, R. G. W. Lipid rafts: at a crossroad between cell biology and physics. *Nature Reviews Molecular Cell Biology* **9**, 7–14 (2007).
9. Hancock, J. F. Lipid rafts: contentious only from simplistic standpoints. *Nature Reviews Molecular Cell Biology* **7**, 456–462 (2006).
10. van Zanten, T. S. *et al.* Hotspots of GPI-anchored proteins and integrin nanoclusters function as nucleation sites for cell adhesion. *Proceedings of the National Academy of Sciences* **106**, 18557–18562 (2009).
11. Lingwood, D. *et al.* Cholesterol modulates glycolipid conformation and receptor activity. *Nature Chemical Biology* **7**, 260 (2011).
12. Varshney, P., Yadav, V. & Saini, N. Lipid rafts in immune signalling: current progress and future perspective. *Immunology* **149**, 13–24 (2016).
13. Mayor, S. & Rao, M. Rafts: Scale-Dependent, Active Lipid Organization at the Cell Surface: Raft Hypothesis. *Traffic* **5**, 231–240 (2004).
14. Goswami, D. *et al.* Nanoclusters of GPI-Anchored Proteins Are Formed by Cortical Actin-Driven Activity. *Cell* **135**, 1085–1097 (2008).

15. Fujiwara, T., Ritchie, K., Murakoshi, H., Jacobson, K. & Kusumi, A. Phospholipids undergo hop diffusion in compartmentalized cell membrane. *The Journal of Cell Biology* **157**, 1071–1082 (2002).

16. Lajoie, P., Goetz, J. G., Dennis, J. W. & Nabi, I. R. Lattices, rafts, and scaffolds: domain regulation of receptor signaling at the plasma membrane. *The Journal of Cell Biology* **185**, 381–385 (2009).

17. Subramaniam, A. B., Guidotti, G., Manoharan, V. N. & Stone, H. A. Glycans pattern the phase behaviour of lipid membranes. *Nature Materials* **12**, 128–133 (2012).

18. Groves, J. T. Cell membranes: Glycans' imprints. *Nature Materials* **12**, 96–97 (2013).

19. Garcia-Parajo, M. F., Cambi, A., Torreno-Pina, J. A., Thompson, N. & Jacobson, K. Nanoclustering as a dominant feature of plasma membrane organization. *Journal of Cell Science* **127**, 4995–5005 (2014).

20. Blouin, C. M. *et al.* Glycosylation-Dependent IFN-γR Partitioning in Lipid and Actin Nanodomains Is Critical for JAK Activation. *Cell* **166**, 920–934.

21. Dietrich, C. *et al.* Lipid rafts reconstituted in model membranes. *Biophysical Journal* **80**, 1417–1428 (2001).

22. Veatch, S. L. & Keller, S. L. Organization in Lipid Membranes Containing Cholesterol. *Physical Review Letters* **89**, 268101 (2002).

23. Kahya, N., Scherfeld, D., Bacia, K., Poolman, B. & Schwille, P. Probing Lipid Mobility of Raft-exhibiting Model Membranes by Fluorescence Correlation Spectroscopy. *Journal of Biological Chemistry* **278**, 28109–28115 (2003).

24. Chiantia, S., Ries, J., Kahya, N. & Schwille, P. Combined AFM and Two-Focus SFCS Study of Raft-Exhibiting Model Membranes. *ChemPhysChem* **7**, 2409–2418 (2006).

25. Simons, K. & Vaz, W. L. C. Model Systems, Lipid Rafts, and Cell Membranes. *Annual Review of Biophysics and Biomolecular Structure* **33**, 269–295 (2004).

26. Tamm, L. K. & McConnell, H. M. Supported phospholipid bilayers. *Biophysical Journal* **47**, 105–113 (1985).

27. Sezgin, E. *et al.* Elucidating membrane structure and protein behavior using giant plasma membrane vesicles. *Nature Protocols* **7**, 1042–1051 (2012).

28. Baumgart, T. *et al.* Large-scale fluid/fluid phase separation of proteins and lipids in giant plasma membrane vesicles. *Proceedings of the National Academy of Sciences* **104**, 3165–3170 (2007).

29. Lingwood, D., Ries, J., Schwille, P. & Simons, K. Plasma membranes are poised for activation of raft phase coalescence at physiological temperature. *Proceedings of the National Academy of Sciences* **105**, 10005–10010 (2008).

30. Hammond, A. T. *et al.* Crosslinking a lipid raft component triggers liquid ordered-liquid disordered phase separation in model plasma membranes.

Proceedings of the National Academy of Sciences of the United States of America **102**, 6320–6325 (2005).

31. Munro, S. Lipid rafts: elusive or illusive? *Cell* **115**, 377–388 (2003).
32. Klotzsch, E. & Schütz, G. J. A critical survey of methods to detect plasma membrane rafts. *Philosophical Transactions of the Royal Society B: Biological Sciences* **368**, 20120033 (2013).
33. Kenworthy, A. K. Fluorescence Recovery After Photobleaching Studies of Lipid Rafts. in *Lipid Rafts* (ed. McIntosh, T. J.) 179–192 (Humana Press, 2007). doi:10.1007/978-1-59745-513-8_13.
34. Chen, Y., Lagerholm, B. C., Yang, B. & Jacobson, K. Methods to measure the lateral diffusion of membrane lipids and proteins. *Methods* **39**, 147–153 (2006).
35. Dietrich, C., Yang, B., Fujiwara, T., Kusumi, A. & Jacobson, K. Relationship of Lipid Rafts to Transient Confinement Zones Detected by Single Particle Tracking. *Biophysical Journal* **82**, 274–284.
36. Marguet, D., Lenne, P., Rigneault, H. & He, H. Dynamics in the plasma membrane: how to combine fluidity and order. *The EMBO Journal* **25**, 3446 (2006).
37. Bacia, K., Kim, S. A. & Schwille, P. Fluorescence cross-correlation spectroscopy in living cells. *Nature Methods* **3**, 83–89 (2006).
38. He, H.-T. & Marguet, D. Detecting Nanodomains in Living Cell Membrane by Fluorescence Correlation Spectroscopy. *Annual Review of Physical Chemistry* **62**, 417–436 (2011).
39. Yechiel, E. & Edidin, M. Micrometer-scale domains in fibroblast plasma membranes. *The Journal of Cell Biology* **105**, 755 (1987).
40. Lenne, P.-F. *et al.* Dynamic molecular confinement in the plasma membrane by microdomains and the cytoskeleton meshwork. *The EMBO Journal* **25**, 3245–3256 (2006).
41. Wawrezinieck, L., Rigneault, H., Marguet, D. & Lenne, P.-F. Fluorescence Correlation Spectroscopy Diffusion Laws to Probe the Submicron Cell Membrane Organization. *Biophysical Journal* **89**, 4029–4042 (2005).
42. Ruprecht, V., Wieser, S., Marguet, D. & Schütz, G. J. Spot Variation Fluorescence Correlation Spectroscopy Allows for Superresolution Chronoscopy of Confinement Times in Membranes. *Biophysical Journal* **100**, 2839–2845 (2011).
43. Winkler, P. M. *et al.* Optical Antenna-Based Fluorescence Correlation Spectroscopy to Probe the Nanoscale Dynamics of Biological Membranes. *The Journal of Physical Chemistry Letters* **9**, 110–119 (2018).
44. Lasserre, R. *et al.* Raft nanodomains contribute to Akt/PKB plasma membrane recruitment and activation. *Nature Chemical Biology* **4**, 538 (2008).

45. Simons, K. & Gerl, M. J. Revitalizing membrane rafts: new tools and insights. *Nature Reviews Molecular Cell Biology* **11**, 688–699 (2010).

46. Betzig, E. *et al.* Imaging Intracellular Fluorescent Proteins at Nanometer Resolution. *Science* **313**, 1642 (2006).

47. Hess, S. T., Girirajan, T. P. K. & Mason, M. D. Ultra-High Resolution Imaging by Fluorescence Photoactivation Localization Microscopy. *Biophysical Journal* **91**, 4258–4272 (2006).

48. Rust, M. J., Bates, M. & Zhuang, X. Sub-diffraction-limit imaging by stochastic optical reconstruction microscopy (STORM). *Nature Methods* **3**, 793–796 (2006).

49. Hell, S. W. & Wichmann, J. Breaking the diffraction resolution limit by stimulated emission: stimulated-emission-depletion fluorescence microscopy. *Optics Letters* **19**, 780–782 (1994).

50. Klar, T. A., Jakobs, S., Dyba, M., Egner, A. & Hell, S. W. Fluorescence microscopy with diffraction resolution barrier broken by stimulated emission. *Proceedings of the National Academy of Sciences* **97**, 8206–8210 (2000).

51. Hell, S. W. Far-Field Optical Nanoscopy. *Science* **316**, 1153–1158 (2007).

52. Hwang, J., Gheber, L. A., Margolis, L. & Edidin, M. Domains in cell plasma membranes investigated by near-field scanning optical microscopy. *Biophysical Journal* **74**, 2184–2190 (1998).

53. De Lange, F. *et al.* Cell biology beyond the diffraction limit: near-field scanning optical microscopy. *Journal of Cell Science* **114**, 4153–4160 (2001).

54. van Zanten, T. S. *et al.* Direct mapping of nanoscale compositional connectivity on intact cell membranes. *Proceedings of the National Academy of Sciences* **107**, 15437–15442 (2010).

55. van Zanten, T. S., Cambi, A. & Garcia-Parajo, M. F. A nanometer scale optical view on the compartmentalization of cell membranes. *Biochimica et Biophysica Acta (BBA) - Biomembranes* **1798**, 777–787 (2010).

56. Dufrêne, Y. F. & Garcia-Parajo, M. F. Recent progress in cell surface nanoscopy: Light and force in the near-field. *Nano Today* **7**, 390–403 (2012).

57. Manzo, C., van Zanten, T. S. & Garcia-Parajo, M. F. Nanoscale Fluorescence Correlation Spectroscopy on Intact Living Cell Membranes with NSOM Probes. *Biophysical Journal* **100**, L8–L10 (2011).

58. Mivelle, M., van Zanten, T. S. & Garcia-Parajo, M. F. Hybrid Photonic Antennas for Subnanometer Multicolor Localization and Nanoimaging of Single Molecules. *Nano Letters* **14**, 4895–4900 (2014).

59. Gwosch, K. C. *et al.* MINFLUX nanoscopy delivers 3D multicolor nanometer resolution in cells. *Nature Methods* **17**, 217–224 (2020).

60. Mueller, V. *et al.* STED Nanoscopy Reveals Molecular Details of Cholesterol- and Cytoskeleton-Modulated Lipid Interactions in Living Cells. *Biophysical Journal* **101**, 1651–1660 (2011).

61. Honigmann, A. *et al.* A lipid bound actin meshwork organizes liquid phase separation in model membranes. *Elife* **3**, e01671 (2014).

62. Vicidomini, G. *et al.* STED-FLCS: An Advanced Tool to Reveal Spatiotemporal Heterogeneity of Molecular Membrane Dynamics. *Nano Letters* **15**, 5912–5918 (2015).

63. Honigmann, A. *et al.* Scanning STED-FCS reveals spatiotemporal heterogeneity of lipid interaction in the plasma membrane of living cells. *Nature Communications* **5**, 5412 (2014).

64. Eggeling, C. *et al.* Direct observation of the nanoscale dynamics of membrane lipids in a living cell. *Nature* **457**, 1159–1162 (2009).

65. Honigmann, A., Mueller, V., Hell, S. W. & Eggeling, C. STED microscopy detects and quantifies liquid phase separation in lipid membranes using a new far-red emitting fluorescent phosphoglycerolipid analogue. *Faraday Discussions* **161**, 77–89 (2013).

66. Sezgin, E. *et al.* Measuring nanoscale diffusion dynamics in cellular membranes with super-resolution STED–FCS. *Nature Protocols* **14**, 1054–1083 (2019).

67. Schneider, F. *et al.* High photon count rates improve the quality of super-resolution fluorescence fluctuation spectroscopy. *Journal of Physics D: Applied Physics* **53**, 164003 (2020).

68. Clausen, M. P. *et al.* A straightforward approach for gated STED-FCS to investigate lipid membrane dynamics. *Methods* **88**, 67–75 (2015).

69. Sarangi, N. K., Ayappa, K. G. & Basu, J. K. Complex dynamics at the nanoscale in simple biomembranes. *Scientific Reports* **7**, 11173 (2017).

70. Pinkwart, K. *et al.* Nanoscale dynamics of cholesterol in the cell membrane. *Journal of Biological Chemistry* **294**, 12599–12609 (2019).

71. Manzo, C. & Garcia-Parajo, M. F. A review of progress in single particle tracking: from methods to biophysical insights. *Reports on Progress in Physics* **78**, 124601 (2015).

72. Ortega-Arroyo, J. & Kukura, P. Interferometric scattering microscopy (iSCAT): new frontiers in ultrafast and ultrasensitive optical microscopy. *Physical Chemistry Chemical Physics* **14**, 15625 (2012).

73. Spillane, K. M. *et al.* High-Speed Single-Particle Tracking of GM1 in Model Membranes Reveals Anomalous Diffusion due to Interleaflet Coupling and Molecular Pinning. *Nano Letters* **14**, 5390–5397 (2014).

74. Spindler, S. *et al.* Visualization of lipids and proteins at high spatial and temporal resolution via interferometric scattering (iSCAT) microscopy. *Journal of Physics D: Applied Physics* **49**, 274002 (2016).

75. Taylor, R. W. *et al.* Interferometric scattering microscopy reveals microsecond nanoscopic protein motion on a live cell membrane. *Nature Photonics* **13**, 480–487 (2019).

76. Wu, H.-M., Lin, Y.-H., Yen, T.-C. & Hsieh, C.-L. Nanoscopic substructures of raft-mimetic liquid-ordered membrane domains revealed by high-speed single-particle tracking. *Scientific Reports* **6**, 20542 (2016).

77. Reina, F. *et al.* Complementary studies of lipid membrane dynamics using iSCAT and super-resolved fluorescence correlation spectroscopy. *Journal of Physics D: Applied Physics* **51**, 235401 (2018).

78. Taylor, R. W. & Sandoghdar, V. Interferometric Scattering Microscopy: Seeing Single Nanoparticles and Molecules via Rayleigh Scattering. *Nano Letters* **19**, 4827–4835 (2019).

79. Holzmeister, P., Acuna, G. P., Grohmann, D. & Tinnefeld, P. Breaking the concentration limit of optical single-molecule detection. *Chemical Society Reviews* **43**, 1014–1028 (2014).

80. Punj, D. *et al.* Plasmonic antennas and zero-mode waveguides to enhance single molecule fluorescence detection and fluorescence correlation spectroscopy toward physiological concentrations: Plasmonic antennas and zero mode waveguides. *Wiley Interdisciplinary Reviews: Nanomedicine and Nanobiotechnology* **6**, 268–282 (2014).

81. Wenger, J. & Rigneault, H. Photonic Methods to Enhance Fluorescence Correlation Spectroscopy and Single Molecule Fluorescence Detection. *International Journal of Molecular Sciences* **11**, 206–221 (2010).

82. Levene, M. J. *et al.* Zero-Mode Waveguides for Single-Molecule Analysis at High Concentrations. *Science* **299**, 682 (2003).

83. Moran-Mirabal, J. M. & Craighead, H. G. Zero-mode waveguides: Sub-wavelength nanostructures for single molecule studies at high concentrations. *Methods* **46**, 11–17 (2008).

84. Genet, C. & Ebbesen, T. W. Light in tiny holes. *Nature* **445**, 39–46 (2007).

85. Samiee, K. T., Moran-Mirabal, J. M., Cheung, Y. K. & Craighead, H. G. Zero Mode Waveguides for Single-Molecule Spectroscopy on Lipid Membranes. *Biophysical Journal* **90**, 3288–3299 (2006).

86. Wenger, J., Rigneault, H., Dintinger, J., Marguet, D. & Lenne, P.-F. Single-Fluorophore Diffusion in a Lipid Membrane over a Subwavelength Aperture. *Journal of Biological Physics* **32**, SN1–SN4 (2006).

87. Edel, J. B., Wu, M., Baird, B. & Craighead, H. G. High Spatial Resolution Observation of Single-Molecule Dynamics in Living Cell Membranes. *Biophysical Journal* **88**, L43–L45 (2005).

88. Moran-Mirabal, J. M., Torres, A. J., Samiee, K. T., Baird, B. A. & Craighead, H. G. Cell investigation of nanostructures: zero-mode waveguides for plasma membrane studies with single molecule resolution. *Nanotechnology* **18**, 195101 (2007).

89. Richards, C. I. *et al.* Live-Cell Imaging of Single Receptor Composition Using Zero-Mode Waveguide Nanostructures. *Nano Letters* **12**, 3690–3694 (2012).

90. Wenger, J. *et al.* Diffusion Analysis within Single Nanometric Apertures Reveals the Ultrafine Cell Membrane Organization. *Biophysical Journal* **92**, 913–919 (2007).

91. Gérard, D. *et al.* Nanoaperture-enhanced fluorescence: Towards higher detection rates with plasmonic metals. *Phys. Rev. B* **77**, 045413 (2008).

92. Kelly, C. V., Baird, B. A. & Craighead, H. G. An Array of Planar Apertures for Near-Field Fluorescence Correlation Spectroscopy. *Biophysical Journal* **100**, L34–L36 (2011).

93. Kelly, C. V., Wakefield, D. L., Holowka, D. A., Craighead, H. G. & Baird, B. A. Near-Field Fluorescence Cross-Correlation Spectroscopy on Planar Membranes. *ACS Nano* **8**, 7392–7404 (2014).

94. Schuller, J. A. *et al.* Plasmonics for extreme light concentration and manipulation. *Nature Materials* **9**, 193–204 (2010).

95. Novotny, L. & van Hulst, N. Antennas for light. *Nature Photonics* **5**, 83–90 (2011).

96. Biagioni, P., Huang, J.-S. & Hecht, B. Nanoantennas for visible and infrared radiation. *Reports on Progress in Physics* **75**, 024402 (2012).

97. Halas, N. J., Lal, S., Chang, W.-S., Link, S. & Nordlander, P. Plasmons in Strongly Coupled Metallic Nanostructures. *Chemical Reviews* **111**, 3913–3961 (2011).

98. Koenderink, A. F. Single-Photon Nanoantennas. *ACS Photonics* **4**, 710–722 (2017).

99. Kinkhabwala, A. *et al.* Large single-molecule fluorescence enhancements produced by a bowtie nanoantenna. *Nature Photonics* **3**, 654–657 (2009).

100. Acuna, G. P. *et al.* Fluorescence Enhancement at Docking Sites of DNA-Directed Self-Assembled Nanoantennas. *Science* **338**, 506–510 (2012).

101. Puchkova, A. *et al.* DNA Origami Nanoantennas with over 5000-fold Fluorescence Enhancement and Single-Molecule Detection at 25 μM. *Nano Letters* **15**, 8354–8359 (2015).

102. Yuan, H., Khatua, S., Zijlstra, P., Yorulmaz, M. & Orrit, M. Thousand-fold Enhancement of Single-Molecule Fluorescence Near a Single Gold Nanorod. *Angewandte Chemie International Edition* **52**, 1217–1221 (2013).

103. Khatua, S. *et al.* Resonant Plasmonic Enhancement of Single-Molecule Fluorescence by Individual Gold Nanorods. *ACS Nano* **8**, 4440–4449 (2014).

104. Flauraud, V. *et al.* Large-Scale Arrays of Bowtie Nanoaperture Antennas for Nanoscale Dynamics in Living Cell Membranes. *Nano Letters* **15**, 4176–4182 (2015).

105. Flynn, J. D., Haas, B. L. & Biteen, J. S. Plasmon-Enhanced Fluorescence from Single Proteins in Living Bacteria. *The Journal of Physical Chemistry C* **120**, 20512–20517 (2016).

106. Fabrizio, E. D. *et al.* Roadmap on biosensing and photonics with advanced nano-optical methods. *Journal of Optics* **18**, 063003 (2016).

107. Perozziello, G. *et al.* Microfluidic device for continuous single cells analysis via Raman spectroscopy enhanced by integrated plasmonic nanodimers. *Optics Express* **24**, A180–A190 (2016).

108. Coluccio, M. L. *et al.* Detection of single amino acid mutation in human breast cancer by disordered plasmonic self-similar chain. *Science Advances* **1**, e1500487 (2015).

109. Langguth, L. & Femius Koenderink, A. Simple model for plasmon enhanced fluorescence correlation spectroscopy. *Optics Express* **22**, 15397–15409 (2014).

110. Estrada, L. C., Aramendía, P. F. & Martínez, O. E. 10000 times volume reduction for fluorescence correlation spectroscopy using nano-antennas. *Optics Express* **16**, 20597–20602 (2008).

111. Wang, Q. *et al.* Fluorescence correlation spectroscopy near individual gold nanoparticle. *Chemical Physics Letters* **503**, 256–261 (2011).

112. Lu, G. *et al.* Plasmonic near-field in the vicinity of a single gold nanoparticle investigated with fluorescence correlation spectroscopy. *Nanoscale* **4**, 3359–3364 (2012).

113. Punj, D., de Torres, J., Rigneault, H. & Wenger, J. Gold nanoparticles for enhanced single molecule fluorescence analysis at micromolar concentration. *Opt. Express* **21**, 27338–27343 (2013).

114. Khatua, S., Yuan, H. & Orrit, M. Enhanced-fluorescence correlation spectroscopy at micro-molar dye concentration around a single gold nanorod. *Physical Chemistry Chemical Physics* **17**, 21127–21132 (2015).

115. Kinkhabwala, A. A., Yu, Z., Fan, S. & Moerner, W. E. Fluorescence correlation spectroscopy at high concentrations using gold bowtie nanoantennas. *Chemical Physics* **406**, 3–8 (2012).

116. Dutta Choudhury, S., Ray, K. & Lakowicz, J. R. Silver Nanostructures for Fluorescence Correlation Spectroscopy: Reduced Volumes and Increased Signal Intensities. *The Journal of Physical Chemistry Letters* **3**, 2915–2919 (2012).

117. Punj, D. *et al.* Self-Assembled Nanoparticle Dimer Antennas for Plasmonic-Enhanced Single-Molecule Fluorescence Detection at Micromolar Concentrations. *ACS Photonics* **2**, 1099–1107 (2015).

118. Punj, D. *et al.* A plasmonic 'antenna-in-box' platform for enhanced single-molecule analysis at micromolar concentrations. *Nature Nanotechnology* **8**, 512–516 (2013).

119. Flauraud, V. *et al.* In-Plane Plasmonic Antenna Arrays with Surface Nanogaps for Giant Fluorescence Enhancement. *Nano Letters* **17**, 1703–1710 (2017).

120. Pradhan, B. *et al.* Gold-Nanorod-Enhanced Fluorescence Correlation Spectroscopy of Fluorophores with High Quantum Yield in Lipid Bilayers. *The Journal of Physical Chemistry C* **120**, 25996–26003 (2016).

121. Ghenuche, P., de Torres, J., Moparthi, S. B., Grigoriev, V. & Wenger, J. Nanophotonic Enhancement of the Förster Resonance Energy-Transfer Rate with Single Nanoapertures. *Nano Letters* **14**, 4707–4714 (2014).

122. Winkler, P. M. *et al.* Transient Nanoscopic Phase Separation in Biological Lipid Membranes Resolved by Planar Plasmonic Antennas. *ACS Nano* **11**, 7241–7250 (2017).

123. Sahoo, H. & Schwille, P. Influence of glycosaminoglycans on lipid dynamics in supported phospholipid bilayers. *Soft Matter* **9**, 3859 (2013).

124. Regmi, R. *et al.* Planar Optical Nanoantennas Resolve Cholesterol-Dependent Nanoscale Heterogeneities in the Plasma Membrane of Living Cells. *Nano Letters* **17**, 6295–6302 (2017).

125. Giannini, V., Fernández-Domínguez, A. I., Heck, S. C. & Maier, S. A. Plasmonic Nanoantennas: Fundamentals and Their Use in Controlling the Radiative Properties of Nanoemitters. *Chemical Reviews* **111**, 3888–3912 (2011).

126. Anger, P., Bharadwaj, P. & Novotny, L. Enhancement and Quenching of Single-Molecule Fluorescence. *Physical Review Letters* **96**, 113002 (2006).

127. Kühn, S., Håkanson, U., Rogobete, L. & Sandoghdar, V. Enhancement of Single-Molecule Fluorescence Using a Gold Nanoparticle as an Optical Nanoantenna. *Physical Review Letters* **97**, 017402 (2006).

128. Chikkaraddy, R. *et al.* Single-molecule strong coupling at room temperature in plasmonic nanocavities. *Nature* **535**, 127–130 (2016).

129. Benz, F. *et al.* Single-molecule optomechanics in "picocavities". *Science* **354**, 726–729 (2016).

130. Bidault, S. *et al.* Picosecond Lifetimes with High Quantum Yields from Single-Photon-Emitting Colloidal Nanostructures at Room Temperature. *ACS Nano* **10**, 4806–4815 (2016).

131. Akselrod, G. M. *et al.* Probing the mechanisms of large Purcell enhancement in plasmonic nanoantennas. *Nature Photonics* **8**, 835–840 (2014).

132. Hoang, T. B., Akselrod, G. M. & Mikkelsen, M. H. Ultrafast Room-Temperature Single Photon Emission from Quantum Dots Coupled to Plasmonic Nanocavities. *Nano Letters* **16**, 270–275 (2016).

133. Wientjes, E., Renger, J., Cogdell, R. & van Hulst, N. F. Pushing the Photon Limit: Nanoantennas Increase Maximal Photon Stream and Total Photon Number. *The Journal of Physical Chemistry Letters* **7**, 1604–1609 (2016).

134. Pellegrotti, J. V. *et al.* Controlled Reduction of Photobleaching in DNA Origami–Gold Nanoparticle Hybrids. *Nano Letters* **14**, 2831–2836 (2014).

135. Duan, H., Hu, H., Kumar, K., Shen, Z. & Yang, J. K. W. Direct and Reliable Patterning of Plasmonic Nanostructures with Sub-10-nm Gaps. *ACS Nano* **5**, 7593–7600 (2011).

136. Kollmann, H. *et al.* Toward Plasmonics with Nanometer Precision: Nonlinear Optics of Helium-Ion Milled Gold Nanoantennas. *Nano Letters* **14**, 4778–4784 (2014).

137. Duan, H., Hu, H., Hui, H. K., Shen, Z. & Yang, J. K. W. Free-standing sub-10 nm nanostencils for the definition of gaps in plasmonic antennas. *Nanotechnology* **24**, 185301 (2013).

138. Wang, Y. M. *et al.* High aspect ratio 10-nm-scale nanoaperture arrays with template-guided metal dewetting. *Scientific Reports* **5**, 9654 (2015).

139. Thacker, V. V. *et al.* DNA origami based assembly of gold nanoparticle dimers for surface-enhanced Raman scattering. *Nature Communications* **5**, 3448 (2014).

140. Kühler, P. *et al.* Plasmonic DNA-Origami Nanoantennas for Surface-Enhanced Raman Spectroscopy. *Nano Letters* **14**, 2914–2919 (2014).

141. Flauraud, V. *et al.* Nanoscale topographical control of capillary assembly of nanoparticles. *Nature Nanotechnology* (2016) doi:10.1038/nnano.2016.179.

142. *Single molecule detection in solution: methods and applications*. (Wiley-VCH, 2002).

143. Maiti, S., Haupts, U. & Webb, W. W. Fluorescence correlation spectroscopy: diagnostics for sparse molecules. *Proceedings of the National Academy of Sciences* **94**, 11753–11757 (1997).

144. Novotny, L. & Hecht, B. *Principles of nano-optics*. (Cambridge University Press, 2012).

145. Giannini, V., Sánchez-Gil, J. A., Muskens, O. L. & Rivas, J. G. Electrodynamic calculations of spontaneous emission coupled to metal nanostructures of arbitrary shape: nanoantenna-enhanced fluorescence. *Journal of the Optical Society of America B* **26**, 1569 (2009).

146. Giannini, V. *et al.* Controlling Light Localization and Light-Matter Interactions with Nanoplasmonics. *Small* **6**, 2498–2507 (2010).

147. *Cavity quantum electrodynamics*. (Academic Press, Inc., Boston, MA (United States), 1994).

148. Bharadwaj, P. & Novotny, L. Spectral dependence of single molecule fluorescence enhancement. *Optics Express* **15**, 14266 (2007).

149. Elson, D. *et al.* Time-domain fluorescence lifetime imaging applied to biological tissue. *Photochemical & Photobiological Sciences* **3**, 795 (2004).

150. Grecco, H. E. & Verveer, P. J. FRET in Cell Biology: Still Shining in the Age of Super-Resolution? *ChemPhysChem* **12**, 484–490 (2011).

151. *Advanced photon counting: applications, methods, instrumentation*. (Springer, 2015).

152. Nagpal, P., Lindquist, N. C., Oh, S.-H. & Norris, D. J. Ultrasmooth Patterned Metals for Plasmonics and Metamaterials. *Science* **325**, 594–597 (2009).

153. Zhou, W. & Odom, T. W. Tunable subradiant lattice plasmons by out-of-plane dipolar interactions. *Nature Nanotechnology* **6**, 423–427 (2011).

154. Aouani, H. *et al.* Crucial Role of the Adhesion Layer on the Plasmonic Fluorescence Enhancement. *ACS Nano* **3**, 2043–2048 (2009).

155. Kapusta, P. Absolute Diffusion Coefficients: Compilation of Reference Data for FCS Calibration. http://www.picoquant.com/images/uploads/page/files/7353/appnote_diffusioncoefficients.pdf (2017).

156. Aouani, H. *et al.* Bright Unidirectional Fluorescence Emission of Molecules in a Nanoaperture with Plasmonic Corrugations. *Nano Letters* **11**, 637–644 (2011).

157. Brown, D. A. & London, E. Structure and Function of Sphingolipid- and Cholesterol-rich Membrane Rafts. *Journal of Biological Chemistry* **275**, 17221–17224 (2000).

158. Owen, D. M., Williamson, D. J., Magenau, A. & Gaus, K. Sub-resolution lipid domains exist in the plasma membrane and regulate protein diffusion and distribution. *Nature Communications* **3**, 1256 (2012).

159. Simons, K. & Toomre, D. Lipid rafts and signal transduction. *Nature Reviews Molecular Cell Biology* **1**, 31–39 (2000).

160. Yasuda, T., Tsuchikawa, H., Murata, M. & Matsumori, N. Deuterium NMR of Raft Model Membranes Reveals Domain-Specific Order Profiles and Compositional Distribution. *Biophysical Journal* **108**, 2502–2506 (2015).

161. Nicolau, D. V., Burrage, K., Parton, R. G. & Hancock, J. F. Identifying Optimal Lipid Raft Characteristics Required To Promote Nanoscale Protein-Protein Interactions on the Plasma Membrane. *Molecular and Cellular Biology* **26**, 313–323 (2006).

162. Mühlschlegel, P., Eisler, H.-J., Martin, O. J. F., Hecht, B. & Pohl, D. W. Resonant optical antennas. *Science* **308**, 1607–1609 (2005).

163. Schuck, P. J., Fromm, D. P., Sundaramurthy, A., Kino, G. S. & Moerner, W. E. Improving the Mismatch between Light and Nanoscale Objects with Gold Bowtie Nanoantennas. *Physical Review Letters* **94**, (2005).

164. Worley, C. G. & Linton, R. W. Removing sulfur from gold using ultraviolet/ozone cleaning. *Journal of Vacuum Science & Technology A: Vacuum, Surfaces, and Films* **13**, 2281–2284 (1995).

165. Chiantia, S., Kahya, N. & Schwille, P. Dehydration Damage of Domain-Exhibiting Supported Bilayers: An AFM Study on the Protective Effects of Disaccharides and Other Stabilizing Substances. *Langmuir* **21**, 6317–6323 (2005).

166. Sezgin, E. *et al.* Partitioning, diffusion, and ligand binding of raft lipid analogs in model and cellular plasma membranes. *Biochimica et Biophysica Acta (BBA) - Biomembranes* **1818**, 1777–1784 (2012).

167. McPeak, K. M. *et al.* Plasmonic Films Can Easily Be Better: Rules and Recipes. *ACS Photonics* **2**, 326–333 (2015).

168. Baffou, G., Quidant, R. & García de Abajo, F. J. Nanoscale Control of Optical Heating in Complex Plasmonic Systems. *ACS Nano* **4**, 709–716 (2010).

169. Apajalahti, T. *et al.* Concerted diffusion of lipids in raft-like membranes. *Faraday Discussions* **144**, 411–430 (2010).

170. Silvius, J. R. Role of cholesterol in lipid raft formation: lessons from lipid model systems. *Biochimica et Biophysica Acta (BBA) - Biomembranes* **1610**, (2003).

171. de Almeida, R. F. M., Loura, L. M. S., Fedorov, A. & Prieto, M. Lipid Rafts have Different Sizes Depending on Membrane Composition: A Time-resolved Fluorescence Resonance Energy Transfer Study. *Journal of Molecular Biology* **346**, 1109–1120 (2005).

172. Ma, Y., Hinde, E. & Gaus, K. Nanodomains in biological membranes. *Essays in Biochemistry* **57**, 93–107 (2015).

173. Köster, D. V. & Mayor, S. Cortical actin and the plasma membrane: inextricably intertwined. *Current Opinion in Cell Biology* **38**, 81–89 (2016).

174. Buffone, A. & Weaver, V. M. Don't sugarcoat it: How glycocalyx composition influences cancer progression. *The Journal of Cell Biology* **219**, e201910070 (2020).

175. Lanctot, P. M., Gage, F. H. & Varki, A. P. The glycans of stem cells. *Current Opinion in Chemical Biology* **11**, 373–380 (2007).

176. Haltiwanger, R. S. & Lowe, J. B. Role of Glycosylation in Development. *Annual Review of Biochemistry* **73**, 491–537 (2004).

177. Paszek, M. J. *et al.* The cancer glycocalyx mechanically primes integrin-mediated growth and survival. *Nature* **511**, 319–325 (2014).

178. Torreno-Pina, J. A. *et al.* Enhanced receptor-clathrin interactions induced by N-glycan-mediated membrane micropatterning. *Proceedings of the National Academy of Sciences* **111**, 11037–11042 (2014).

179. Freeman, S. A. *et al.* Transmembrane Pickets Connect Cyto- and Pericellular Skeletons Forming Barriers to Receptor Engagement. *Cell* **172**, 305–317 (2018).

180. Sil, P. *et al.* Dynamic actin-mediated nano-scale clustering of CD44 regulates its meso-scale organization at the plasma membrane. *Molecular Biology of the Cell* **31**, 511–723 (2020).

181. Mingeot-Leclercq, M.-P., Deleu, M., Brasseur, R. & Dufrêne, Y. F. Atomic force microscopy of supported lipid bilayers. *Nature Protocols* **3**, 1654–1659 (2008).

182. Proksch, R., Schäffer, T. E., Cleveland, J. P., Callahan, R. C. & Viani, M. B. Finite optical spot size and position corrections in thermal spring constant calibration. *Nanotechnology* **15**, 1344–1350 (2004).

183. Fraser, J. R. E., Laurent, T. C. & Laurent, U. B. G. Hyaluronan: its nature, distribution, functions and turnover. *Journal of Internal Medicine* **242**, 27–33 (1997).

184. Aufderhorst-Roberts, A., Chandra, U. & Connell, S. D. Three-Phase Coexistence in Lipid Membranes. *Biophysical Journal* **112**, 313–324 (2017).

185. Garcia-Manyes, S. & Sanz, F. Nanomechanics of lipid bilayers by force spectroscopy with AFM: A perspective. *Biochimica et Biophysica Acta (BBA) - Biomembranes* **1798**, 741–749 (2010).

186. Gumí-Audenis, B. *et al.* Structure and Nanomechanics of Model Membranes by Atomic Force Microscopy and Spectroscopy: Insights into the Role of Cholesterol and Sphingolipids. *Membranes* **6**, 58 (2016).

187. Crespo-Villanueva, A. *et al.* Casein interaction with lipid membranes: Are the phase state or charge density of the phospholipids affecting protein adsorption? *Biochimica et Biophysica Acta (BBA) - Biomembranes* **1860**, 2588–2598 (2018).

188. Connell, S. D. & Smith, D. A. The atomic force microscope as a tool for studying phase separation in lipid membranes (Review). *Molecular Membrane Biology* **23**, 17–28 (2006).

189. Guyomarc'h, F., Chen, M., Et-Thakafy, O., Zou, S. & Lopez, C. Gel-gel phase separation within milk sphingomyelin domains revealed at the nanoscale using atomic force microscopy. *Biochimica et Biophysica Acta (BBA) - Biomembranes* **1859**, 949–958 (2017).

190. Gumí-Audenis, B. *et al.* In-plane molecular organization of hydrated single lipid bilayers: DPPC:cholesterol. *Nanoscale* **10**, 87–92 (2018).

191. Gumí-Audenis, B., Sanz, F. & Giannotti, M. I. Impact of galactosylceramides on the nanomechanical properties of lipid bilayer models: an AFM-force spectroscopy study. *Soft Matter* **11**, 5447–5454 (2015).

192. Nyholm, T. K. M., Lindroos, D., Westerlund, B. & Slotte, J. P. Construction of a DOPC/PSM/Cholesterol Phase Diagram Based on the Fluorescence Properties of *trans* -Parinaric Acid. *Langmuir* **27**, 8339–8350 (2011).

193. Veatch, S. L. & Keller, S. L. Miscibility Phase Diagrams of Giant Vesicles Containing Sphingomyelin. *Physical Review Letters* **94**, 148101 (2005).

194. Koukalová, A. *et al.* Lipid Driven Nanodomains in Giant Lipid Vesicles are Fluid and Disordered. *Scientific Reports* **7**, 5460 (2017).

195. Eaton, P. J. & West, P. *Atomic force microscopy*. (Oxford University Press, 2010).

196. Ramstedt, B. & Slotte, J. P. Sphingolipids and the formation of sterol-enriched ordered membrane domains. *Biochimica et Biophysica Acta (BBA) - Biomembranes* **1758**, 1945–1956 (2006).

197. Giannotti, M. I., Rinaudo, M. & Vancso, G. J. Force Spectroscopy of Hyaluronan by Atomic Force Microscopy: From Hydrogen-Bonded Networks toward Single-Chain Behavior. *Biomacromolecules* **8**, 2648–2652 (2007).

198. Mombelli, E., Morris, R., Taylor, W. & Fraternali, F. Hydrogen-Bonding Propensities of Sphingomyelin in Solution and in a Bilayer Assembly: A Molecular Dynamics Study. *Biophysical Journal* **84**, 1507–1517 (2003).

199. Meder, D., Moreno, M. J., Verkade, P., Vaz, W. L. C. & Simons, K. Phase coexistence and connectivity in the apical membrane of polarized epithelial cells. *Proceedings of the National Academy of Sciences of the United States of America* **103**, 329–334 (2006).

200. Kastrup, L., Blom, H., Eggeling, C. & Hell, S. W. Fluorescence Fluctuation Spectroscopy in Subdiffraction Focal Volumes. *Physical Review Letters* **94**, 178104 (2005).

201. Lohmüller, T. *et al.* Single Molecule Tracking on Supported Membranes with Arrays of Optical Nanoantennas. *Nano Letters* **12**, 1717–1721 (2012).

202. Mivelle, M., van Zanten, T. S., Neumann, L., van Hulst, N. F. & Garcia-Parajo, M. F. Ultrabright Bowtie Nanoaperture Antenna Probes Studied by Single Molecule Fluorescence. *Nano Letters* **12**, 5972–5978 (2012).

203. Garcia-Parajo, M. F. Optical antennas focus in on biology. *Nature Photonics* **2**, 201–203 (2008).

204. Zhang, K. & Yang, H. Photon-by-Photon Determination of Emission Bursts from Diffusing Single Chromophores. *The Journal of Physical Chemistry B* **109**, 21930–21937 (2005).

205. Kalappurakkal, J. M., Sil, P. & Mayor, S. Toward a new picture of the living plasma membrane. *Protein Science* **29**, 1355–1365 (2020).

206. Krieger, J. W. *et al.* Imaging fluorescence (cross-) correlation spectroscopy in live cells and organisms. *Nature Protocols* **10**, 1948–1974 (2015).

207. Buchholz, J. *et al.* Widefield High Frame Rate Single-Photon SPAD Imagers for SPIM-FCS. *Biophysical Journal* **114**, 2455–2464 (2018).

208. Needleman, D. J., Xu, Y. & Mitchison, T. J. Pin-Hole Array Correlation Imaging: Highly Parallel Fluorescence Correlation Spectroscopy. *Biophysical Journal* **96**, 5050–5059 (2009).

209. Oh, D., Zidovska, A., Xu, Y. & Needleman, D. J. Development of Time-Integrated Multipoint Moment Analysis for Spatially Resolved Fluctuation Spectroscopy with High Time Resolution. *Biophysical Journal* **101**, 1546–1554 (2011).

210. Lippincott-Schwartz, J., Snapp, E. & Kenworthy, A. Studying protein dynamics in living cells. *Nature Reviews Molecular Cell Biology* **2**, 444–456 (2001).

211. Shroff, H., Galbraith, C. G., Galbraith, J. A. & Betzig, E. Live-cell photoactivated localization microscopy of nanoscale adhesion dynamics. *Nature Methods* **5**, 417–423 (2008).

212. Saemisch, L., Liebel, M. & van Hulst, N. F. Isolating strong nanoantenna–molecule interactions by ensemble-level single-molecule detection. *Nanoscale* **12**, 3723–3730 (2020).

213. Sriram, V., Krishnan, K. S. & Mayor, S. deep-orange and carnation define distinct stages in late endosomal biogenesis in Drosophila melanogaster. *Journal of Cell Biology* **161**, 593–607 (2003).

214. Huang, F. *et al.* Video-rate nanoscopy using sCMOS camera–specific single-molecule localization algorithms. *Nature Methods* **10**, 653–658 (2013).

215. Magatti, D. & Ferri, F. Fast multi-tau real-time software correlator for dynamic light scattering. *Applied Optics* **40**, 4011–4021 (2001).

216. Krieger, J. W. & Langowski, J. QuickFit 3.0. *http://www.dkfz.de/Macromol/quickfit/*.

217. Chen, Y., Müller, J. D., So, P. T. C. & Gratton, E. The Photon Counting Histogram in Fluorescence Fluctuation Spectroscopy. *Biophysical Journal* **77**, 553–567 (1999).

218. Sharma, P. *et al.* Nanoscale organization of multiple GPI-anchored proteins in living cell membranes. *Cell* **116**, 577–589 (2004).

219. Saha, S. *et al.* Diffusion of GPI-anchored proteins is influenced by the activity of dynamic cortical actin. *Molecular Biology of the Cell* **26**, 4033–4045 (2015).

220. Frantz, C., Stewart, K. M. & Weaver, V. M. The extracellular matrix at a glance. *Journal of Cell Science* **123**, 4195–4200 (2010).

221. Mouw, J. K., Ou, G. & Weaver, V. M. Extracellular matrix assembly: a multiscale deconstruction. *Nature Reviews Molecular Cell Biology* **15**, 771–785 (2014).

222. Briddon, S. J. *et al.* Quantitative analysis of the formation and diffusion of A1-adenosine receptor-antagonist complexes in single living cells. *Proceedings of the National Academy of Sciences* **101**, 4673–4678 (2004).

223. Knight, M. W. *et al.* Aluminum Plasmonic Nanoantennas. *Nano Letters* **12**, 6000–6004 (2012).

224. Krasnok, A. E., Miroshnichenko, A. E., Belov, P. A. & Kivshar, Y. S. All-dielectric optical nanoantennas. *Optics Express* **20**, 20599 (2012).

225. Kuznetsov, A. I., Miroshnichenko, A. E., Brongersma, M. L., Kivshar, Y. S. & Lukyanchuk, B. Optically resonant dielectric nanostructures. *Science* **354**, 2472 (2016).

226. Regmi, R. *et al.* All-Dielectric Silicon Nanogap Antennas To Enhance the Fluorescence of Single Molecules. *Nano Letters* **16**, 5143–5151 (2016).

227. Krmpot, A. J. *et al.* Functional Fluorescence Microscopy Imaging: Quantitative Scanning-Free Confocal Fluorescence Microscopy for the Characterization of Fast Dynamic Processes in Live Cells. *Analytical Chemistry* **91**, 11129–11137 (2019).

228. Guo, R., Hakala, T. K. & Törmä, P. Geometry dependence of surface lattice resonances in plasmonic nanoparticle arrays. *Physical Review B* **95**, 155423 (2017).

229. Humphrey, A. D. & Barnes, W. L. Plasmonic surface lattice resonances on arrays of different lattice symmetry. *Physical Review B* **90**, 075404 (2014).

230. Rechberger, W. *et al.* Optical properties of two interacting gold nanoparticles. *Optics Communications* **220**, 137–141 (2003).

231. Tretnak, V., Hohenester, U., Krenn, J. R. & Hohenau, A. The Role of Particle Size in the Dispersion Engineering of Plasmonic Arrays. *The Journal of Physical Chemistry C* **124**, 2104–2112 (2020).

232. Sankaran, J. & Wohland, T. Fluorescence strategies for mapping cell membrane dynamics and structures. *APL Bioengineering* **4**, 020901 (2020).

233. Hell, S. & Stelzer, E. H. K. Properties of a 4Pi confocal fluorescence microscope. *Journal of the Optical Society of America A* **9**, 2159 (1992).